

**Deterministically fabricated, quantum dot based
single-photon sources for quantum information
technologies**

vorgelegt von
Master of Science
Sarah Fischbach

Von der Fakultät II - Mathematik und Naturwissenschaften
der Technischen Universität Berlin
zur Erlangung des akademischen Grades
Doktor der Naturwissenschaften
Dr. rer. nat.
genehmigte Dissertation

Promotionsausschuss:

Vorsitzender: Prof. Dr. Andreas Knorr

Gutachter: Prof. Dr. Stephan Reitzenstein

Gutachter: Prof. Dr. Armando Rastelli

Tag der wissenschaftlichen Aussprache: 22.02.2019

Berlin 2019

Zusammenfassung

Das große Potential der Quanteninformationstechnologie kann bereits durch erste experimentelle Realisierungen demonstriert werden, welche zumeist die Polarisations-eigenschaften einzelner Photonen für die Verarbeitung und Übertragung von Quantenzuständen verwenden. Die Datensicherheit solcher Systeme basiert entscheidend auf der Verfügbarkeit von triggerbaren Einzelphotonenquellen. Als exzellente Quantenlichtquellen haben sich Halbleiter-Quantenpunkte erwiesen, die im Rahmen der vorliegenden Arbeit unter Verwendung einer deterministischen Prozessierungstechnologie in Mikrolinsen integriert werden. Um auf Basis dieses Konzepts effiziente und marktfähige Quellen herstellen zu können, müssen noch weitere Entwicklungsschritte für den praktischen Einsatz erreicht werden. Diese Arbeit zeigt Möglichkeiten zur Erhöhung der Photonen-Auskopplungseffizienz Quantenpunkt-basierter Mikrostrukturen, eine Methode zur Feinjustierung der Emissions-Wellenlänge durch Verspannungseintrag, sowie einen Ansatz zur Faserkopplung der Emission.

Unter Verwendung der sogenannten in-situ Elektronenstrahlolithographie werden die Quantenpunkte anhand ihrer Kathodolumineszenz ausgewählt und mit hoher Positioniergenauigkeit und Prozessausbeute in Mikrostrukturen integriert. Im Vergleich zu Emittern im einfachen planaren Halbleiter kann durch eine Kombination aus rückseitigem Spiegel und einer Mesa oder Linse mit angepasster Geometrie eine deutliche Erhöhung der Auskopplungseffizienz erreicht werden. Mithilfe von Simulationen basierend auf der Finite-Elemente-Methode können optimale Designparameter für diese Strukturen gefunden werden. Abhängig von der numerischen Apertur (NA) der Sammeloptik lassen sich theoretisch Auskopplungseffizienzen von bis zu $\eta_{\text{Sim}} = 80\%$ bei einer NA von 1,0 ermöglichen. Durch Entwicklung und Anwendung eines Goldbonding-Schritts mittels Thermokompression werden Quantenpunkt-Mikrostrukturen mit einem rückseitigen Goldspiegel versehen, sodass Quantenlichtquellen mit einer gemessenen Effizienz von bis zu $\eta_{\text{Exp}} = (20 \pm 2)\%$ bei einer NA von 0,4 realisiert werden. Die gleiche Bond-Technik kann verwendet werden, um eine Quantenpunktprobe mit einem piezoelektrischen Aktuator zu verbinden, sodass ein direkter Verspannungsübertrag auf den Emitter erfolgen kann. Hierdurch wird die Emissionswellenlänge einer Quantenpunkt-Mikrolinse kontrolliert über eine extern angelegte Spannung um $\Delta\lambda = 1,7\text{ nm}$ verstimmt.

Um die Effizienz, mit der die Quantenpunkt-Emission eingesammelt wird, weiter zu erhöhen, werden Mikroobjektive mithilfe des Zwei-Photonen Laserstrahlschreibens mit Quantenpunkt-Mikrolinsen kombiniert. Hierdurch kann eine Auskopplungseffizienz von $\eta_{\text{Exp}} = (40 \pm 4) \%$ bei gleichzeitiger Erhöhung der Anregungseffizienz um etwa eine Größenordnung erreicht werden. Darüber hinaus wird ein Ansatz zur direkten Kopplung der Emission einer Quantenpunkt-Mikrolinse in eine Single-Mode Glasfaser präsentiert. In Kombination mit einer elektrischen Kontaktierung der Struktur kann dies in zukünftigen Experimenten die Verwendung der Quantenpunkt-Mikrolinsen als Quelle einer „stand-alone“ Einzelphotonenlichtquelle ermöglichen, die zum Betrieb lediglich eine externe Stromzufuhr benötigt.

Die vorliegende Arbeit gibt eine detaillierte Einführung in die benötigten Methoden für die Herstellung von Quantenpunkt-basierten Mikrostrukturen, zeigt eine theoretische Evaluierung des verwendeten Design-Konzepts und präsentiert Verbesserungen und Erweiterungen auf dem Weg zu einer marktfähigen Einzelphotonenquelle. Im Rahmen der Arbeit kann so gezeigt werden, dass deterministisch hergestellte Quantenpunkt-Mikrolinsen sehr gut als spektral durchstimmbare und effiziente Quellen für einzelne Photonen oder verschränkte Photonenpaare für Anwendungen in der Quanteninformationstechnologie geeignet sind.

Abstract

First experimental demonstrations proved the potential of quantum information technologies, which in many cases choose the polarization characteristics of single photons to process and transport quantum states. The security of such systems crucially relies on the availability of on-demand single-photon sources. Semiconductor quantum dots demonstrate to be excellent sources of quantum light, which in the scope of this work are integrated into microlenses, using a deterministic processing technique. To create efficient plug-and-play sources based on this concept, several further steps need to be taken. This work presents means to increase the photon-extraction efficiency of quantum dot based microstructures, a method to achieve a tunability of the emission wavelength by strain transfer and introduces a fiber-coupling approach.

The quantum dots are chosen by their cathodoluminescence signal and precisely integrated into microstructures with a high yield, using a method called in-situ electron-beam lithography. By a combination of a backside mirror with a mesa or lens with an adjusted geometry, an increased photon-extraction efficiency can be achieved as compared to bulk structures. Optimum design parameters are found by the use of finite-element simulations. Depending on the numerical aperture of the collection optics, theoretically extraction efficiencies of up to $\eta_{\text{Sim}} = 80\%$ can be achieved into a numerical aperture of 1.0. By development and application of a thermocompression gold-bonding step, quantum dot microstructures are combined with a backside gold mirror to create sources with measured efficiencies of up to $\eta_{\text{Exp}} = (20 \pm 2)\%$. The same bonding technique can be used to mount a quantum dot sample onto a piezoelectric actuator, which allows for a strain transfer to the emitter. In that way, the emission wavelength of a quantum dot microlens can be altered by $\Delta\lambda = 1.7\text{ nm}$ using an externally applied voltage.

To further enhance the collected amount of the quantum dot luminescence, microobjectives written by two-photon direct laser writing can be combined with quantum dot microlenses. In that way, a photon-extraction efficiency of $\eta_{\text{Exp}} = (40 \pm 4)\%$ is achieved while increasing the excitation efficiency by around one order of magnitude. Finally, a direct coupling of the emission into a single-mode fiber is presented by the use of a combination of microobjectives and a fiber mount created by direct laser writing. In future experiments such fiber-coupled samples could be combined with electrical contacts to create a stand-alone

single-photon source which solely relies on an external power supply.

This thesis gives a thorough introduction to the required methods for the fabrication of quantum dot based microstructures, presents a theoretical evaluation of the design concepts and demonstrates improvements and new features, which show that quantum dot microlenses serve as tunable and efficient sources of single-photons or entangled photon pairs for quantum information applications.

Contents

1	Introduction	1
1.1	Quantum information applications of single-photon technology	1
1.2	Basic approaches to the realization of single-photon sources	4
1.3	Thesis structure	6
2	Quantum dots as emitters of non-classical light	9
2.1	Statistics of light	9
2.2	Quantum dots as emitters of non-classical light	11
2.2.1	Optical characteristics	12
2.2.2	Line broadening	15
2.2.3	Effects of strain on semiconductor quantum dots	16
2.3	Single-photon sources for quantum communication	20
3	Processing technology for single-photon sources	25
3.1	Epitaxial growth of self-assembled semiconductor quantum dots	25
3.2	Nanofabrication with cathodoluminescence lithography	27
3.2.1	Setup for in-situ 3-D electron-beam lithography	29
3.2.2	Resist characteristics	30
3.2.3	Cathodoluminescence measurements and deterministic lithography .	32
3.2.4	Processing of deterministically written microstructures	33
3.3	Bonding techniques for semiconductor samples	35
3.3.1	Bonding with adhesives	36
3.3.2	Direct bonding by surface attraction forces	38
3.3.3	Thermocompression gold bonding	38
3.3.4	Thermosonic bonding	39
3.3.5	Flip-chip thermocompression gold bonding of GaAs quantum dot samples	41
3.4	Two-photon direct laser writing	42
4	Photoluminescence measurements	45
4.1	Micro-photoluminescence spectroscopy	45

4.2	Determining the photon-extraction efficiency	47
4.3	Time-resolved measurements	48
4.4	Photon-autocorrelation measurements	49
4.5	Setup for fiber-coupled single-photon sources	50
5	Tailoring the outcoupling characteristics of single-photon emitters	51
5.1	Simulation concept using a finite-element method	51
5.2	Backside mirrors and cavities	52
5.3	Micromesas and microlenses	56
5.4	Parameter variations	59
5.5	Discussion	61
6	Experimental implementation of a backside gold mirror for quantum dot microstructures	63
6.1	Sample fabrication	63
6.2	Micro-photoluminescence measurement results	65
6.3	Comparison and discussion	69
7	Wavelength tuning of single-photon sources	71
7.1	Tuning methods for quantum dot based nanostructures	71
7.1.1	Temperature tuning	72
7.1.2	Electrical tuning	72
7.1.3	Strain tuning	72
7.2	Strain tuning of quantum dot microlenses by the use of piezoelectric actuators	73
7.2.1	Properties of piezoelectric materials	73
7.2.2	Characteristics of the piezoelectric actuators	74
7.2.3	Sample fabrication	75
7.2.4	Micro-photoluminescence measurements	75
7.2.5	Comparison to simulation results	80
7.3	Outlook and discussion	82
8	Using 3-D printed optical elements for high photon-extraction efficiencies and fiber-coupling	83
8.1	Increasing the photon-extraction efficiency of single-photon sources with 3-D written microobjectives	84
8.1.1	Design and fabrication	84
8.1.2	Micro-photoluminescence measurements	85

8.2	Coupling to single-mode fibers with 3-D written objectives and mounting support	89
8.2.1	Design and fabrication	89
8.2.2	Evaluation of the fiber-coupling of a quantum dot microlens	91
8.3	Discussion	94
9	Summary and outlook	95
	Bibliography	99
A	Comparison of different design approaches for single-photon sources based on quantum dots	127
B	Layer designs for sample growth by MOCVD	129
	Danksagung	130
	Versicherung an Eides statt	133

1 Introduction

Research on quantum technologies has produced exciting results in the past years, leading to first commercially available implementations in this emerging field of science and technology. Quantum communication, for instance, has been used for the transfer of election results in the Canton of Geneva in Switzerland since 2007 [Stu11]. First systems for quantum computation proved to optimize problems of traffic distribution much faster than conventional computers [Neu17]. These achievements are based on extensive research on theoretical concepts of quantum information methods as well as on the rapid development of quantum devices created by nanotechnology.

This work presents advances in the field of single-photon emitters, which in many approaches serve as the source of the quantum bits that are transported by quantum communication or used by a quantum computer. To build reliable systems of quantum information technology, bright plug-and-play single-photon sources are required. To employ the excellent quantum optical properties of self-assembled quantum dots (QD), a deterministic processing method is required, as the structures are randomly distributed in their location and emission wavelength. Crucial improvements of deterministic QD based sources will be presented in the following chapters, such as an increase of the photon-extraction efficiency, as well as a tunability method and an approach for a fiber-coupling of the emission. The motivation for these achievements is explained in the next section, where a more detailed introduction to quantum information applications is given. Afterwards, important approaches to the creation of single-photon sources are discussed to give a context for the results presented in this thesis.

1.1 Quantum information applications of single-photon technology

Based on the fundamental concepts of Bennett and Brassard in 1984 (BB-84) [Ben84] and Ekert in 1991 (Ekert-91) [Eke91], quantum key distribution (QKD) has become an important alternative to conventional cryptography methods. It does not rely on computational complexity, but on the characteristics of quantum mechanical bits (qubits), which are used to transfer a secret key between a sender and a receiver. Any third-party attempt to intercept and copy a qubit is inhibited due to the fact that the exact state of a quantum

system cannot be replicated (no-cloning theorem [Woo82]).

Single photons are the most promising candidates for such flying qubits, as their polarization characteristics serve as easily accessible quantum states. Moreover, they show low decoherence and experimental realizations can rely on existing optical technology and infrastructure. While the BB-84-protocol encodes data bits on the polarization states of single photons, other versions, such as the Ekert-91-protocol, use entangled photon pairs to transfer the data. After the first demonstrations of QKD systems [Asp82, Ben92, Res05, Rau14], transmission distances have been quickly increased to more than 100 km [Tak05, Yin16]. In a further step, QKD experiments have recently been taken to space with a satellite that allows to repeatably send a quantum signal over a distance of 1200 km to a ground-station on earth [Lia18].

First commercial systems offering QKD solutions, e.g. by *ID Quantique*, use attenuated laser sources to create the single-photon emission. With these implementations, the data transfer is limited by a trade-off between efficiency and security. The emission from a laser follows a poissonian distribution inducing a finite probability for multi-photon emission events even at low average photon number. A data transfer with more than just one photon per bit opens the security loophole of photon-number splitting attacks [Bra00]. A pure single-photon emission corresponds to a Fock state with one particle, which is a quantum mechanical description of a state having an average of one and zero variance in the photon number. Such states can only be generated by sources that inherently guarantee a single-photon emission, e.g. from an atomic transition or the recombination of charge carriers. The structures presented in this thesis belong to that category of true quantum light sources. QDs are used as the emitters which show atom-like energy states due to the spatial confinement of charge carriers [Ree88], such that single photons are created by the recombination of bound electron-hole pairs (excitons) [Mic00a, Bec01].

As decoherence and absorption of photons can never be fully eliminated, QKD on distances beyond 100 km will require space based solutions or quantum repeater concepts that transport quantum states in a cascaded system between different network nodes [Dua01]. The transmission distance is divided into several segments and entangled qubits are generated and purified on each segment [Bri98]. Then entanglement swapping is implemented at the connecting points between neighboring segments followed by another purification. To use entanglement swapping, it is a prerequisite to have indistinguishable pairs of entangled photons. QDs can generate pairs of entangled photons via the emission from the biexciton-exciton radiative cascade [Ben00], but when using QDs created by self-assembled growth, a tunability method is required to create a network of sources emitting at matching wavelength on the scale of the homogeneous linewidth.

The idea of a large scale quantum network based on entangled photons is motivated by the implementation of a world-wide quantum internet [Kim00]. In such a system, not only secure data transfer, but also methods of distributed quantum computing can be implemented with single photons. In the past years, different approaches towards quantum computation came up, which can tackle different kinds of calculations that are computationally expensive or even practically unsolvable on classical computers (quantum supremacy). Fermionic problems can be solved by machines based on quantum gates, which can be created by superconducting qubits [Cla08]. Boson sampling [Aar13], in contrast, could successfully be implemented using indistinguishable single photons [Spr13]. It samples the distribution of bosonic states that have undergone a unitary transformation, which is computationally expensive on a classical computer. Furthermore, the protocol by Knill, Laflamme and Milburn shows that all basic logical gates required for more universal computation methods can be created using linear optical elements [Kni01, Kok07]. Their approach again relies on the availability of entangled pairs of indistinguishable photons. The ability to store a quantum state is important for applications in quantum communication as well as computation. Here, first demonstrations make use of the coupling between photons and atoms [Spe11], atomic ensembles [Cho08] or solid state memories [Tir15]. These examples show that single-photon technology establishes exciting concepts and applications in the field of quantum information science. They rely, however, on the availability of sources of single photons and entangled photon pairs, which have to fulfill challenging requirements. The most important ones are:

- An on-demand generation of single photons or entangled photon-pairs.
- A vanishing probability for the emission of multi-photon states ($g^{(2)}(\tau = 0) = 0$).
- A photon-extraction efficiency (PE) close to $\eta = 100$ %, which means that every excitation pulse should create a photon that is collected for transfer and use as a qubit.
- Sources with low decoherence, spectral diffusion and time jitter, to emit single photons with high indistinguishability.
- A precise control of the emission wavelength of the photons on the scale of their own homogeneous linewidth, required for the creation of indistinguishable photons from different sources or the coupling to optical resonances of quantum memories.
- Finally, for a distributed commercial usage the sources should be scalable, fiber-coupled and they should be operated as a stand-alone device requiring only a power supply.

There is no single-photon technology so far which could fulfill all of those requirements simultaneously. In this thesis, deterministically fabricated sources based on InGaAs QDs are presented. New technological steps are introduced which serve to increase the PE, ensure a control of the emission wavelength and allow for a fiber-coupling of the emission. To show how our sources compare to other approaches, different kinds of single-photon emitters will be discussed in the following.

1.2 Basic approaches to the realization of single-photon sources

Since the definition of non-classical light in contrast to thermal or laser light has been understood, many different approaches have been used to find the best kind of source to create it. Early demonstrations could be made with single atoms [Kim77], but to increase their efficiency and stability they need to be cooled down to below one millikelvin in complex experimental setups [Kuh02]. The approach requires expensive stabilization and cooling systems, which make it impracticable for scalable or commercial applications. Single-photon emitters working at room-temperature could be realized with color centers in diamond, such as the nitrogen-vacancy [Kur00] or the silicon-vacancy defects [Loh15]. Their electron spin states have a long coherence time and can be read out by the characteristics of the optical transitions, which has allowed for demonstrations of entanglement across more than one kilometer at cryogenic temperatures [Hen15]. In comparison to other approaches, however, the visibility of the emitted photons is limited by homogeneous and inhomogeneous broadening [Sip14, Joh17].

Further demonstrations of single-photon emission have recently been made using defect states in 2-dimensional (2-D) materials, such as transition metal dichalcogenides [He15, Kop15]. The basic characteristics of this technology, however, are still being investigated, and their geometry limits the available methods for the creation of advanced photonic structures.

A technique frequently used for demonstrations of quantum information applications is spontaneous parametric downconversion, as it serves to create single-photons in room-temperature operation in compact experimental settings. It uses the generation of two entangled photons from one laser pulse inside a nonlinear crystal [Shi88, Kwi95] or nonlinear waveguides [Tan02, Lai16, Mon17]. The second photon can serve to monitor at which times a single-photon is emitted, as this only happens with a limited probability. Moreover, a spectral filtering is usually necessary as the photon emission has a bandwidth of several nanometers, such that the overall efficiency of the approach is limited.

The single-photon sources presented in this thesis are based on self-assembled InGaAs QDs

in a GaAs matrix material. These emitters proved to give a single-photon emission with suitable characteristics, demonstrated by values of the photon autocorrelation $g^{(2)}(0) < 0.01$, and almost perfect indistinguishability with $V > 95\%$ [Wei14, Din16, Tho16, Som16]. These results were achieved by cooling the samples to cryogenic temperatures to limit linewidth broadening due to phonon interaction and thermal emission of the emitters into the wetting layer or barriers. First approaches of room-temperature operation with nitride-based QDs have already been demonstrated, but so far they cannot be used to reproduce the aforementioned qualities [Hol14]. QDs allow for the generation of entangled photon pairs with high fidelity [Tro15b, Bou18, Hub18b] and can be integrated into advanced nanophotonic structures using the full range of semiconductor processing methods. The latter are used to solve the challenge of extracting the emitted photons from the host material.

Prominent approaches to increase the PE of QDs in semiconductor material are micropillar structures with high-Q cavities [Hei10, Din16], nanowires [Fri09, Cla10], photonic crystal cavities [Lee15] and microlenses [Gsc15b]. An overview of the different designs and their characteristics is given in Appendix A. In this work, we focus on QD microlens structures, as they serve to achieve an increased efficiency on a broadband wavelength range of more than 10 nanometers. This is crucial for the generation of entangled photon pairs, as the excitonic and biexcitonic transitions usually emit at separated photon energies. The enhancement of the emission is achieved by a combination of a backside mirror, in previous works a distributed bragg reflector (DBR), and a microstructure on top of the QD. In this thesis, different design approaches are evaluated using finite-element simulations. A substitution of the DBR mirror by a backside gold mirror is tested theoretically and experimentally, as the latter already showed promising results, e.g. in combination with QDs integrated into nanowires [Cla10].

Previous experiments demonstrated that QD microlenses give $g^{(2)}(0)$ -values below 0.01 [Gsc15b] and photon indistinguishabilities above 95% [Tho16]. Moreover, a deterministic processing method called in-situ electron-beam lithography (EBL) has been developed that allows us to create QD microstructures at desired emission characteristics with a high yield [Gsc13]. In this way, a pre-selection of the emission wavelength of the QD with an accuracy of 0.3 nm is possible. However, for advanced methods of quantum information technology, a wavelength matching to other sources or a quantum memory with a higher accuracy on the scale of the homogeneous emitter linewidth is required. Consequently, the development of a tuning mechanism is a central task approached in this work. In addition, a combination of our samples with on-chip components written by direct laser writing is tested. Microscale optical structures written with this method served to increase

the field of view of optical fibers and image sensors [Gis16b, Thi17] and could similarly collect the emission from QD microlenses from a large angle. A method to collimate or focus the QD emission by an on-chip device can also be highly beneficial for fiber-coupling approaches. Recently, a technique for a multimode fiber-coupling of QD-microlenses has been demonstrated [Sch18a], and a first approach towards a single-mode fiber coupling of the QD emission will be presented here.

1.3 Thesis structure

The different aspects of extending the concept of deterministic QD microstructures are covered in the following order:

Chapter 2 gives an introduction to QDs and their unique properties that make them a promising source of quantum light. After explaining the basic few-particle complexes found in semiconductor QDs, the impact of internal and external strain on the optical characteristics is discussed. Finally, a brief introduction to concepts of quantum communication is given, to provide further background on the requirements stated for single-photon sources.

In **Chapter 3**, methods of nanofabrication are described, that are used in the context of this thesis. Two central aspects are the in-situ EBL required for the creation of QD microlenses and the introduction of bonding processes for semiconductor samples that can be applied to integrate the structures onto a piezoelectric actuator. Additionally, the basic aspects of 3-dimensional (3-D) direct laser writing are presented, which allows one to integrate microoptical structures onto semiconductor samples.

Chapter 4 completes the methodological part with an introduction to the most important measurement techniques used for the characterization of single-photon sources. The samples created in this work are designed for optical excitation, such that micro-photoluminescence measurements in free-beam or fiber-coupled setups are implemented. Experiments in pulsed excitation allow for the generation of time-resolved results, which give important information on the efficiency, emitter lifetime and photon autocorrelation of the sources.

In **Chapter 5**, finite-element simulation results are presented that motivate and determine the design of the samples introduced in the following chapters. A theoretical comparison between samples with a backside DBR and a gold mirror is given. In both cases, optimum

design parameters for mesa structures as well as microlenses are found, which maximize the PE. The latter can be evaluated for different numerical apertures of the collection optics and under the impact of small parameter variations.

The first experimental results, described in **Chapter 6**, show single-photon sources with a backside gold mirror, demonstrating the successful combination of a thermocompression gold bonding step with in-situ EBL for the integration of QDs into microstructures. It is shown that high PEs and low values of the second-order autocorrelation function are obtained for these structures.

In **Chapter 7**, the same fabrication methods are used to create a single-photon source which is tunable in its emission wavelength by strain transfer from a piezoelectric actuator. Micro-photoluminescence measurements allow for an investigation of the impact of the strain tuning on different characteristics of the single-photon sources. A comparison with theoretical results from a continuum elasticity model gives a deeper understanding of the observed mechanism.

Chapter 8 deals with the combination of QD microlenses with microobjectives created by 3-D direct laser writing to increase the extraction efficiency in small numerical apertures. In a second step, components written by direct laser writing can be used for coupling of the single-photon emission to a single-mode fiber.

Finally, **Chapter 9** discusses the presented results in the context of state-of-the-art technology and research and proposes further steps to bring QD-based devices towards efficient, plug-and-play single-photon sources with tunable emission characteristics.

2 Quantum dots as emitters of non-classical light

In this chapter semiconductor QDs are introduced as sources of single-photons. At first, a definition of a single-photon emission in contrast to forms of classical light is given. Subsequently, it is explained how semiconductor QDs can serve as single-photon emitters due to their quantized energy level distribution caused by the 3-D confinement of charge carriers in the structures. The properties of few-particle states in QDs are discussed in detail, as they determine the wavelength, polarization and coherence of QD-based single-photon sources. A closer look is taken at the effects of strain on these energy states. Finally, an introduction to the most important methods of quantum communication is given to motivate the most important requirements for single-photon sources.

2.1 Statistics of light

Single-photon emitters are distinguished from classical emitters, such as lasers or thermal light sources, by the statistics of the photon occurrences in time. These statistics can be characterized by the second-order coherence $g^{(2)}(t, t')$ between two points in time, t and t' . This description refers back to the classification of coherence by J. R. Glauber [Gla63] using higher order correlation functions expressed in the terms of the second quantization for many-body quantum systems.

Assuming that the statistical characteristics are stationary in t , the second-order coherence function can be simplified to $g^{(2)}(\tau = t' - t)$ which gives the joint probability to detect one photon at time t and a second one at time $t + \tau$. Using the creation operator \hat{a}^\dagger and annihilation operator \hat{a} it can be expressed as

$$g^{(2)}(\tau) = \frac{\langle \hat{a}^\dagger(t) \hat{a}^\dagger(t + \tau) \hat{a}(t + \tau) \hat{a}(t) \rangle}{\langle \hat{a}^\dagger(t) \hat{a}(t) \rangle^2}, \quad (2.1)$$

which we will also refer to as the second-order autocorrelation function. The symbol $\langle \rangle$ denotes the quantum mechanical expectation value in time. Photon statistics are characterized by the value of this function in the limit $\tau \rightarrow 0$. It can be simplified for stationary

systems with classical terms to

$$g^{(2)}(0) = 1 + \frac{V(\bar{n}) - \bar{n}}{\bar{n}^2}, \quad (2.2)$$

where \bar{n} is the mean and $V(\bar{n})$ the variance of the probability distribution $P(n)$ of the photon number n measured at a fixed point in time. Figure 2.1 shows a typical second-order autocorrelation function for thermal (a) and coherent light (b), as well as for a single-photon emitter (c).

A value $g^{(2)}(0) > 1$ is characteristic for thermal light, such as gained from a heated filament. This property is called bunching and describes a high probability of more than one photon to arrive in a short time interval. Thermal light follows a probability distribution

$$P_{th}(n) = \frac{\bar{n}^n}{(1 + \bar{n})^{1+n}} \quad (2.3)$$

where the variance $V(\bar{n}) = \bar{n}^2 - \bar{n}$ increases with the mean photon number.

Coherent light, which is emitted by an ideal laser, follows a Poissonian probability distribution

$$P_{coh}(n) = \frac{\bar{n}^n}{n!} e^{-\bar{n}} \quad (2.4)$$

which implies that the mean photon number is equal to the variance $\bar{n} = V(\bar{n})$. Inserting this to Equation 2.2 results in $g^{(2)}(0) = 1$, which also holds for arbitrary values of τ with $g^{(2)}(\tau) = 1$.

Non-classical light emission can be described by Fock states $|n_i\rangle$, which are defined as eigenstates $\hat{n}_i|n_i\rangle = n_i|n_i\rangle$ of the photon number operator \hat{n}_i . This implies that there is no variance of the photon number and a fixed mean $\langle n \rangle = n_i$, leading to

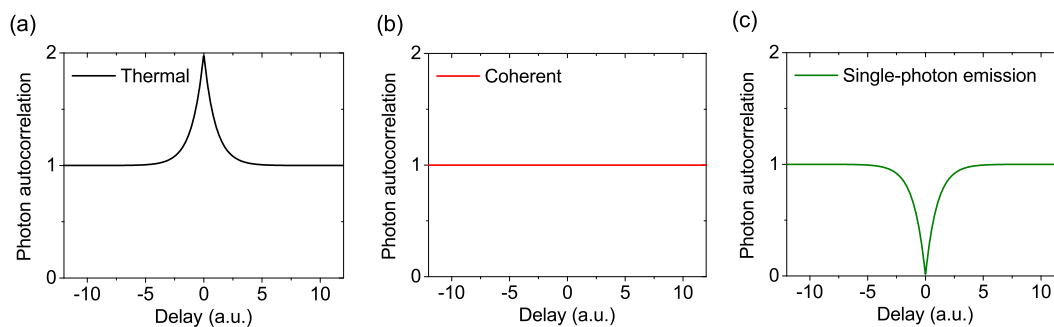


Figure 2.1: Second-order photon-autocorrelation functions $g^{(2)}(\tau)$ depending on the time delay between consecutive photons emitted by a light source. The graphs show the results for thermal (a), coherent (b) and single-photon (c) emission.

$$g^{(2)}(0) = 1 - \frac{1}{n_i}. \quad (2.5)$$

This implies that $g^{(2)}(0) < 1$, which is also referred to as antibunching and characterizes a non-classical light source. An ideal single-photon source is a special case with a photon number of $n_i = 1$. A measurement of the second-order autocorrelation should correspondingly show a value $g^{(2)}(0) = 0$.

From this comparison, it is clear that a true single-photon emission cannot be achieved by the simple attenuation of a thermal emitter or a laser. Even if the mean photon number is decreased below one, there will always be a finite probability for multi-photon emission events.

2.2 Quantum dots as emitters of non-classical light

Semiconductor QDs are nanocrystals consisting of a few thousands of atoms inside a semiconductor matrix. The QD material is chosen to have a smaller bandgap E_{gap} as compared to the surrounding one, such that charge carriers can be trapped and recombine via radiative and non-radiative channels. A highly studied material system comprises In(Ga)As QDs in a GaAs matrix ($E_{gap}^{\text{InAs}} \approx 0.36$ eV and $E_{gap}^{\text{GaAs}} \approx 1.42$ at $T = 300$ K [Sze06]), which have shown excellent performance in applications such as lasers with a high number of emitters [Led94, Hei97], high- β lasers using less than 100 QDs [Rei06] and single-photon sources based on single QDs [Mic00b, Lod15, Gsc15b, Din16].

The 3-D carrier confinement inside the QD creates 'atom-like' characteristics with discrete electronic energy levels of different orders or 'shells' as illustrated in Figure 2.2 (a). InGaAs and GaAs form a type-I energy-band alignment, which describes a confinement of charge carriers in the enclosed material section at the conduction- and the valence-band edge. To observe a quantization of the energy states, the dimensions of the QD need to be on the scale of the de-Broglie wavelength of the charge carriers [Bro25], which is defined as

$$\lambda_{dB} = \frac{h}{\sqrt{2m^*k_B T}}. \quad (2.6)$$

The effective mass of the charge carrier in the semiconductor m^* is usually much smaller than the free-electron mass, such that the size limit for a QD at cryogenic temperatures are a few tens of nanometers [Gru10].

The energy states inside the QD can be populated by electrons and holes from the surrounding material or by resonant photon absorption. Scattering processes with phonons will move charge carriers on higher order energy states to empty lower states. Due to the

strong confinement, electrons and holes form excitonic states, which are bound electron-hole pairs subject to direct and exchange Coulomb interaction.

The concept of the Bohr radius can be transferred from the hydrogen atom to describe the extension of an exciton in a bulk semiconductor. The electron mass is replaced by the reduced mass of the electron-hole pair $\mu = \frac{m_e^* \cdot m_h^*}{m_e^* + m_h^*}$, where m_e^* and m_h^* are the effective masses of electron and hole, and the resulting formula is multiplied by the material permittivity ϵ . For InAs this results in

$$a_B^X = a_B^H \cdot \frac{\epsilon}{\mu} \approx 25.6 \text{ nm} \quad (2.7)$$

with $a_B^H = 5.291 \cdot 10^{-11} \text{ m}$ and material constants for InAs taken from Reference [Gru10]. One refers to a strong confinement of an exciton inside a QD structure if the dimensions of the QD are smaller than this number, such as on the range of 10 nm [Gaa10] for InGaAs QDs.

2.2.1 Optical characteristics

Generally, electron-hole pairs in QDs can recombine via radiative as well as non-radiative decay channels, e.g. by Auger processes [Usk98] or phonon-assisted recombination at charge traps or surface states [Man15]. In direct bandgap semiconductors, such as GaAs and InAs, non-radiative decay channels are usually negligible at cryogenic temperatures, unless there is an increased number of charge traps, which can occur at a material surface in close proximity to the QD [Wan04, Sto09].

The emission energy of the radiative decay of an excitonic state depends on the confinement, defining electron and hole energy levels, Coulomb interactions, exchange interactions and additional effects due to strain and piezoelectricity. In the following, these different contributions are discussed in more detail.

In a simplified model, a quantum dot can be regarded as a potential well. Electron and hole can be described by single-particle Hamiltonians \hat{H}_e and \hat{H}_h . In this basic model, the energy levels are described by their quantum number n_x, n_y, n_z and are inversely proportional to the square of the length L of the QD

$$E_{n_x, n_y, n_z} \propto \frac{n_x^2 + n_y^2 + n_z^2}{m^* \cdot L^2}. \quad (2.8)$$

Consequently, an increase in size of the QD leads to decreased energy levels of the quantum confinement and consequently to a red-shift of the photon emission caused by a recombination process. In accordance to the description of the electron shells of an atom, the

states can be identified as s-like, p-like, et cetera. Each energy state can be occupied by two particles with opposite spin following the Pauli exclusion principle [Bay00]. Figure 2.2 (b) shows the possible configurations for the electron and hole ground states. One electron and one hole form an exciton (X). If an additional electron or hole is present, the state is defined as a charged exciton which is denoted by X^- or X^+ respectively. A full occupation with two electrons and two holes is called a biexciton (XX). This state can entail a cascaded emission of a first photon leaving an exciton state, and a second photon from the exciton recombination.

The recombination energy of an electron-hole pair depends on the difference between electron and hole states, but is additionally influenced by the Coulomb interaction between the charged particles [Sti95]. The direct Coulomb interaction, which in the case of a neutral exciton refers to the Coulomb attraction between electron and hole, is described by the Hamiltonian $\hat{H}_{Coulomb}$. If more charge carriers are present, the additional Coulomb energy can be either binding or antibinding, defining the energetic position of the transition compared to the excitonic one. The sign and magnitude of the direct Coulomb interaction depends on the localization and the overlap of the wave-functions, that are dependent on the shape and size of the quantum dot [Rod05, Sch09b].

To understand the contributions by spin interactions to the binding energy, all possible combinations of spin states of the trapped charge carriers need to be considered, as shown in the left part of the schematic in Figure 2.2 (b). The projection of the two-fold degenerate electron spin-state \mathbf{s} on the z -axis is $s_z = \pm\frac{1}{2}$ (illustrated as $|\uparrow\rangle$ and $|\downarrow\rangle$), while \mathbf{j} denotes the hole spin-state with its projection j_z . Due to the spin-orbit coupling, the lowest valence band states in cubic semiconductors are separated into a heavy-hole, a light-hole and a split-off band, which is shifted to higher energies. In a QD, hole states usually have a strong heavy-hole character with $j_z = \pm\frac{3}{2}$ (illustrated as $|\uparrow\rangle$ and $|\downarrow\rangle$), as the light-hole states are split-off by several tens of meV [Bay02] due to the influence of compressive biaxial strain. Consequently, there are four possible combinations of spin states for the exciton and its total spin vector results as the sum of electron and hole spins $\mathbf{F} = \mathbf{s} + \mathbf{j}$, with the possible projections $F_z = \pm 1, \pm 2$.

The exchange interaction, represented by the Hamiltonian \hat{H}_{ex} , is explained by the Coulomb interaction in many-body systems described by quantum mechanics. The wavefunction has to be antisymmetric towards the exchange of the fermionic particles, which leads to an additional variation in the energy states that is influenced by the symmetry of the system. In consequence, the exchange interaction splits up some of the degenerate excitonic states, depending on the symmetry in form and strain distribution of the QD [Bay99, Bay02]. This is illustrated in the right part of Figure 2.2 (b) for two different geometric conditions.

tions are called 'dark states' as they cannot couple to an electromagnetic field by emission of a single photon. Due to the dipole selection rules for the total angular momentum, only the 'bright states' with $F_z = \pm 1$ can decay radiatively. In a QD with a 2-D symmetry, the bright exciton states are degenerate, and the transition from biexciton to a bright exciton as well as from the bright exciton to the ground state emit circularly polarized photons of opposite direction. The two different decay channels $|LR\rangle$ and $|RL\rangle$ are not distinguishable by their photon wavelengths, such that an emitted photon pair is in an entangled state of right- and left-circular polarization [Ben00].

$$|\Psi^+\rangle = \frac{1}{\sqrt{2}}(|LR\rangle + |RL\rangle) \quad (2.10)$$

This configuration can be achieved for III-V QDs by growth on a (111)-oriented substrate due to the rotational symmetry of the surface [Sch09b]. It can be implemented either by a positioned growth on pre-defined patterns [Ver14, Hub17] or by a method called droplet epitaxy, which is based on a sequential deposition of group III and group V material [Man10] by molecular beam epitaxy. Droplet epitaxy has the additional advantage that the choice of the growth materials is more flexible than during Stranski-Krastanow growth, cf. Chapter 3.1, as the growth is not triggered by the strain energy of the substrate and the growth layer. This allows one to choose a material combination with a low dephasing due to a low coupling of the exciton spin with the spins of the QD nuclei [Che13], such as GaAs QDs which can be embedded inside an AlGaAs barrier [Hub17].

QDs grown on (001)-III-V-material by Stranski-Krastanow growth are usually InGaAs structures and have a lower symmetry level, such that the biexciton-exciton cascade follows an emission path with either horizontally or vertically polarized photons. In a structure with C_{2v} symmetry, the polarization directions of the exciton emission are oriented along the (110) and (1-10) crystal directions. If additional influences, such as strain or piezoelectricity, lower the QD symmetry further to C_1 , the polarization directions are shifted away from the crystal axes [Tro15a]. In both cases, the energy of the biexcitonic transitions is either increased by half of the fine-structure splitting $\frac{\Delta_{\text{FSS}}}{2}$ and the decay of the exciton is decreased by the same amount, or vice versa. Consequently, the two decay paths are distinguishable and the photon pair does not share an entangled state.

2.2.2 Line broadening

The radiative lifetime τ_1 of an excitonic state describes the time scale on which a decay is observed, resulting in the spontaneous emission of a photon. In a system without any phase-destroying mechanisms, it is antiproportional to the natural linewidth Γ of the

transition with

$$\Gamma = \frac{\hbar}{\tau_1}. \quad (2.11)$$

Assuming a typical lifetime of $\tau_1 = 1$ ns for an exciton in an InGaAs QD [Mel03], we gain a linewidth of $\Gamma \approx 0,66$ μeV .

In experiments, however, significantly higher linewidths are observed due to dephasing mechanisms by non-radiative processes. The most important effects are spectral diffusion, described with a rate Γ' , and the coupling to phonons with a rate γ . Spectral diffusion is mainly caused by charge fluctuations at surface or defect states, causing a change in the electric field that influences the QD via the quantum-confined Stark effect [Tür00]. The probability of scattering processes with phonons rises with increasing temperature, such that a significant increase in linewidth with temperature can be observed in experiments [Bor01]. Both effects contribute to the dephasing time $\tau_2 = (\Gamma' + \gamma)^{-1}$, which decreases the coherence time τ_{coh} [Byl03]

$$(\tau_{coh})^{-1} = (2\tau_1)^{-1} + (\tau_2)^{-1}. \quad (2.12)$$

To gain streams of indistinguishable photons, high coherence times are required, such that a limitation of defect states and a low sample temperature are inevitable [Tho16].

2.2.3 Effects of strain on semiconductor quantum dots

Strain can be inherently incorporated in semiconductor nanostructures due to growth or fabrication processes, such as the formation of QDs in the self-assembled growth mode. The bandstructure of a bulk semiconductor as well as the energy levels of QDs are significantly altered by deformation effects. For that reason, the application of external strain to a QD can be exploited to control the properties of its emission. For that purpose, however, it is important to understand the various effects of stress and strain onto the structures.

To describe strain effects in semiconductors, continuum mechanics can be applied. This formulation neglects the atomistic structure of the material and assumes that the physical quantities have a continuous distribution in space which can be described in tensor notation [Jog15, Sun10]. The elements of the strain tensor $\epsilon_{ij} = \frac{\delta u_i}{\delta x_j}$ represent the relative displacement of the i -th component of a unit vector \mathbf{u} along direction j . As solid materials resist deformation, a strain is always accompanied by a stress $\sigma_{ij} = \frac{F_{ij}}{A_j}$, which describes the force F_{ij} in direction i applied to a plane with area A_j and normal in direction j .

In elastic materials Hooke's law is assumed to hold for the relation between strain and

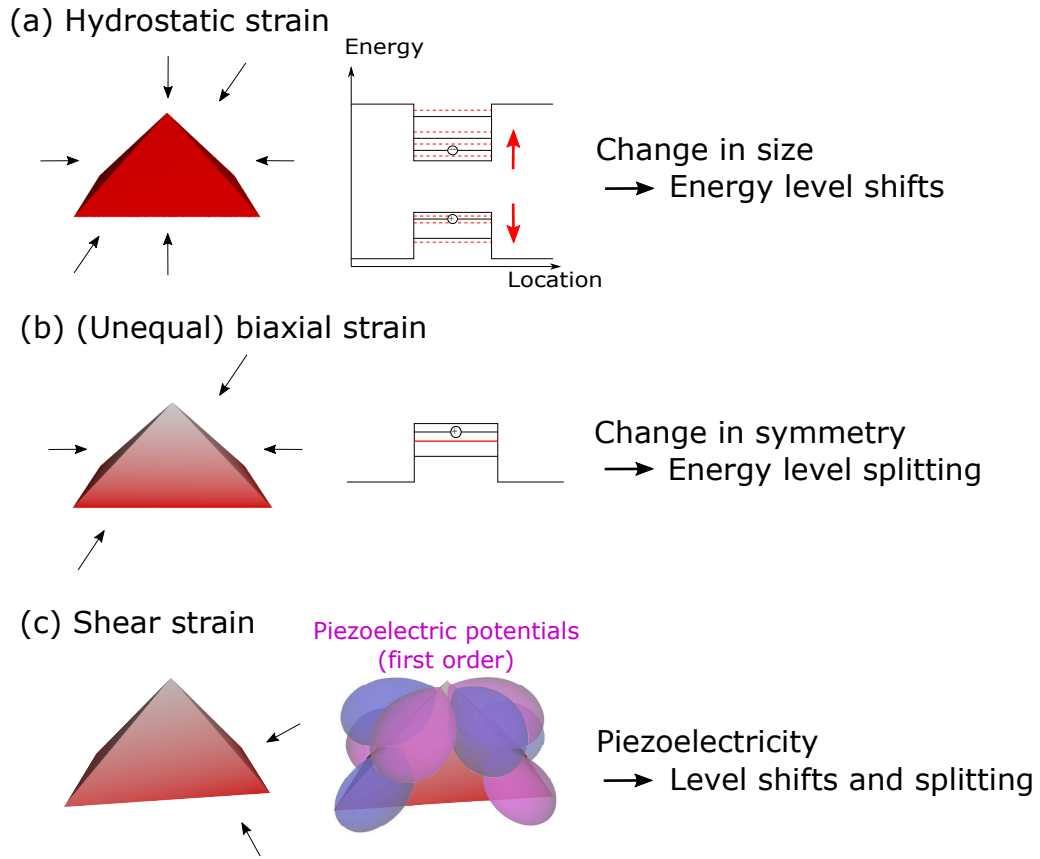


Figure 2.3: Effects of different types of strain on a pyramidal quantum dots, according to the calculations in Schliwa et al. [Sch07]: (a) Hydrostatic strain changes the size and with that the energy levels of the quantum dot. (b) Biaxial strain changes the aspect ratios of the quantum dot structure, which can split degenerate particle states. (c) Shear strain induces a piezoelectricity, which can lead to further splitting or shifts of the particle states.

stress, which is described with material-dependent elastic constants C_{ijkl} as

$$\sigma_{ij} = \sum_{kl} C_{ijkl} \epsilon_{kl}. \quad (2.13)$$

Equilibrium strain distributions in a 3-D system can be obtained by minimizing the total strain energy U_{cm} , which can be expressed as

$$U_{cm} = \frac{1}{2} \sum_{ij} C_{ijkl} \epsilon_{ij} \epsilon_{kl}. \quad (2.14)$$

The elastic constants C_{ijkl} can be simplified due to symmetry considerations from a fourth-rank tensor to a 6×6 matrix in the Voigt notation [Voi10], which is formed by only three

parameters C_{11} , C_{12} and C_{44} for cubic crystals

$$\sigma_i = \sum_j C_{ij} \epsilon_j, \quad (2.15)$$

where $\sigma_i = (\sigma_{xx}, \sigma_{yy}, \sigma_{zz}, \sigma_{yz}, \sigma_{zx}, \sigma_{xy})$ and $\epsilon_j = (\epsilon_{xx}, \epsilon_{yy}, \epsilon_{zz}, 2\epsilon_{yz}, 2\epsilon_{zx}, 2\epsilon_{xy})$. The first three components describe a strain in normal direction altering the volume of the crystal, while the other three components are shear strains. We refer to a strain as hydrostatic, if it is equal in all three main axes, $\epsilon_{xx} = \epsilon_{yy} = \epsilon_{zz}$, such that it only causes volumetric changes. All other strain components, that cause a change in the geometry of the structure, are called deviatoric strains [Sad09]. A simple example is a biaxial strain, where a compressive strain in one direction, e.g. ϵ_{zz} , is combined with a tensile strain along the x- and y-axis, or vice versa.

In a bulk semiconductor, a hydrostatic compressive strain leads to a widening of the bandgap, as the interatomic interaction is increased. Deviatoric forms of strain, such as biaxial strain or shear strain $(\epsilon_{yz}, \epsilon_{zx}, \epsilon_{xy})$, change the crystal geometry and induce piezoelectricity. Both effects can lead to a change in the bandstructure in the reciprocal space, such as a lifting of the degeneracy of valence or conduction bands or a warping of the bands [Sun10].

Piezoelectricity only occurs in crystals that lack a center of inversion, such as zinc-blende semiconductors. A mechanical strain ϵ results in the occurrence of an electric response, while the application of an electric field leads to a mechanical stress or deformation (inverse or converse piezoelectric effect). In semiconductor materials, the piezoelectric response to an external strain has linear and quadratic components [Bes06]

$$P_i = \sum_j e_{ij} \epsilon_j + \frac{1}{2} \sum_{kl} B_{ikl} \epsilon_k \epsilon_l, \quad (2.16)$$

where P_i is the strain-induced polarization. When considering zinc-blende crystal structures, the first-order piezoelectric tensor e_{ij} only has one constant $e_{14} = e_{25} = e_{36}$ that needs to be determined, while there are three independent elements, B_{114} , B_{124} and B_{156} , of the second-order tensor B_{ikl} . Calculated values of the constants for GaAs can be found, e.g., in Beya-Wakata et al. [BW11].

QDs grown on (100) surfaces of GaAs or other zinc-blende structures are inherently strained. Strain distributions for pyramidal shaped InGaAs quantum dots have been calculated in References Grundmann et al. [Gru95] and Stier et al. [Sti99] applying a finite-difference scheme to the continuum mechanical model, cf. Equation 2.14. They find a compressive hydrostatic strain component, and additional biaxial and shear components,

which are especially pronounced at the edges of the pyramid.

To determine the influence of internal or externally applied strain on the optical properties of a QD, the effects on the size and position of the electron and hole wavefunctions need to be calculated, which can be done using a strain-dependent 8-band $k \cdot p$ -method [Pry98, Gru95, Sti99]. With the $k \cdot p$ -method, the energy eigenvalues and orbitals are calculated as perturbations of a known solution of the Schrödinger equation describing the charged particle. The 'eight bands' investigated here are two conduction band states (spin up and down) and 6 valence band states, namely heavy-hole, light-hole and split-off bands in both spin configurations. To account for the Coulomb and exchange interaction of multi-particle states, a configuration interaction model can be used. The obtained single-particle states are required to build linear combinations of Slater determinants, such that the few-particle Schrödinger equation can be solved by a linear variational method [Sch09a].

Generally, the calculation results show that the same strain effects that were described for semiconductor bandstructures also hold for the energy levels in QDs, as shown in Figure 2.3. Strain resulting from the growth process of the QD can influence its characteristics, but externally applied strain can also serve to alter and control its electrical and optical properties. Hydrostatic compressive strain causes a decrease in the interatomic distances, leading to an enhanced band gap between conduction and valence band states and thus a larger exciton recombination energy. [Sti99]. Correspondingly, a hydrostatic tensile strain decreases the recombination energy [Din10]. Biaxial strain components influence the aspect ratios of the axes of the quantum dot. In the case where the sign or the amount of strain of the axes perpendicular to the growth direction of the QD are different (unequal biaxial strain), the symmetry group of the structure can be altered. This can lead to a splitting of degenerate energy levels as described above for the two bright excitonic states. In pyramidal QDs, a shear strain was shown to create first- and second-order piezoelectric effects [Sch07]. The linear piezoelectric effect results in charge densities with opposite sign at adjacent edges of the pyramid. The second-order piezoelectric effect creates charge densities with contrary sign, which are only found inside the pyramids. This induces additional asymmetries via the piezoelectric potential leading to further level splitting and shifts of the energy levels. The sign and extend of these effects cannot be generalized as they were shown to depend on the form, size and material composition of the QD [Sch07]. Asymmetries due to internal strain configurations can be compensated by an external strain tuning. If the asymmetries cause the polarization direction of the exciton emission to depart from (110) and (1-10) crystal directions, as described in Section 2.2.1, two external tuning knobs are required to restore the symmetry of the QD and eliminate the fine-structure splitting [Tro15a]. These can either be a biaxial strain combined with an

electrical tuning [Tro14], or two separate strain tuning axes [Tro15b, Wan15].

2.3 Single-photon sources for quantum communication

Secret data communication is usually implemented with an encryption system using a public or private code, or a combination of both. Classical cryptography methods are based on mathematical algorithms that are difficult to solve on a classical computer. Quantum computation, however, can use the correlations between quantum states to encode such data much faster. Factorization problems, for instance, can be solved efficiently using Shor's algorithm [Sho97].

New ways of securing data transfer can be found using quantum states as data bits (qubits). If the qubits are used to share a secret key used for an encryption, we refer to this as quantum key distribution (QKD). The security of QKD is based on the "no-cloning" theorem [Woo82], which says that no identical copy can be produced of a quantum state $|\Psi\rangle = \alpha|0\rangle + \beta|1\rangle$ with basis states $|0\rangle$ and $|1\rangle$ and unknown values of α and β . This can be proven by assuming a unitary operation U creating a clone of the quantum states, which for the basis states results in

$$U|0\rangle = |00\rangle \quad U|1\rangle = |11\rangle. \quad (2.17)$$

With that, by application of U to the general quantum state, we gain

$$U(|\Psi\rangle) = \alpha|00\rangle + \beta|11\rangle \quad (2.18)$$

as a unitary transformation is always linear in the states of the Hilbert space. The contradiction in this step becomes apparent if we calculate the direct clone of the quantum state before insertion of the linear combination

$$U(|\Psi\rangle) = |\Psi\Psi\rangle = \alpha^2|00\rangle + \alpha\beta|01\rangle + \alpha\beta|10\rangle + \beta^2|11\rangle \quad (2.19)$$

which is unequal to Equation 2.18, showing that such an operation cannot exist [Ved06]. If we assume now that we have a sender (Alice) and a receiver (Bob) trying to transfer a secret code using qubits, this makes it difficult for a third party (Eve) to eavesdrop on the information, as Eve is not able to create a copy of the quantum state without being noticed.

A first protocol for QKD has been proposed by Bennett and Brassard in 1984 [Ben84]. The bits are encrypted using two polarization bases of single photons that can be trans-

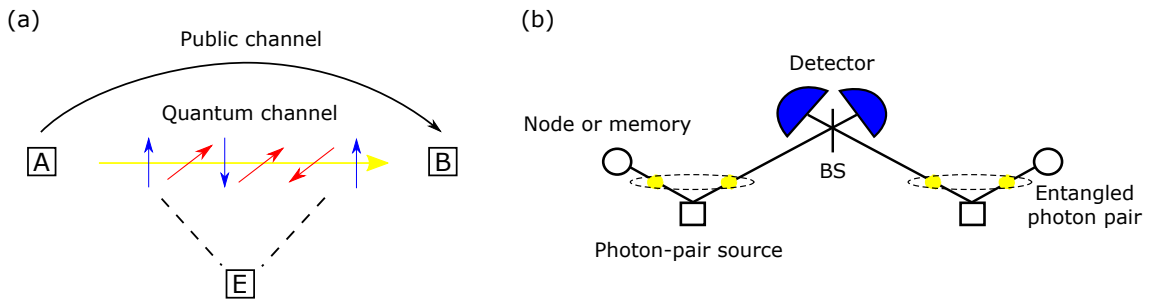


Figure 2.4: (a) Scheme of the BB-84-protocol for QKD. Alice (A) and Bob (B) create a secret key by the transfer of qubits on a quantum channel and additional information on a public classical channel. Eve (E) is trying to eavesdrop on the conversation, but can be detected as quantum mechanics forbids a simple 'cloning' of a qubit. (b) Bell-state measurement for the realization of a quantum network, using two photon-pair sources, a beam-splitter (BS) and two photo-detectors.

ferred between Alice and Bob. For every qubit, Alice randomly chooses the basis in which she sends the information in one of two basic states and Bob likewise chooses a basis in which he measures the polarization state. Afterwards, Alice informs Bob over a classical non-private channel for which bit she chose which basis set, such that they can find out in which cases Bob measured in the same polarization basis. For these values they should get equal results, all other bits will be discarded. If Eve tries to gain information from the transferred code, she must choose a polarization basis, measure the qubit and then emit a new qubit in the same state and basis set. With a probability of 25 % this will result in Alice and Bob measuring different results in the same polarization basis. So to check their transmission for eavesdropping, they can sacrifice a small part of their code and compare the results to find out if they see such an amount of discrepancies.

This basic method already sets high requirements on the single-photon technology. A stream of qubits send with an attenuated laser, or another source with a relevant probability of multi-photon emission events, can be subject to photon number splitting attacks [Bra00]. Eve can separate the redundant photons, wait for the information on the choices for the polarization bases made by Alice and extract the encoded bits. Consequently, a high effort is taken to create single-photon sources with low $g^{(2)}(0)$ values. Sources with low efficiency or high losses during the transfer also increase the risk of an undetected eavesdropper, at least as long as there is no perfect single-photon detector available. In that case the level of dark counts compared to the actual detected signal will make it challenging, or even impossible, to identify an eavesdropper from the error rate in the compared share of the final bits.

Other protocols for QKD make use of entangled photon pairs and their security is based

on the violation of Bell's inequality for quantum mechanical states [Bel64]. Bell proposes an experiment, where Alice and Bob both have one out of a pair of particles and each of them has two measurement apparatuses, A_1 and A_2 , as well as B_1 and B_2 . The possible measurement outcomes shall for simplicity be $+1$ and -1 . If both particles prior to the measurement have a property that creates a fixed independent measurement result in either apparatus, it can be shown for the different expectation values $E(A_i B_j)$ that the following equation holds

$$E(A_1 B_1) + E(A_1 B_2) + E(A_2 B_1) - E(A_2 B_2) \leq 2 \quad (2.20)$$

If the particles are entangled, however, this result does not hold in all cases and the upper limit is

$$E(A'_1 B'_1) + E(A'_1 B'_2) + E(A'_2 B'_1) - E(A'_2 B'_2) \leq 2\sqrt{2} \quad (2.21)$$

To exploit this for QKD, one can follow the protocol proposed by Ekert in 1991 [Eke91]. Alice and Bob use an entangled state for the data transmission, e.g. a Bell state

$$|\Psi^-\rangle = \frac{1}{\sqrt{2}}(|01\rangle - |10\rangle). \quad (2.22)$$

It is possible for them to choose three angles each as a measurement basis, such that for a combination of two of them the two sides of Inequality 2.21 are equal. A relevant deviation from this result identifies an intruder into the communication channel. Alice and Bob choose at least one of the three angles to be equal, such that whenever both of them use this measurement basis, the bits can be used as the code. This protocol requires sources of entangled photon pairs, which, similarly to methods with one photon per bit, should have a high efficiency to avoid detrimental impact by dark counts.

Even with perfect on-demand single-photon generation the losses in optical fibers or the beam broadening in free-space hinder long-distance QKD with the described protocols. To achieve distances above several hundred kilometers, quantum networks need to be constructed. The distance is decomposed into segments with sources of entangled photon pairs. Between two nodes, Bell-state measurements on one photon from each source serve to create entanglement between the other two photons. This method is called entanglement swapping and can create entanglement between remote sources. For a realization of such a network, however, sources of entangled photons with perfectly matching wavelength are needed. In a realistic version, quantum memories will be required, as the Bell-state measurement will not be implemented successfully at all nodes at the same time. Such memories can be based on atoms [Spe11], atomic ensembles [Cho08] or solid state memories

[Tir15], which would all predefine a resonance wavelength, that the single-photon sources need to match. Consequently, tunable sources of entangled photon pairs would be beneficial for the creation of long-distance QKD. Reference Guha et al. [Guh15] gives achievable data transmission rates for quantum-repeater concepts with different component and network conditions. They compare, for instance, the transfer rates of single-photon QKD with a perfect source and detector at typical fiber losses ($\alpha = 0.15$ dB/km at $\lambda = 1.55$ μm) with a quantum-repeater system with efficiencies of the photon-pair sources and detectors larger than 0.9. In this case, a quantum repeater system with only 4 nodes outperforms the single-photon QKD already above a communication length of 260 km.

3 Processing technology for single-photon sources

This chapter describes the nanofabrication processes used in this work to produce single-photon sources with advanced features such as an increased outcoupling efficiency or a tuning mechanism. The growth of the structures by metal-organic chemical vapor deposition (MOCVD) is naturally the first step, which is explained in the following. Subsequently, a crucial processing step is the in-situ EBL for the integration of QDs into microstructures, which is described in detail with all required subprocesses. Flip-chip gold bonding can be used to bring additional features to these samples, such as a backside gold mirror and an integration of the samples onto piezoelectric actuators. Finally the process of two-photon direct laser writing is introduced, which serves to integrate additional optical components on top of the QD microstructures.

3.1 Epitaxial growth of self-assembled semiconductor quantum dots

Since the first realizations of QD structures were achieved in the 1980s [Eki81, Ree88], different techniques for their growth have been developed and refined. In the beginning, 3-D confinement was achieved by lithographic patterning and etching of quantum films [Ils93]. In that way, however, QDs cannot be fully embedded into a semiconductor material and suffer from low luminescence efficiency due to enhanced non-radiative recombination at surface and defect states, especially caused by the etch process. Improved results can be achieved by self-assembled methods, which employ the formation of atomic clusters in an equilibrium state of the material layers. Such epitaxial growth is implemented with either molecular beam epitaxy (MBE) [Cho75] or MOCVD [Man68, Lud85]. For MBE, the growth material is transported by a molecular beam in a ultra-high vacuum, while for MOCVD precursor molecules are used to transport the required material components towards the heated surface, where they can decompose and adsorb, leading to a gradual increase of the crystalline material. MBE leads to lower defect densities and generally a more controlled growth, but has slower growth rates than MOCVD. Moreover, as mentioned in Chapter 2.2.1, QDs can be formed in different growth modes, e.g. strain-induced by Stranski-Krastanow mode or by using droplet epitaxy [Kog93]. The latter serves to create QDs with excellent optical properties, such as a low fine-structure splitting due to

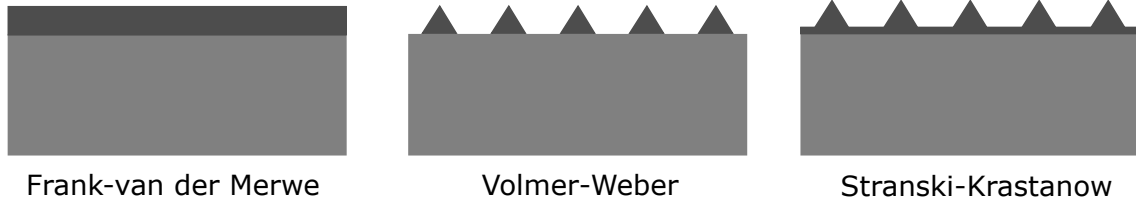


Figure 3.1: Schematic illustration of the three main growth modes in heteroepitaxy: Frank-van der Merwe, Volmer-Weber and Stranski-Krastanow growth.

the high structural symmetry of the structures [Kur13]. Moreover, it allows for a different choice of the QD material combination, such as GaAs QDs inside an AlGaAs matrix, which further contributes to a low FSS due to low interaction with nuclear atomic spins [Hub17]. A drawback of droplet epitaxy is the large size distribution and corresponding variety of the optical characteristics, which can only be overcome by a careful choice of the growth parameters [Hub17, BB18].

In this work, MOCVD is used to form InGaAs QDs in a GaAs matrix material using the Stranski-Krastanow growth mode. The adsorption of GaAs is based on the reaction of arsine and trimethylgallium, which is described by the following formula:



GaAs is grown on the surface of the wafer, while the other reaction product is gaseous. Heteroepitaxy, i.e. the growth of different materials on top of each other, is critically influenced by the chosen materials and their lattice constants a_i as well as by the temperature and pressure inside the chamber [Poh08].

To grow a layer of InGaAs QDs onto GaAs, trimethylindium is added such that an InGaAs alloy can form. The lattice constant of InGaAs can be estimated from linear interpolation of the values for GaAs and InAs ($a_{\text{GaAs}} = 0.5653$ nm and $a_{\text{InAs}} = 0.6058$ nm at room-temperature [Poh13]). As the InGaAs layers adopt the lattice constant of the underlying GaAs, strain is induced which increases with every monolayer, adding strain energy to the system. It settles in the condition with the lowest net energy, which is the sum of strain and surface energies. Three kinds of growth modes can be distinguished, as sketched in Figure 3.1: The formation of a full wetting of the surface is referred to as Frank-van der Merwe growth [Fra49]. In Volmer-Weber growth mode, islands of the adsorbed material are formed on the substrate material [Vol26]. It is observed if the strain energy is high enough so that three-dimensional islands nucleate, decreasing the strain energy while adding additional surface energies. In an ongoing growth, the islands will at some point

coalesce. Stranski-Krastanow growth describes an intermediate situation of the former two: In the beginning, the adsorbing molecules assemble into strained layers, until the strain energy is high enough to favor an elastic relaxation into 3-D surface structures. Small islands are formed on top of a wetting layer with a thickness of at least one monolayer. Afterwards, a capping layer of GaAs is grown, altering the final form and size of the QDs. In this work, truncated pyramids with a width of a few tens of nanometers and a height of less than ten nanometers are utilized.

The areal density of the dots is usually in the range of $1 - 10 \times 10^9 \text{ cm}^{-2}$. For the creation of QD microlenses as single-photon sources, densities of below 10^8 cm^{-2} are required. A growth interruption of 35 s before application of the capping layer allows for a ripening of the islands, which results in a lower density of larger QDs as well as a decrease in the size distribution. Nevertheless, the remaining differences in size and shape of the QDs leads to a significant range of their emission characteristics. As further explained in the next section, deterministic processing methods are required to integrate QDs of a desired emission wavelength into microstructures.

3.2 Nanofabrication with cathodoluminescence lithography

From a QD embedded in planar GaAs matrix material, only approximately 2.1 % of its photon emission are coupled out upwards to a surrounding vacuum or air. If the light is collected from a limited numerical aperture, this value is even smaller, e.g. $\eta^{NA=0.4} = 0.4 \%$. Nanofabrication allows us to integrate the QDs into structures that increase this rate significantly. Photolithography and EBL are the most frequently used techniques to define patterns on top of a full wafer or wafer piece, followed by an etch or metallization step. In a basic implementation, a mask with a regular pattern of devices is used to process the structures at an arbitrary position on the sample. When working with QDs randomly positioned by the self-assembled Stranski-Krastanow growth mode, this leads to a low yield of working devices, as most structures will not be placed above an emitter. Let us assume, that for a successful integration the center of the QD and of the microstructure need to coincide with an accuracy of $r = 100 \text{ nm}$. If the QDs are distributed with a density of $\rho_{\text{QD}} = 10^7 \text{ cm}^{-2}$, we will achieve a device yield of $\pi r^2 \cdot \rho_{\text{QD}} = 0.31 \%$. This means that on average around 300 devices need to be characterized in luminescence measurements before one functioning device is found. Moreover, in most cases the structures will be created for a specific emission wavelength, which is fixed, for instance, by a cavity design. If the emitters are grown with an inhomogeneous broadening of $\Delta\lambda_{\text{in}} = \pm 15 \text{ nm}$

and the bandwidth of the device is $\Delta\lambda_{\text{mode}} = \pm 0.5$ nm, this decreases the probability to gain a functioning device by an additional factor of approximately 0.033. In that case, on average 9000 devices have to be checked to find a combination with a QD that fulfills the spatial as well as the modal requirements. This is confirmed by experiments with QD-micropillar based single-photon sources, where one out of 10.000 structures showed the desired emission characteristics [Uns16]. In that way, a lot of time and sample material are wasted, and scaling up such technologies, e.g. for large scale quantum networks, will not be feasible.

Three different approaches have been found to increase this yield. Firstly, methods for a positioned growth of QDs have been developed by the creation of holes [Meh07, Sch08] or a tailored strain distribution on the sample surface [Kag18], which all favor the nucleation of the emitters at specific positions. QDs aligned to etched nanoholes, however, are limited in their optical quality [Alb10] including a broad linewidth [Chi04] due to an increased influence of charge traps and surface states. A patterned strain distribution can be implemented by precise partial oxidization of buried layers, which avoids a close proximity of the QDs to an etched material surface, but here the accuracy is limited by the size of the oxide apertures [Str12]. Moreover, in both cases a control of the position but not of the spectral characteristics of the QDs is given. The latter can be achieved by techniques that use a pre-characterization of the QD characteristics at cryogenic temperatures, where the positions of suitable QDs are determined with respect to alignment markers. In a second step, these coordinates are used to integrate the chosen emitters into microstructures by use of EBL at room-temperature [Koj13, Sap15].

A significant acceleration of this procedure is gained by deterministic in-situ lithography techniques, which use a characterization method to locate an emitter, directly followed by a processing step that defines a microstructure at the determined position in the same experimental setup.

In this work, a deterministic implementation of EBL is applied which serves to choose QDs by their optical characteristics in cathodoluminescence measurements and integrate them into microstructures with the same tool at cryogenic temperatures. We refer to this method as in-situ EBL or deterministic cathodoluminescence lithography. A similar procedure has been demonstrated based on far-field optical lithography, where two laser beams are required. The first laser is used for excitation of the photoluminescence, but does not affect the applied resist layer, and a second beam at a different wavelength is chosen for the lithography step [Dou08]. In this case, however, the feature sizes are restricted by the Abbe diffraction limit. A further advantage of in-situ EBL is that structures with a varying height profile, such as required for lens structures, can be written, which has not

been demonstrated with far-field optical lithography yet.

To implement in-situ EBL, several processing steps are required: The sample is coated with a resist, the cathodoluminescence lithography is conducted, and finally the defined structures are developed and etched. All details of these steps are described in the following.

3.2.1 Setup for in-situ 3-D electron-beam lithography

To implement the in-situ EBL a scanning electron microscope (SEM) *Jeol JSM-840* has been customized with equipment for cathodoluminescence measurements, as well as with a sample carrier suitable for cooling with liquid helium. Details are shown in the schematic overview in Figure 3.2. The electron beam is formed by thermal emission from the tip of an LaB_6 -crystal, which is heated by a gun current of approximately 3 A, and an acceleration voltage at the anode that is adjustable between 3 and 20 kV. The electron beam, which is focused and deflected by magnetic coils, can be blanked by a *DEBEN-PCD Beam Blanker* with integrated Faraday-cup to measure the actual electron current. The sample is positioned in a 90° angle to the electron beam on a movable holder that can be cooled by a liquid helium flow to below $T = 8$ K. To achieve a sufficient thermal and electrical contact to the coldfinger, the sample is fixed with a conductive silver lacquer. A cooling trap filled with liquid nitrogen and a turbo-molecular pump serve to achieve a pressure of below 10^{-6} mbar inside the vacuum chamber. In addition to a detector for secondary electrons (SE) on one side of the chamber, an elliptical mirror has been positioned above the sample on the other side to collect the luminescence of an excited sample area. It can be adjusted with two micrometer screws, such that the collected light is coupled out of the adjacent side of the chamber onto the entrance slit of a monochromator *Acton - SP 2500* equipped with three different gratings. For the samples introduced in this work, a grating with 1200 lines/mm and an entrance slit width of $100 \mu\text{m}$ are chosen. Behind the monochromator a liquid-nitrogen-cooled Si-charge coupled device (CCD) camera *Princeton Instruments - PYLON* with pixel size $20 \times 20 \mu\text{m}^2$ and an array of 1340×100 pixels serves to visualize a spectrum with a resolution of $\Delta\lambda = 0.15$ nm.

For the luminescence measurements as well as for the lithography process it has to be taken into account that the primary electrons hitting the sample undergo several types of elastic and inelastic scattering processes, such as backscattering by atoms or the excitation of secondary electrons. Consequently, a drop-shaped volume of the exposed sample is excited, which increases with the chosen acceleration voltage. According to the model of Kanaya-Okayama, the penetration depth of electrons with an energy of 10 keV in GaAs relevant for our process is approximately $0.5 \mu\text{m}$ [Kan72, Yac86]. The excitation

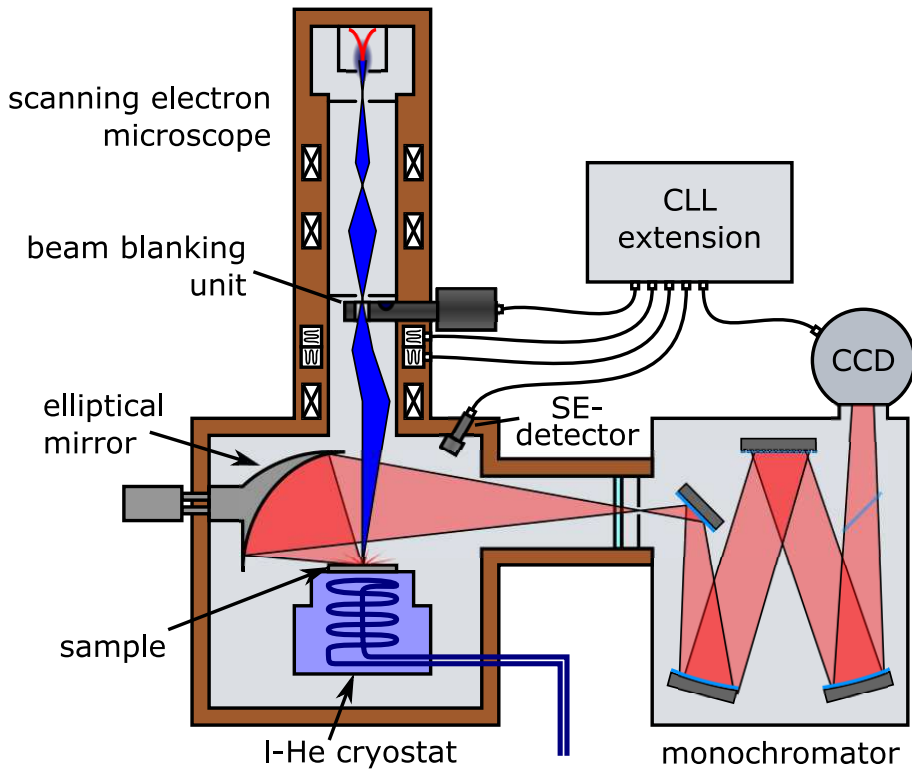


Figure 3.2: Schematic overview of the customized scanning electron microscope used for the in-situ electron-beam lithography, taken from [Hei17]. In addition to the standard equipment with a vacuum chamber, gun, deflection coils and detectors, e.g. for secondary electrons (SE), a liquid-flow helium (l-He) cryostat has been added to cool down the samples to cryogenic temperatures, while the cathodoluminescence can be dispersed by a monochromator and detected by a Si-charge coupled device camera (CCD).

range is further increased by charge carrier diffusion, which decreases with temperature and with the density of impurities in the material. For a GaAs sample at $T = 6.5$ K the excitonic diffusion length was experimentally estimated to approximately 250 nm [Rod06]. In vertical direction, the diffusion length can be reduced by the growth of anti-diffusion barriers of a material with larger bandwidth, such as AlGaAs for GaAs samples. The effective increase of the pixel size of lithography structures due to scattering or diffusion is called proximity effect.

3.2.2 Resist characteristics

A key feature for our 3-D in-situ EBL technique is that the utilized lithography resist has specific characteristics depending on the applied exposure dose. We use *AR-P 6200 (CSAR 62)* from the company *ALLRESIST GmbH*, which is based on the polymer

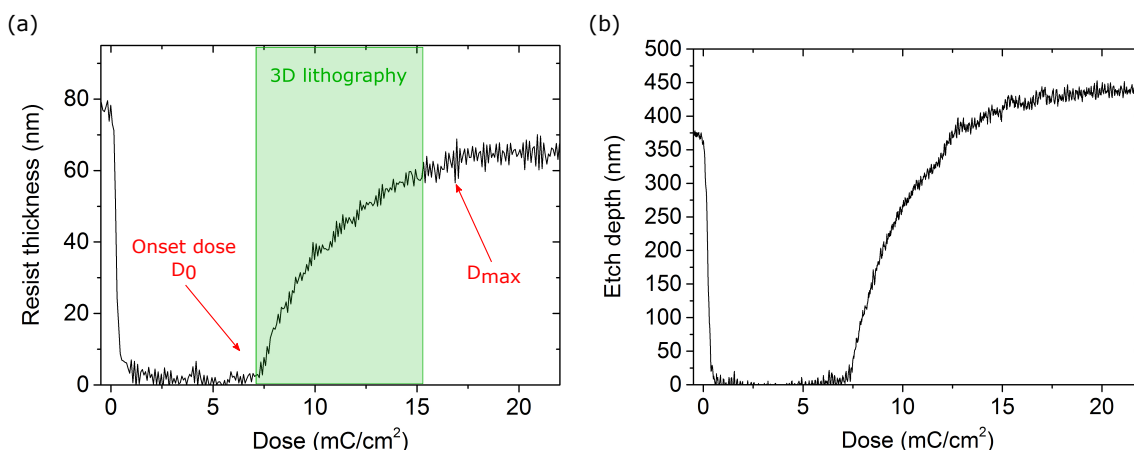


Figure 3.3: Characteristics of the electron-beam resist AR-P 6200 depending on the applied electron dose: (a) Resist profile after exposure and development. (b) Height profile transferred to a GaAs sample after dry etching of the resist profile in (a).

Poly-(α -methylstyrene-co-methylchloroacrylate). Figure 3.3 (a) shows the depth profile of the resist after exposure and development, depending on the applied electron dose for a resist thickness of 80 nm and an acceleration voltage of the electron beam of 10 kV. A positive-tone behavior can be observed for a low dose which stays unchanged up to a value of approximately 7 mC cm^{-2} , which we refer to as the onset dose D_0 . During the positive-tone exposure molecule-chains are sliced into smaller components, which can be carried away by the developer. For in-situ EBL this regime is used for the collection of the cathodoluminescence signal of a small sample area. If an exposure above the onset dose is applied, the chains will start to crosslink again and thus become increasingly insoluble to the developer. Beyond a threshold dose of D_{max} , which for an acceleration voltage of 10 kV lies at around 15 mC cm^{-2} , the resist is fully inverted. It has a slightly decreased thickness as compared to the unexposed resist due to the outgassing of HCL and other scission products [Oya12]. The steepness of the rising flank of the resist thickness can be characterized by the contrast $\gamma = \frac{-1}{\log(D_0/D_{max})}$, which decreases with temperature and increases with the the chosen acceleration voltage [Kag16]. A low contrast allows for 3-D structures such as microlenses to be written by patterning with varying exposure doses. If structures with steep vertical flanks shall be created, a high contrast is favorable, which can be achieved at high acceleration voltages. At the same time, the absolute values of onset and threshold dose move to higher values with increasing acceleration voltage, which allows for higher exposure times and thus a higher signal-to-noise ratio of the collected luminescence signal. In this work, we mainly aim for the creation of microlenses, which is why an acceleration voltage of 10 kV is chosen as a compromise between a low contrast

and sufficiently high dwell times for luminescence collection.

The same feature of exposure-dependent positive- and negative-tone regimes was found for the resist Polymethylmethacrylat (PMMA), but at cryogenic temperatures it requires a very precise choice of the dose parameters to gain a high device yield [Sch16b]. For that reason, it is not utilized in the context of this work.

To prepare a sample for in-situ electron-beam lithography, it is cleaned in a cleanroom environment (Class 100) with acetone and isopropanol at $T = 70$ °C for 5 min each. The sample is spin-coated with the resist *AR-P 6200.04*, which is the version with the lowest available solids content of 4 %. Spinning at 3000 rotations per minute for one minute results in a thickness of approximately 85 nm. Afterwards, a softbake is required at $T = 150$ °C for one minute to reduce the moisture content in the resist. Then the sample is ready to be placed into the setup for in-situ EBL.

3.2.3 Cathodoluminescence measurements and deterministic lithography

The major advantage of in-situ EBL is that the analysis of the cathodoluminescence signal of the QDs and the lithography of the microstructures can be conducted repeatedly in directly consecutive steps on small areas of the sample. For the investigation of the cathodoluminescence, a combination of an AD-DA-converter card controlled with a *LabVIEW* program allows to scan the sample with a variable pixel size, which is usually set to 500 nm. The exposure and integration times for each pixel are chosen such that the applied electron dose stays below the onset dose of the resist. In that way, the resist above the mapping areas will be washed away during development and the GaAs can be removed in the etch process down to the QD layer. Typical exposure times lie between 10 and 15 ms for an acceleration voltage of 10 kV. To make sure that the dose is distributed equally on the respective pixel, the beam is moved in a meandering pattern while the luminescence is collected. After each pixel the beam is blanked and the spectrum can be read out and saved, such that overall around 50 ms are required per pixel. This is repeated pixel by pixel until a luminescence map is gained such as shown in Figure 3.4 (a). Different emitters can be clearly located and single lines identified, as plotted in Figure 3.4 (b). To find the exact position of a QD the integrated intensity of its emission lines over an area of 6×6 pixel is fitted with a 2-D Gaussian, such that the location of highest intensity can be identified.

One or several suitable QDs are chosen from each map for integration into a microstructure. The emitter can be picked in a required wavelength range and by selection of the brightest cathodoluminescence lines. The resolution of the spectroscopy system gives an accuracy of 0.15 nm, however the QD emission characteristics can vary between different

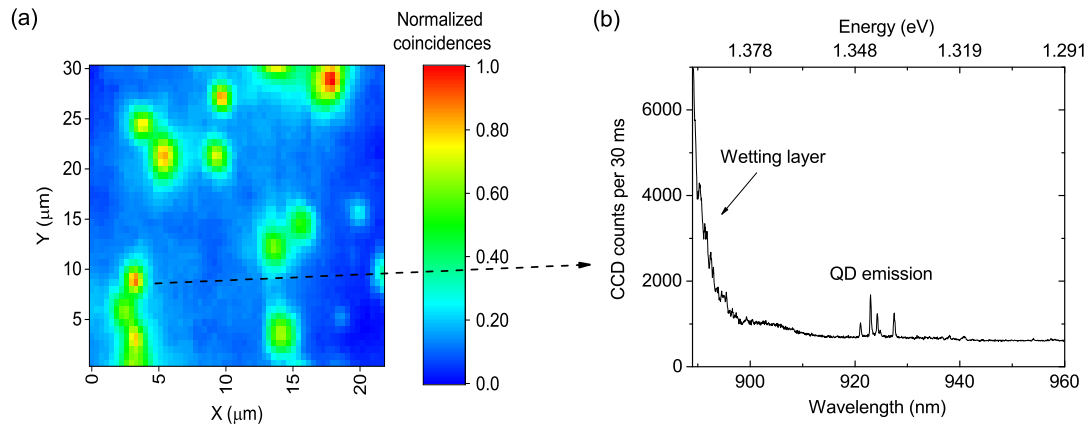


Figure 3.4: Cathodoluminescence measurements taken at $T < 8$ K: (a) Cathodoluminescence map at energies between 1.32 eV and 1.36 eV of a sample with suitable quantum dot density for in-situ EBL of around $3 \cdot 10^{-6} \text{ cm}^{-2}$. (b) Spectrum from a bright quantum dot.

cooldowns due to a changing electrical environment. Consequently, a realistic estimate for the precision of in-situ EBL is $\Delta\lambda = 0.3$ nm. The writing process should be started immediately after the pre-selecting the QDs to minimize the impact of parasitic influences such as a sample drift of approximately 5 nm per minute. For lenses or other structures with a 3-D height profile, the electron dose range for 3-D lithography can be used. Lenses are written by the exposure of circular patterns with radially decreasing exposure time, which results in an outwards decreasing resist thickness after development. Flat structures are written by choosing a constant exposure above the threshold dose D_{max} .

3.2.4 Processing of deterministically written microstructures

After the in-situ EBL process, the sample is transferred back to the cleanroom to be developed and etched. To develop the resist, the sample is dipped for 30 s into developer *AR 600-546* from *ALLRESIST GmbH* (main component Amylacetat), for 20 s into isopropanol and finally for 30 s into deionized water to stop the development. The chemicals and development time were chosen to give smooth surfaces as well as suitable dose characteristics, as the onset dose and the dose window for 3-D lithography can be influenced in this step.

To transfer the developed structures into the GaAs material, inductively-coupled plasma reactive-ion etching (ICP-RIE) is implemented in the *ICP-RIE SI 500* etching system from the company *Sentech*. After positioning of the sample inside the vacuum chamber, argon, boron trichloride and chlorine are introduced into the chamber with controlled

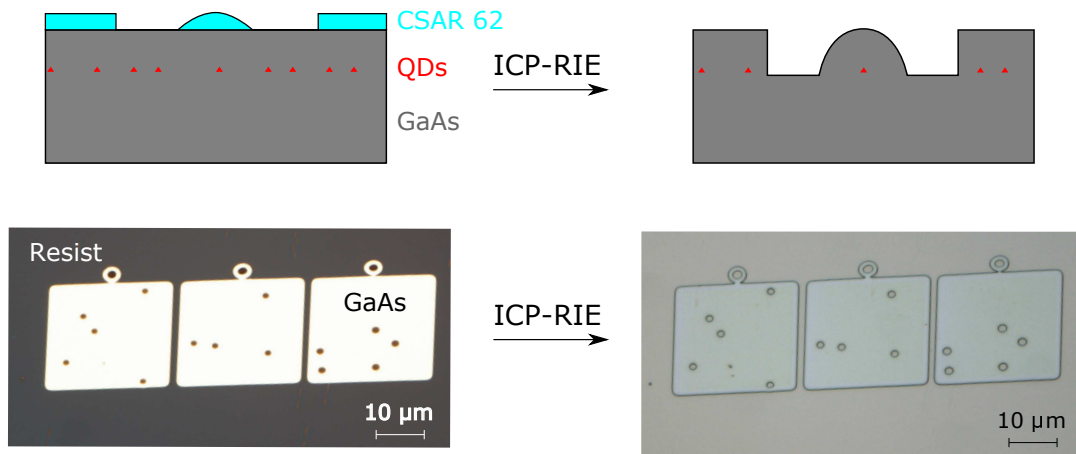


Figure 3.5: Sketch and microscope images to visualize the etch process used for QD microlenses written by in-situ EBL: Inductively-coupled plasma reactive-ion etching (ICP-RIE) is applied to transfer the structures into the semiconductor material. The resist is washed away in the mapping areas such that the GaAs is etched down to the level of the quantum dot layer outside specifically written microstructures.

rates. An antenna generates radio-frequency electromagnetic fields that create a plasma, from which ions are accelerated towards the sample. The ablation of its surface includes physical (sputtering) as well as chemical reactions. This combination results in a highly anisotropic (vertical) etch procedure which is desirable to transfer the structure as written into the GaAs material. At the same time a selectivity between different materials is maintained due to different reactions with the accelerated ions. We observe an etching of the CSAR 62 resist of 1:4.9 in comparison to GaAs, such that thin layers of resist can be used to transfer structures almost five times deeper into the resist, such as shown in Figure 3.5. When etching samples structured by in-situ EBL, it is crucial to choose the required etch time and corresponding etch depth with a high accuracy. If the parameters are set too low, the 3-D profile will not fully be transferred into the resist and the QDs in the map around the structure will not be removed. This results in undesired stray light contribution from neighboring emitters when implementing photoluminescence measurements. If the etch depth is too high, the 3-D structures will turn out smaller in radius and the vertical position of the QD will be altered. Consequently, an etch dummy is used prior to the processing of a QD sample, as the etch rate can vary with parameters such as the sample size or the chamber condition influenced by previous processes. The dummy is coated with the same resist which is partly removed to create an edge. After etching the dummy sample, the etch depth can be determined by measuring the height of the edge using the profilometer *Ambios XP2*.

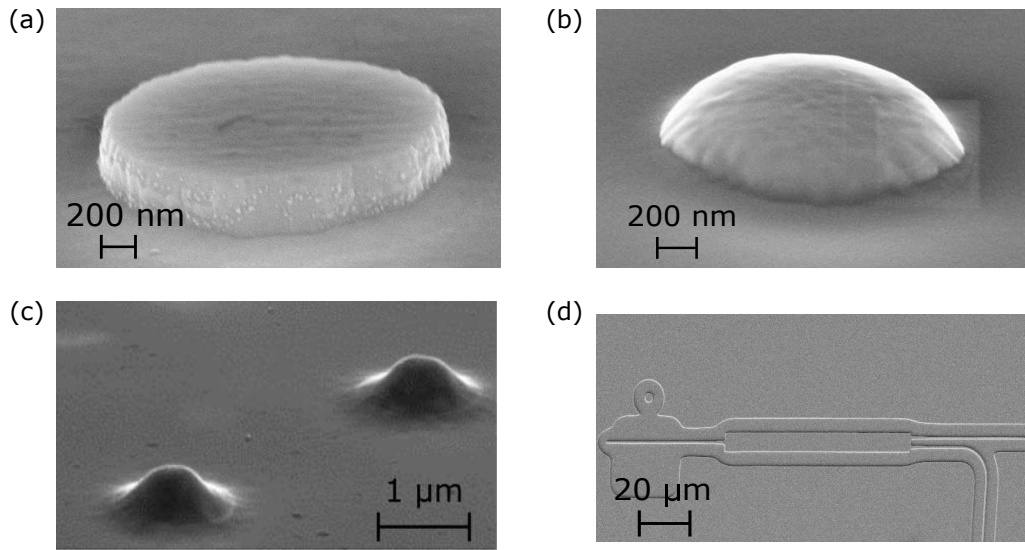


Figure 3.6: Images of structures created by in-situ electron-beam lithography taken by scanning electron microscopy. (a) Mesa structure. (b) Hemispherical microlens. (c) Gaussian microlenses. (d) Waveguides and multi-mode interferometer [Sch18b].

Different kinds of QD-based structures have already been realized using in-situ EBL. Figure 3.6 shows SEM images of a micromesa (a) and a hemispherical microlens (b), which are further introduced in the following chapters. Gaussian lenses (c) give a slightly altered emission profile compared to hemispherical lenses, and waveguide structures (d) allow for quantum optical experiments to be implemented on-chip [Sch18b]. For all of these structures, the precise alignment to a QD with the targeted emission wavelength is crucial for optimum device performance, e.g. in terms of maximum photon-extraction efficiency. Consequently, it is highly beneficial to use a deterministic in-situ processing technique.

3.3 Bonding techniques for semiconductor samples

Different applications in semiconductor device processing need a semiconductor sample to be permanently placed on a carrier of the same or a different material. This can be required during packaging of devices or to stack a semiconductor upon a material that it cannot be grown on. Prominent examples are the creation of silicon-on-insulator transistors [Las86], packaging of MEMS (microelectromechanical systems) technology [Col00], the integration of III-V semiconductor lasers to silicon photonic circuits [Roe07] or the construction of efficient solar cells by stacking different semiconductor materials [Dim14]. In this work, a GaAs sample with InGaAs quantum dots is bonded by a flip-chip technique onto a gold surface, firstly to increase its extraction efficiency by using the gold layer as a backside

mirror. Secondly, the gold layer can connect the sample to a piezoelectric actuator, which allows one to implement a strain tuning of the QD emission.

Several methods can be used for the permanent bonding of samples or full wafers. Requirements on the bond result can include electric conductivity, temperature stability and elasticity parameters allowing for a strain transfer. In many cases, even sub-micrometer thin layers of the original sample are to be transferred onto the carrier, although they were grown and processed on a substrate of several hundred micrometer thickness. In that case, a flip-chip approach is usually applied, where the active layers are grown in a reversed order, such that the sample can be placed face-down onto the carrier. After the realization of the bond, the substrate is removed by etching or lapping. Often, a stop layer for the etch process is integrated during epitaxy or by implantation, which is removed in a second, more gentle etch step to protect the thin active layers.

All bonding methods in direct or flip-chip implementation share similar basic steps, which are visualized in Figure 3.7:

1. Preparation of the carrier and the sample by cleaning, polishing or application of an interconnect layer.
2. Bringing carrier and sample into contact, either in air or optimally in vacuum. Contact forces form a first bonding between carrier and sample.
3. Activation or strengthening of the bond by e.g. an increased temperature or a perpendicular force.
4. When using a flip-chip approach: Etching or lapping of undesired material of the upper sample.

The most prominent versions are a bonding mediated by adhesives, thermocompression bonding and ultrasonic bonding, which will be described in more detail in the following.

3.3.1 Bonding with adhesives

A wide variety of polymers, such as epoxy adhesives, can be used to fix a sample on a carrier. For most commercially available adhesives, however, the characteristics at high and low temperature (below 100 K) are unknown or material degradation at such temperatures has been observed [Mar15]. Other materials usually used as photoresists or planarization material in semiconductor technology can also serve as an intermediate layer for bonding. Prominent examples are benocyclobutene (BCB) [Wie06, Ryu10], PMMA [Eat94], SU-8 [Wie06, Yu06] or spin-on glass materials, e.g. hydrogen silesquioxane (HSQ) [Ryu10].

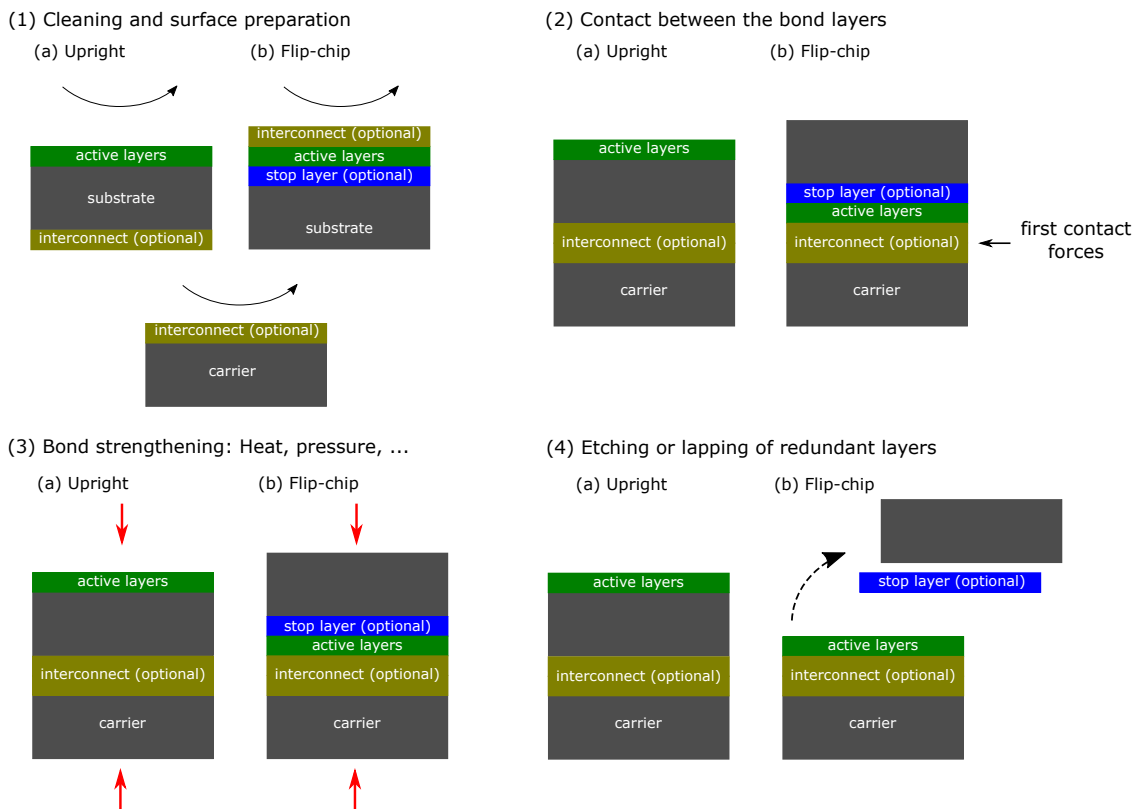


Figure 3.7: Sketch of the basic steps of (a) a normal or (b) a flip-chip bond process: (1) Polishing of the surfaces (if required) and cleaning with solvents or oxygen plasma. If necessary, an interconnect layer, e.g. an adhesive, can be applied. (2) Sample and carrier are brought into contact either upright or upside-down. (3) The bond forces are increased depending on the respective bond method, e.g. by heating the samples or pressing them together. (4) If a flip-chip procedure is applied, the upper sample substrate is removed by lapping or wet etching.

They are all liquid at room-temperature but harden above a certain curing temperature. To bond a sample onto a carrier, the polymer is spin coated or spray coated onto the carrier substrate in a thin layer of a few hundred nanometer, which is usually followed by a baking step for the removal of solvents. Next, the sample to be bonded is pressed onto the carrier such that the polymer can come into full contact with its surface and slight surface irregularities are filled up. Finally, the samples are heated to temperatures such as 180 °C for BCB [Nik01], 220 °C when using SU-8 [Zis17] and 400 °C for HSQ [Ryu10], such that the polymer is hardened and a stable bond is formed. An advantage of this technique is that small surface irregularities are compensated, as they are filled up by the adhesive material. Moreover, as compared to other bonding methods, the temperature and pressure required during the process are rather low. Most adhesives, however, do not

give a conductive connection between the sample and its carrier and the adhesive materials can be quite expensive.

3.3.2 Direct bonding by surface attraction forces

Samples or wafers with a flat and clean surface can be bonded simply by the attracting forces between their surfaces [Las86, Shi86]. The most important effects contributing here are capillary, electrostatic and Van der Waals forces, as well as hydrogen bonding between OH groups. Semiconductor surfaces are hydrophilic under room-temperature conditions, such that they bond in a first step by forming networks of water molecules. The samples are heated such that the water molecules desorb and leave molecule groups linked via hydrogen atoms and OH groups behind [Ste89]. With annealing temperatures up to 1000 °C applied, very stable bonds can be formed.

An alternative is the bonding of hydrophobic surfaces, which can be achieved by removing oxide layers with diluted hydrofluoric acid. In that case, the bonding is achieved by hydrogen and fluorine bonds, which is again increased by an annealing step [Ton94].

Direct bonding of samples or wafers can achieve excellent bond characteristics, but the high annealing temperatures require a high temperature stability of the samples, which is not given e.g. when working with semiconductor QDs.

3.3.3 Thermocompression gold bonding

Instead of using high temperatures to achieve high contact forces, a combination of pressure and temperature can serve to bond surfaces of suitable materials. Whenever an electric connection between sample and carrier is required, it is advantageous to use metallic contact interlayers. In most cases, gold is used as the bond material as it has a moderate melting temperature of 1064 °C, a rather low hardness with 2.5 on Moh's scale and with this also a low yield stress (stress required for permanent deformation of a material) [Hab13]. Moreover, it is oxidation resistant, which is advantageous as oxides hinder the bond formation, and has a high electrical conductivity.

For many applications, not full dies or wafers are bonded, but only parts of the sample are equipped with metallic structures called "bumps", which are pressed onto metallic layers on the carrier to achieve an electrical contact. The processes involved are comparable, however, to a full surface bonding procedure:

The carrier is usually covered with a layer of the same metal as the active sample. Deformation as well as diffusion effects contribute during the thermocompression bonding. When the process starts, at first only microscopic deformation takes place, as the surfaces are in contact merely by a few spikes and asperities. The pressure experienced by these

small areas is very high such that they are easily deformed and flattened, until the two surfaces are in almost full contact [Two98]. Then, atoms are moved on the full contact face resulting in a macroscopic deformation and intertwining between the two samples. Due to deformations in the crystal structure, the required stress per acquired strain increases with the stress applied, which is referred to as work hardening of the material. It was shown in Reference Condra et al. [Con75], however, that at sample temperature above 300 °C this effect decreases for gold, such that higher deformation is achievable. In addition to that, the elevated temperature increases the atomic diffusion between the two samples, resulting in a strengthening of the bond.

Different results can be found on the amount of pressure and heat required for strong Au-Au bonds. 7 MPa at 300 °C were used for 10 minutes by Tsau et al. [Tsa02] to bond 50 µm-thin gold stripes. They analyzed their bond strength by a four point bending approach resulting in a strain energy release rate between 22 and 67 J/m². In Reference Drost et al. [Dro98], 5 x 5 mm² chips were bonded at temperatures between 350 °C and 450 °C and pressure rates between 0.04 and 2.22 MPa for one minute at the peak temperature. Afterwards, they were tested with a pull force of 16 MPa and their electrical conductivity was confirmed. It was found that the yield of sufficiently bonded devices was not increased above a pressure of 0.13 MPa. However, they noted that they did not achieve a continuous bond on a large surface but rather many small local joints between the gold layers.

An important advantage of thermocompression bonding is that it creates conductive connections between sample and carrier and works at lower temperatures than e.g. direct wafer bonding. Bond equipment for the application of temperature and pressure is required, which can either be bought as commercially available systems or can be implemented using a simple spring press and a hotplate.

3.3.4 Thermosonic bonding

The temperature, pressure and duration required in thermocompression bonding can be reduced by adding an additional source of energy by ultrasonic vibrations. This method is also referred to as thermosonic bonding, and was adopted from the thermosonic wire bonding technique used in the packaging of integrated circuits [Joh76]. The vibrations can be applied either horizontally or vertically to the bond area. It has been shown that the resulting acoustic radiation removes contaminations between the surfaces and significantly softens the materials [Krz90]. Typical parameters for the ultrasonic bond process are a temperature of 180 °C, an ultrasonic power of 15 W/cm² and a pressure of 30-40 MPa for 500 ms [Kan95].

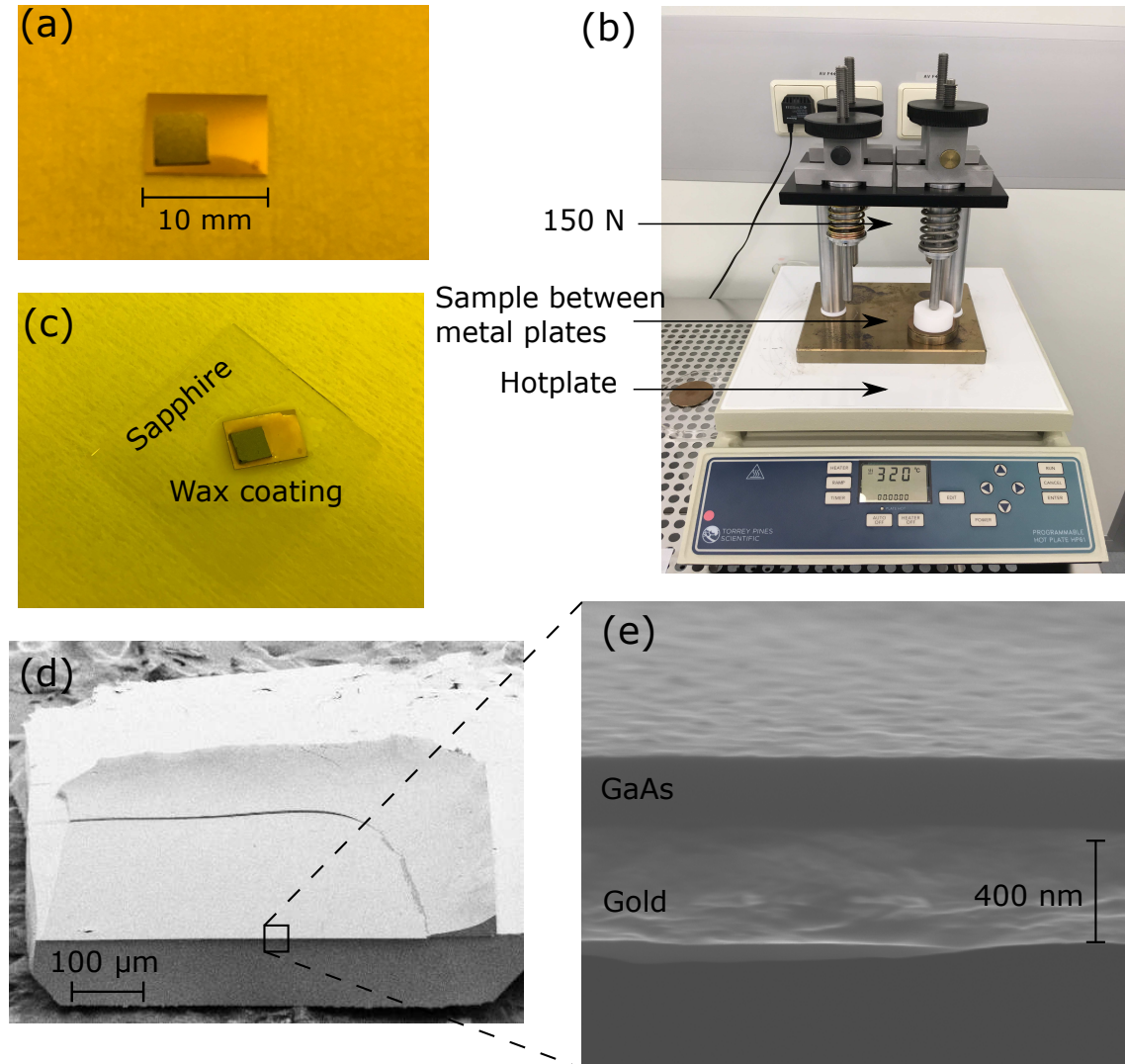


Figure 3.8: Illustration of the flip-chip thermocompression gold bonding with InGaAs QD structures: (a) Sample and carrier are brought into contact with the gold layers facing each other. (b) A spring press on a programmable hotplate is used to apply a pressure of 6 MPa at a temperature of 320 °C. (c) To remove the substrate by wet etching, the sample is coated by a wax layer to protect the sides and the bottom of sample and carrier. (d) SEM image of the etched GaAs surface of a cleaved QD sample bonded onto a GaAs carrier. (e) Close-up of the bonded gold layers with a thin GaAs layer on top (430 nm in this case).

Thermosonic bonding is advantageous for samples which need to be bonded at low temperatures. Due to a very short bond time, it is also applicable for industrial applications with high sample volumes. The bond equipment, however, is difficult to construct in a customized build, as highly sensitive ultrasonic piezoelements are required. Alternatively, it can be acquired as a commercially offered system at high costs.

3.3.5 Flip-chip thermocompression gold bonding of GaAs quantum dot samples

In the scope of this work, InGaAs QD samples are bonded onto GaAs carrier substrates or piezoelectric actuators. Flip-chip thermocompression gold bonding was chosen for this procedure, as its processing temperature stays below 600 °C, where annealing effects on QDs can be observed [Mal97, Hei98]. Furthermore, gold interlayers can be used, which is an advantage as the gold layer of the bonded sample can serve as a backside contact. By using a flip-chip approach, the QDs can be brought in close vicinity to the gold layer, such that their downward emission is reflected upwards for a higher light extraction out of the GaAs sample. Finally, the thermocompression bonding can be implemented with rather basic and low-cost equipment, as presented in Figure 3.8 (b).

The bond process starts by evaporation of 200 nm of gold onto the sample and the carrier. After a thorough cleaning of the gold layers with acetone and isopropanol, the QD sample is turned upside-down and the gold layers are brought into contact, as shown in Figure 3.8 (a). The samples are placed between two metal disks and inserted into the spring press, which is positioned on a hotplate. The springs induce a pressure of 6 MPa for a sample size of 25 mm². The temperature is ramped upwards and downwards with steps of 50 °C in 10 min. The maximum temperature of 320 °C is held for 4 h. After the bonded sample has cooled down, it is taken out of the press and prepared for the removal of the GaAs substrate situated above the QD layer. For that purpose, it is fixed on a thin piece of sapphire with a wax that melts above 50 °C. The wax is used to cover the sides of the carrier and the upper sample, such that they are protected from the etch solution. Only the top of the QD sample remains uncovered. The sample is ready for the substrate removal, which starts with a hydrogen chloride (HCL) dip for 30 s to remove surface oxides. Then, the sample is rinsed in water for one minute, before it is placed into a stirred solution containing 100 ml of hydrogen peroxide (H₂O₂) and 10 ml of ammonium hydroxide (NH₄OH). H₂O₂ serves to oxidize the surface to be etched, while NH₄OH dissolves the oxides such that they can be carried away. The etch process is highly selective towards AlGaAs, which is used as the etch stop layer [Log73]. As this etch process is restricted by the mass transport and not by the oxidization rate, stirring the solution at a high frequency is essential. After approximately 60 minutes, the bare AlGaAs layer is

visible and the sample is taken out to be rinsed in water. 10 s in hydrochloric acid are sufficient to remove the AlGaAs. After another rinsing process, the sample can be cleaned from the wax and is ready for further processing steps. As shown in Figure 3.8 (d), a small rim of GaAs and AlGaAs can remain on the sides of the surface, as the etch procedure usually distributes from the middle to the edges of the sample.

3.4 Two-photon direct laser writing

While conventional optical lithography is limited to (2-D) patterns transferred into a resist, the non-linear effect of two-photon absorption in photoresists [Pao65] can be used to create 3-D polymer microstructures [Wu92, Mar97, Sun99]. Two-photon absorption was initially predicted by Göppert-Mayer in 1931 [GM31] and experimentally verified by Kaiser and Garrett in 1961 [Kai61]. It describes how two photons can be collectively absorbed to bring an atom into an excited state, which has an excitation energy that corresponds to the sum of the energy of the two photons. As the probability of this effect is proportional to the squared optical power, it can be limited to the focal spot of a laser beam, which allows for a creation of 3-D structures by illuminating areas of a photoresist in a layer-by-layer fashion. This enables an additive fabrication of structures on the micrometer scale using negative-tone UV sensitive resists that are exposed to tightly focused IR laser pulses.

When using 2-D optical lithography, photoinitiators start the photopolymerization by absorption of one UV photon. This leads to the creation of free radicals that finally induce the cross-linking of polymer chains. They become insoluble in the developer, whereas unexposed areas are removed in the development step. For direct laser writing, the same process is activated by the absorption of two IR photons. The exposed volume is referred to as a "voxel", whose size is limited by the focal region of the laser beam.

The resolution of the 3-D femtosecond direct laser writing depends on the size of the focal volume of the laser in which the squared intensity lies above the threshold required for two-photon absorption. One has to take into account, however, that intensities of neighboring voxels can add up if they are close enough for their profiles to overlap. In that case the resist is said to have a memory effect, which is the case for most polymers. To determine the resolution acquired, Sparrows criterion can be applied: It states that two spectroscopic lines can still be distinguished, as long as there is a local minimum in between them [Spa16]. Adopting this to direct laser writing by two photon absorption means, that two voxels are still separable as long as the local minimum in between the two maxima of the squared sum of their overlapping intensities times the exposure time lies below a certain threshold value, at which the resist becomes insoluble. This threshold is

determined by how many two photon absorption processes are required to generate enough photoinitiators to start the crosslinking [Fis13]. An illustration of the comparison between a resist with and without memory effect is given in Figure 3.9, where the threshold value is set for a fixed exposure time. For a reduction of the memory effect, a deactivation of active photoinitiators either by chemical effects by so called "quencher" molecules can be used [Sak12], or a second donut shaped inhibition laser profile can be applied [Fis10]. With the former, a resolution below 100 nm [Gan13] could be achieved, while the latter so far allows for a resolution limit of below 400 nm [Duo17]. When estimating the resolution in all three dimensions, one has to consider that the focal length of a laser spot is usually smaller in axial direction than on the lateral axis.

All structures produced by femtosecond direct laser writing in this work are fabricated at the University of Stuttgart by the 4th Physics Institute using a commercially available 3-D laser lithography system (*Photonic Professional GT* by *Nanoscribe GmbH*). The applied resist is distributed by the same company and is called *IP-Dip*. The photoresist is used as an immersion medium such that sample and writing objective are in direct contact with the resist, which is also referred to as a dip-in approach [Büc12]. This allows to overcome the limitation in the height of the structures by the trade-off between working distance of the writing objective and resolution of the focal spot. Moreover, it avoids aberrations at the interface between air and photoresist. Structures of up to millimeters in height

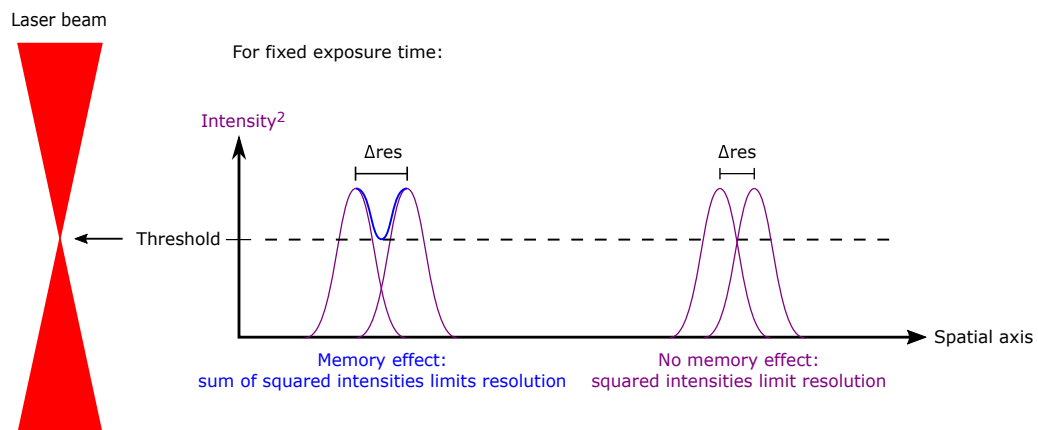


Figure 3.9: The sketch illustrates how the memory effect in the resist influences the resolution of 3-D direct laser writing: The two photon absorption increases with the squared intensity of the exposure. Above a certain threshold of accumulated absorptions, the resist becomes insoluble to the developer. If the resist underlies a memory effect, the sum of the squared intensities of neighboring voxels together with their exposure times determine the distance at which they can still be separated from each other. In a resist without memory effect, the distance of the voxels can be reduced and is only influenced by the width of the beam at the threshold value of the resist.

are possible with that technique. After the exposure, the sample is bathed for several hours in the developer *mr-Dev 600* (*Micro Resist Technology*), before a final cleaning with isopropanol is applied. According to the data sheets published by the company, the combination of lithography system and resist allows for feature sizes below 200 nm in all axial dimensions.

4 Photoluminescence measurements

The single-photon sources investigated in this thesis are designed to be driven by optical excitation. To determine their optical and quantum-optical properties, they are mounted in a liquid-helium flow cryostat at base temperatures of about 10 K. For optical excitation a continuous wave or pulsed laser is used and focused onto a small area of the sample by a microscope objective. The photoluminescence is collected through the same objective, spectrally dispersed by a monochromator and either detected by a CCD camera or by single-photon sensitive detectors. This type of analysis is called micro-photoluminescence spectroscopy. In the following, the used measurement setups will be described in detail, followed by specific measurement techniques that are exploited to characterize the extraction efficiency, the lifetime and the suppression of multi-photon emission events achieved with the developed quantum-light sources. In the last section, a setup for the investigation of fiber-coupled single-photon sources is described.

4.1 Micro-photoluminescence spectroscopy

To characterize the single-photon sources fabricated in this thesis, two different micro-photoluminescence setups are used, which in their basic structure follow the schematics of the beam path shown in Figure 4.1. The setups will be labeled as Setup A and Setup B. In both laboratories a *LabVIEW* program is used to control the actuators for sample positioning as well as the data acquisition. The sample is mounted onto a coldfinger comprised in a liquid-helium flow cryostat. To ensure a sufficient thermal contact between the coldfinger and the sample, conductive silver lacquer is used. The vacuum chamber is connected to a turbo-molecular pump such that the ambient pressure can be reduced to $p < 10^{-6}$ mbar. Afterwards, liquid helium is transferred through the coldfinger to bring the sample to cryogenic temperatures. The sample temperature can be measured by a silicon diode and adjusted by tuning the helium flow as well as by using a heater element below the coldfinger in combination with a proportional-integral-derivative (PID) control loop.

A glass window is integrated in the cryostat above the sample surface to allow for optical access. The cryostat as well as the microscope objective facing the window are mounted

onto translation stages to allow for coarse and fine positioning of objective and sample. To locate microstructures on the sample surface, a white-light source is coupled to the beam path, such that an image of the sample surface can be collected by a CMOS (complementary metal-oxide semiconductor) camera. The laser used for optical excitation is a tunable Titanium-Sapphire laser (*Tsunami HP fs 10 W* from *Spectra Physics*) in the case of Setup A, while Setup B is equipped with a diode laser (*PicoQuant, LDH Series, Picosecond Pulsed Diode Laser Heads*) emitting at $\lambda = 665$ nm. The excitation power can be adjusted with an automated filter wheel. At a beam splitter, 90 percent of the laser emission are directed onto a powermeter to evaluate the excitation power, while 10 percent of the laser emission are focused through the microobjective (*M-Plan APO NIR 20x* from *Mitutoyo*) with a numerical aperture (NA) of 0.4 and magnification by a factor of 20. A minimum excitation spot diameter of 3 μm can be achieved for the excitation of the microstructures. The luminescence is collected with the same objective such that 90 percent is coupled into the detection beam path at the beam splitter.

If filtering of a specific polarization is required, a rotatable half-wave plate and a linear polarization filter can be inserted in front of the focusing lens and entrance slit of the monochromator. In Setup A a single-stage monochromator (*Acton SP2750* from *Princeton Instruments*) is used, which has a focal length of $f_{mono} = 750$ mm. It is equipped with dispersive optical gratings with 300, 1200 or 1500 lines/mm to spectrally analyze the detected light. In Setup B a double-monochromator composed of two *Acton SP2750* from *Princeton Instruments* is used instead, which include gratings with 300, 600 or 1200 lines/mm and also have a focal length of $f_{mono} = 750$ mm each. Behind the last mirror in the monochromator, the light is directed onto a nitrogen-cooled CCD camera. The distribution of the spectrum on the CCD array has been calibrated using a krypton-lamp, such that a fixed grating position can be associated with a specific wavelength range of the spectrum. The highest spectral resolution achievable with Setup A and B is 27 μeV and 25 μeV , respectively.

Using this basic setup configuration, the emission spectra of microstructures can be evaluated. The QDs investigated in this work show different characteristic emission lines, as explained in Chapter 2.2.1. To distinguish between excitonic and biexcitonic transitions, the filter wheel behind the excitation laser can be used to record scans of the QD emission as a function of the excitation power [Abb09]. Polarization-resolved measurements allow to distinguish charged from neutral excitonic and biexcitonic states, if the latter show a detectable fine-structure splitting.

A flip mirror can be introduced into the beam path to direct the light out of a second monochromator exit port and onto a fiber collimator. The latter couples the collected

light into an optical fiber which can be connected to different measurement configurations that will be described in the following section.

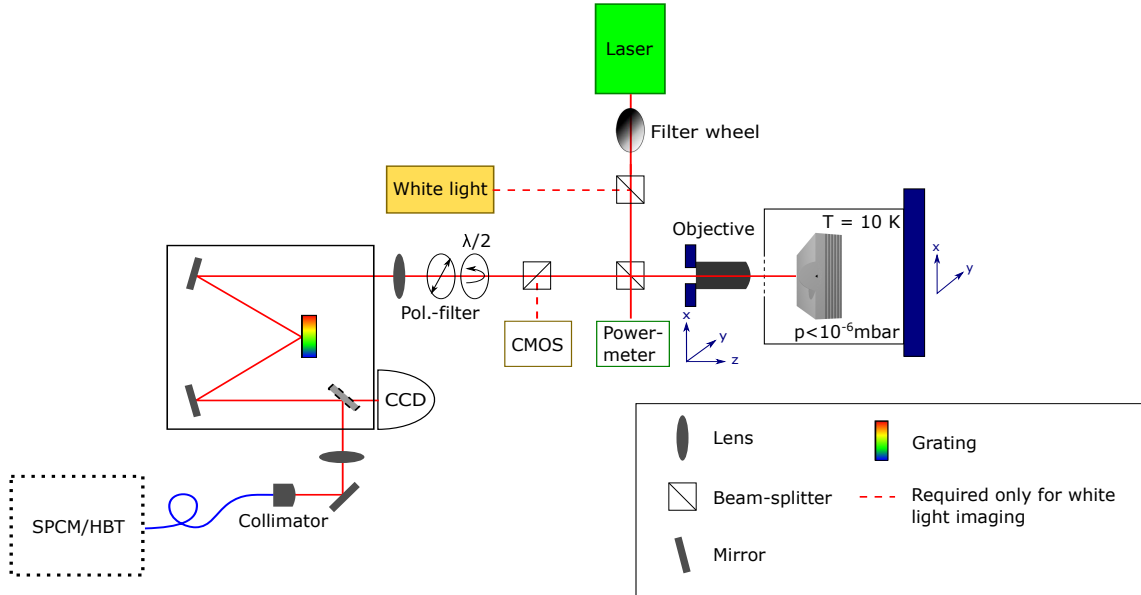


Figure 4.1: Schematic of the setup configuration used for micro-photoluminescence measurements.

4.2 Determining the photon-extraction efficiency

The photon-extraction efficiency (PE) η is a figure of merit that describes how many photons are generated by the device per excitation pulse. A photon is defined as 'generated' if it is emitted by the QD, coupled out of the device and coupled into the first optical element of the measurement setup, which is usually a microobjective with a certain NA. The evaluation of the PE is correspondingly based on the number of photons n_{SPCM} that arrive at a single-photon counting module (SPCM), which is connected to the fiber output of the measurement setup. The SPCM (*SPCM-AQRH* from *Excelitas Technologies Corp.*) is based on a silicon-detector that utilizes an avalanche photo diode (APD) with a timing resolution of 40 ps. To evaluate the efficiency η , the number of detected photons per second n_{SPCM} is set in relation to the excitation frequency f_{Laser} and the efficiency of the setup η_{Setup} .

$$\eta_{\text{NA}=0.4} = \frac{n_{\text{SPCM}}}{f_{\text{Laser}} \cdot \eta_{\text{Setup}}} \quad (4.1)$$

The efficiency of the setup describes the probability that a photon that arrives at the first optical element of the measurement setup finally results in a detection event at the SPCM.

Setup	Grating (lines/mm)	Slit widths (μm)	η_{Setup}
A	1200	50	0.009 ± 0.001
A	1500	100	0.011 ± 0.001
B	1200	50	0.00245 ± 0.00029

Table 4.1: The table gives the setup efficiencies for the three different setup configurations that are used for the measurements described in this thesis. Different gratings can be employed in each setup and the width of the entrance and exit slit of the monochromator can be chosen. The significantly lower efficiency η_{Setup} of Setup B is explained by the fact that it includes a double-monochromator instead of a single-stage monochromator used in Setup A.

This number is found by using the setup in a configuration where the sample is replaced by a gold mirror, which has an approximate reflection of 100 %. A continuous wave laser source is chosen with an emission wavelength that corresponds to the typical QD emission, such that all optics in the setup give the same absorption and scattering effects as with an actual QD sample. To gain a value for η_{Setup} , the applied laser power can be set into relation to the number of counts registered by the SPCM. The full evaluations of the setup efficiency for the two setups are described in the PhD-thesis of Alexander Thoma [Tho17] for Setup A and Alexander Schlehahn [Sch17] for Setup B and result in the values shown in Table 4.1.

It has to be taken into account that both setups are equipped with a microscope objective with a NA of 0.4, such that the efficiency $\eta_{\text{NA}=0.4}$ evaluated here does not correspond to the full amount of the emission that leaves the device into the upper half sphere.

4.3 Time-resolved measurements

To evaluate the emission characteristics of QD-based sources, it is of interest to analyze the decay time τ_{dec} of the transitions, which is one half of the coherence time as defined in Section 2.2.2 for Fourier-limited emission. It can be measured by combining one or two SPCMs with time-correlated single-photon counting (TCSPC) electronics (*PicoHarp300* from *PicoQuant*), which measure the time delay τ between a start- and a stop signal from two different sources. The TCSPC-module features 65536 channels with minimum time-bin width of 4 ps. To determine the decay time of an emitter, a pulsed excitation laser is used that sends a trigger signal to the TCSPC-module for every pulse as a start-signal. The stop-signal is created by the SPCM when the consecutively emitted photon is detected. In that way, a statistic S for the arrival time τ is measured, which follows an exponential decay. To determine the decay time constant, the following function can be

fitted to the data

$$S(\tau) = a \cdot \exp^{-\frac{\tau}{\tau_{dec}}} + b, \quad (4.2)$$

where a is a normalization constant and b an offset accounting for noise and background.

4.4 Photon-autocorrelation measurements

A pure single-photon emission cannot only be characterized by the fact that there is on average one photon per excitation cycle. As explained in Section 2.1, a perfect single-photon source is characterized by a second-order photon autocorrelation at zero time delay $g^{(2)}(\tau = 0) = 0$. As an upper bound, a single-photon source requires the condition of at most $g^{(2)}(\tau = 0) < 0.5$. The photon autocorrelation describes the probability of a second photon to arrive at time $t' = t + \tau$ if a first photon has been detected at time t . A distribution for this value can be experimentally gained using the measurement setup developed by Hanbury-Brown and Twiss [HB56], which is illustrated in Figure 4.2. The photon autocorrelation is determined by using two SPCMs of which one gives the 'start' and one the 'stop' signal to the time correlator. The signal from the sample arrives at the fiber input of the measurement setup, before it is sent to a 1 x 2 fiber-coupler working as a 50:50 beam splitter. To be able to measure also coincidences with negative time delay τ , an additional electrical cable is used to create a delay Δt_{el} in one arm. An optical delay Δt_{opt} is introduced into both fiber paths behind the beam splitter to shift the optical crosstalk of the two SPCMs [Kur01] around 300 ns away from $\tau = 0$. Each arriving photon per se has an equal opportunity of creating a 'start' or a 'stop' signal. If two photons arrive at the beam splitter at the same time, two out of four equally probable cases lead to a coincidence at $\tau = 0$. To gain an estimate of the $g^{(2)}(0)$ value, large statistics of around 10.000 counted events are collected in either continuous wave or pulsed excitation.

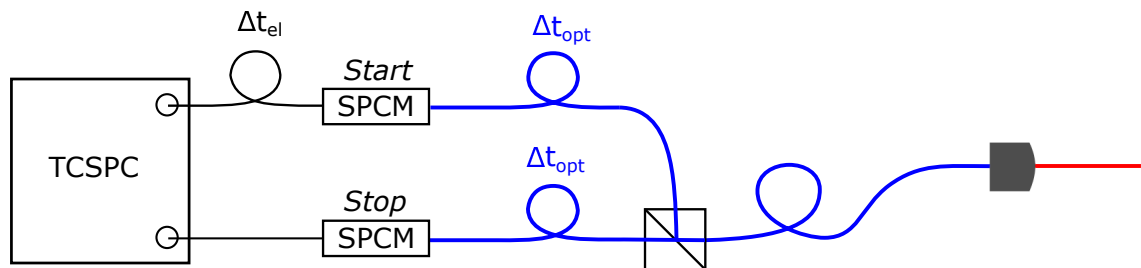


Figure 4.2: Sketch of the setup configuration used for Hanbury-Brown and Twiss-measurements. It can be connected to the basic setup for the characterization of a single-photon sources shown in Figure 4.1.

4.5 Setup for fiber-coupled single-photon sources

Fiber-coupled single-photon sources allow for a plug-and-play usage in future applications, where large free-space setups for the collection of the emission are not practical. To characterize fiber-coupled sources under optical excitation, modifications to the previously described setups are required, as shown in Figure 4.3. The sample is mounted inside the cryostat, but the emission is not coupled out through the cryostat window but collected by an optical fiber directly attached to the sample. To maintain the vacuum conditions inside the chamber, a vacuum-feedthrough is required that connects the fiber inside with another fiber outside the cryostat. The latter is attached to the single side of a 2x1 fiber-coupler. On the other side of the fiber-coupler, the excitation laser can be coupled in through one coupler connection, while the emission of the single-photon source is collected from the second fiber-output. This fiber leads to a collimator which is used to couple the collected emission from the fiber into the beam path leading into the monochromator, that can transfer the diffracted light either to a CCD camera or to a fiber-coupled measurement setup for time-correlated measurements as described above.

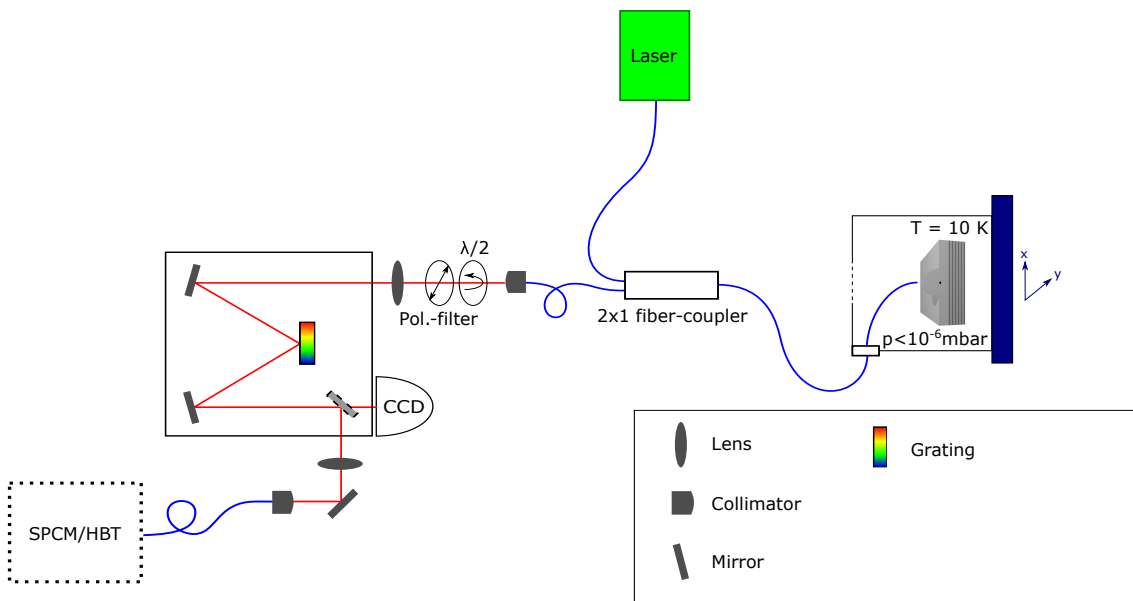


Figure 4.3: Schematic of the setup configuration used to characterize fiber-coupled single-photon sources.

5 Tailoring the outcoupling characteristics of single-photon emitters

Semiconductor QDs have proved to be excellent sources of single-photon emission and can even create entangled photon pairs if a sufficient symmetry of the structure is achieved [Gam96, Ben00, Hub18a]. However, as they are embedded into a matrix material with a refractive index significantly higher than one, a large fraction of the emission is reflected at the semiconductor-air interface.

For the GaAs material system a mature fabrication technology can be used to create structures that increase the amount of harvested light significantly. Basically, 3-D geometries, which reduce the effect of total internal reflection, as well as cavity effects can be exploited to achieve higher PEs. In the following, a finite-element simulation method is introduced, which is then used to optimize the QD microstructures that are investigated in this thesis. The combination of a backside mirror with structured surfaces requires a careful choice of several parameters to achieve the best combination of geometrical optics and cavity effects.

5.1 Simulation concept using a finite-element method

The structures presented in this work are optimized by using the commercially available software package *JCMsuite* by the company *JCMwave*¹. It allows one to solve Maxwell's equations in the frequency domain with the finite-element method (FEM) [Pom07].

To reduce the required computation time, the cylindrically symmetric structures considered here can be described in a two-dimensional plane. A device to be simulated is defined by its geometry divided into domains, and the complex refractive index of the material of each domain. The domains are discretized into a triangular non-uniform mesh following the Constrained Delaunay Algorithm [Che89] to achieve an efficient and precise calculation even for complex geometries. To describe the electromagnetic field, local polynomial ansatz functions are used with adaptable polynomial degree.

¹ <https://www.jcmwave.com>, retrieved on April 29th, 2018

The QD is represented in the calculations by dipole sources. A dipole emitter at position \mathbf{r}_0 is described by a point-like time-harmonic current density

$$\mathbf{J}(\mathbf{r}, t) = \mathbf{j} \cdot \delta(\mathbf{r} - \mathbf{r}_0) e^{-i\omega t} \quad (5.1)$$

with a fixed emission wavelength $\lambda = 2\pi \cdot \frac{c}{\omega}$ and current density vector \mathbf{j} . This is a valid approximation as long as the emitter and the surrounding cavity are in the weak coupling regime. Under this condition it can be shown that a classical description leads to the same results for the spontaneous emission as the calculation using quantum electrodynamics [Nov06].

As the singularity at the emitter position cannot be appropriately treated with the finite-element method, a subtraction approach is applied following Awada et al. [Awa97]. The electromagnetic field \mathbf{E} is described as the sum of a field \mathbf{E}_S , describing the emission of the dipole source in the corresponding bulk material with constant parameters, and a correction field \mathbf{E}_C . Then it is a sufficient approximation to solve Maxwell's equations on the actual geometry for the correction field only and afterwards recombine both fields to $\mathbf{E} = \mathbf{E}_S + \mathbf{E}_C$.

Since the lateral dimensions of the QD are approximately an order of magnitude larger than the vertical, its dipole moment in z-direction and the corresponding emission are omitted. Post processing is finally used to compute the PE into a defined NA from integrals over the calculated fields, or the Purcell enhancement of the emission.

5.2 Backside mirrors and cavities

While semiconductor QDs show excellent single-photon characteristics, their localization inside a semiconductor matrix material with high refractive index results in a significant issue for their use as a single-photon source. The photons are emitted into the matrix material, which in the case of GaAs has a refractive index of $n_{\text{GaAs}} = 3.57$ for a photon energy of $\lambda = 920$ nm at room-temperature [Pal91]. This value can be approximated to $n_{\text{GaAs}}(T = 10 \text{ K}) = 3.48$ at cryogenic temperatures using the temperature coefficient $dn/dT = 3 \cdot 10^{-4} \text{ K}^{-1}$ [Ada93]. To use the emitted photons in a free-beam system they have to be coupled out of the semiconductor into air with $n = 1$ or in the case of a fiber-coupled application to silica glass with $n = 1.45$ [Mal65]. The high difference in the refractive index at the interface leads to a high reflection back into the GaAs, as described by the Fresnel equations. Total internal reflection is observed above angles of $\theta_c^{\text{air}} = 16.7^\circ$ at a GaAs-air interface or $\theta_c^{\text{silica}} = 24.6^\circ$ in the case of silica glass. According to FEM simulation results, only a fraction of $\eta \approx 2.1\%$, and $\eta_s \approx 2.7\%$ respectively, can be coupled out into

the full upper half sphere. For typical numerical apertures of the collection optics of an experimental setup, i.e. $\text{NA}=0.4$, these results decrease even further to $\eta^{NA=0.4} \approx 0.4\%$ and $\eta_s^{NA=0.4} \approx 0.5\%$.

To increase these numbers, a QD can be integrated into a microcavity. This induces several effects for the electromagnetic field, of which some can be explained by classical electrodynamics while others require a description using cavity quantum electrodynamics. We assume that the cavity is limited in z-direction to a height H and is infinitely extended in the other directions. The lower mirror has an almost perfect reflectivity, while the upper mirror only gives a partial reflection as can be observed at a GaAs-air interface. The value $m_c = \text{Int}\left(\frac{2nH}{\lambda}\right)$, which is also referred to as the order of the cavity, describes the number of resonant modes that are fully or partially coupled out of the cavity under an angle $\theta < \theta_c$. For modes with $\theta > \theta_c$ the cavity functions as a waveguide and guided modes can be observed. The reduction of the number of guided modes that the QD can emit increases the amount of light that is coupled out of the structure [Bar02]. Apart from that, the phase relation between the emitter and the zero order cavity mode is relevant for the intensity inside and outside the cavity: If the emission is in phase with the strongest mode propagating in the cavity, its intensity is increased by constructive interference [Ben98]. Consequently, a careful choice of cavity height and emitter position is required to achieve a high amount of emission from the cavity.

Moreover, the coupling between emitter and cavity mode does not only influence the power coupled to the modes but also the absolute rate of spontaneous emission from the emitter. This effect is named after Edward Mills Purcell [Pur46] and expressed by the relation between the spontaneous emission rate in the cavity $1/\tau_{cav}$ compared to the rate in a homogeneous surrounding material $1/\tau_{free}$. Under assumption of spectral resonance between emitter and cavity mode it can be calculated as

$$F_P = \frac{\tau_{free}}{\tau_{cav}} = \frac{3Q(\lambda_c/n)^3}{4\pi^2V} \times \frac{|\mathbf{d} \cdot \mathbf{E}(\mathbf{r}_e)|^2}{|\mathbf{d}|^2}, \quad (5.2)$$

where λ_c denotes the cavity mode, \mathbf{d} the dipole moment of the emitter and $\mathbf{E}(\mathbf{r}_e)$ the electric field at the position of the emitter. The effect is proportional to the quality factor Q of the cavity and antiproportional to its mode volume V . In the simulation results, the Purcell effect can be measured as the absolute emission of the dipole in comparison to the emission in a pure GaAs surrounding at a fixed current density exciting the dipole. Figure 5.1 shows two kinds of planar cavities. In the first case (a), the cavity is formed by a DBR mirror of $\text{Al}_{0.9}\text{Ga}_{0.1}\text{As}/\text{GaAs}$ layer pairs and the GaAs-air interface, while in the second case (b) a gold mirror and the GaAs-air interface create the vertical confinement.

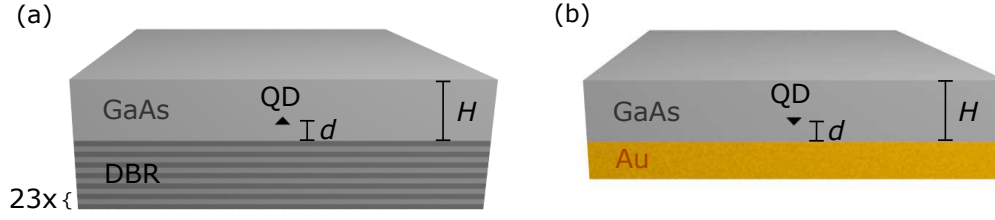


Figure 5.1: Sketch of a QD in a cavity formed by the GaAs and air interface and (a) a DBR mirror with 23 $\text{Al}_{0.9}\text{Ga}_{0.1}\text{As}$ /GaAs layer pairs (b) a gold mirror.

Both mirrors have some minor disadvantages: The reflectivity of a DBR is dependent on wavelength and incidence angle, while the gold mirror can lead to enhanced optical absorption and may develop surface plasmons. Consequently, the performance of both types of backside mirrors in a planar cavity and in combination with microstructures will be investigated in the following.

The optical constants of the gold layer are taken as $n = 0.1195$ and $k = 6.2415$ [McP15], while the refractive index of $\text{Al}_{0.9}\text{Ga}_{0.1}\text{As}$ is set to $n = 2.90$ [Pik80]. To our knowledge, for $\text{Al}_x\text{Ga}_{1-x}\text{As}$ no coefficients expressing the temperature dependence down to cryogenic temperatures are available. The two geometrical parameters that determine the cavity effects are the overall height of the cavity H and the vertical distance between mirror and emitter d . The latter should be chosen such that the emitter is placed at an antinode of the basic cavity mode to achieve an optimized mode overlap and maximum PE. As the reflection at the DBR mirror gives a phase shift of approximately $\pi/2$, a position $d_{\text{DBR}} = \frac{\lambda}{4n} \approx 67$ nm above the DBR mirror fulfills this condition. In the case of the gold mirror, the phase shift is slightly higher than $\pi/2$, which is why the distance should be lower than $d = \lambda/(4n)$. In this work we chose the position to be $d_{\text{gold}} = 60$ nm. A distance above 50 nm should be kept between the QDs and any material interface or surface, to avoid an influence of surface states on the emitter characteristics [Joh10, Wan04].

Figure 5.2 shows the calculated results for the Purcell effect and the PE for a QD in a microcavity at the fixed emitter positions with varying cavity height H . Two different values of the numerical aperture are considered: An NA of 0.4 corresponds to the collection optics of our micro-photoluminescence setups, while an NA of 1.0 describes the collection from the full upper half sphere. It is important for our sample design to consider how much light can be collected in the current state of our measurement optics, but it is also interesting to observe how much emission could be extracted if the collection angle could

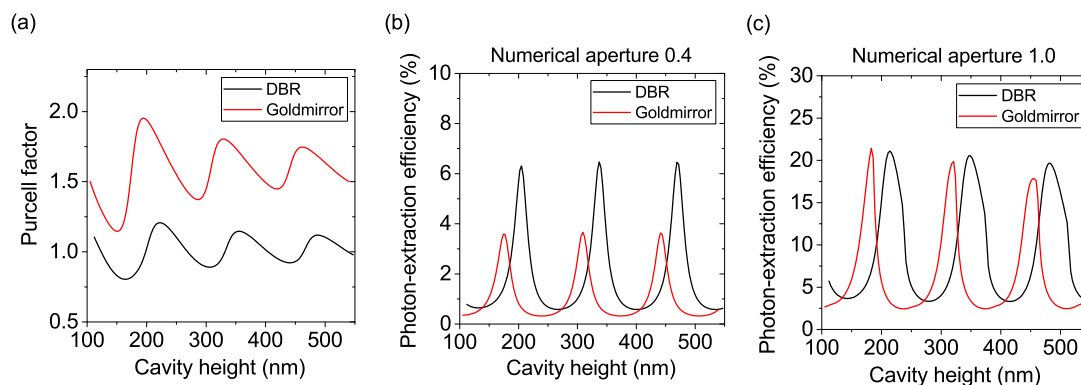


Figure 5.2: FEM simulation results for a dipole inside a cavity formed by a GaAs air interface and a DBR mirror (black) or a gold mirror (red). The QD is situated in 67 nm distance to the DBR mirror and in 60 nm distance to the gold mirror. The overall height of the cavity is varied to observe the influence of the number of cavity modes on the respective quantity: (a) Enhancement of the spontaneous emission of the emitter. (b) Photon-extraction efficiency into a numerical aperture of 0.4. (c) Photon-extraction efficiency into a numerical aperture of 1.0.

be increased towards the full upper half sphere. Maxima of all three performance values can be found wherever the cavity height corresponds approximately to an odd multiple of $\lambda/(4n)$, as this allows for constructive interference of the upward and downward propagating emission. The simulations confirm that the phase shift induced by the gold mirror is slightly larger than $\pi/2$ as the optimum values in this scenario are found at cavity heights around 30 nm lower than the optima for the DBR mirror.

The gold mirror shows a higher Purcell factor than the DBR mirror with values up to 2.0. Both cavity types give a comparable PE into an NA of 1.0, while the one with the DBR shows higher values for an NA of 0.4. This is in correspondence to the fact that the DBR mirror can only reflect light for small incidence angles, such that the decrease by lowering the considered NA from 1.0 to 0.4 is smaller than for the gold mirror. The effect that more light is directed into larger angles in the cavity with the gold mirror does not necessarily make it less attractive for our applications. The higher order modes can be suppressed by microstructuring, as will be explained in the next section. To further increase the efficiency of such nanostructures, two different approaches can be used. The first idea is to increase the cavity effects by the use of an additionally implemented upper mirror [Bar02]. This can significantly enhance the outcoupling as well as the Purcell effect, but also decreases the linewidth of the cavity mode. The resulting narrow-band enhancement of the photon emission makes the integration of randomly grown emitters more challenging and impedes the creation of entangled photon pairs by coupling out the biexciton-exciton cascade of a

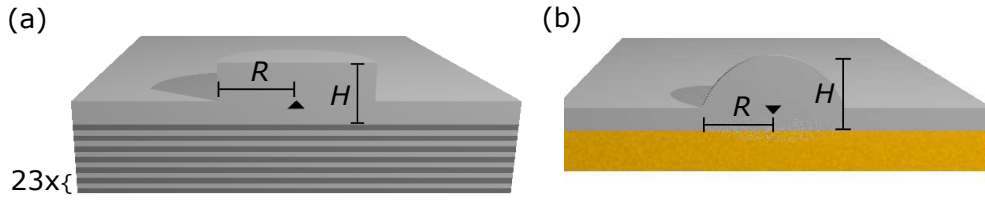


Figure 5.3: Sketch of a QD microstructure formed by (a) a bottom DBR mirror and a micromesa (b) a bottom gold mirror and a hemispherical microlens.

QD. A second approach, which allows one to gain a more broadband enhancement, uses 3-D microstructuring to decrease the mode volume of the cavity and the amount of total internal reflection from the structure. Two different geometries for a broadband increase of the PE will be introduced in the following.

5.3 Micromesas and microlenses

To increase the extraction efficiency of a planar microcavity, microstructuring on the scale of the emission wavelength can be used. In the most simple case, a micromesa is constructed around the emitter such as shown in Figure 5.3 (a). It serves to suppress modes which would otherwise propagate sideways in the planar cavity. In that way, more light is coupled into the lower order modes and guided upwards out of the structure, as can be observed from the example of a simulated light field in Figure 5.4 (b).

In this example with a backside DBR mirror, however, some modes are guided downwards under a large angle to the normal of the DBR structure. This illustrates the advantage of a gold mirror, as it reflects the light independent from the incident angle of the light-wave. Mesa structures can increase the PE significantly, as demonstrated in Figure 5.6 (a). It shows the extraction efficiency of optimized micromesa structures as a function of the numerical aperture of the collection optics for three different kinds of bottom mirror. Apart from the DBR mirror and the gold mirror with 60 nm distance between QD and mirror surface, a version with a distance of $d = 3\lambda/(4n) \approx 200$ nm between QD and gold mirror is investigated. This design will be relevant in the experimental part of this thesis, as a thicker GaAs layer facilitates the fabrication process.

The height H and radius R of the micromesa have been optimized by parameter scans to give the maximum PE into an NA of 0.4. An example of such a scan result is shown in Figure 5.4 (a). The parameter range of the structure height is chosen to approximately

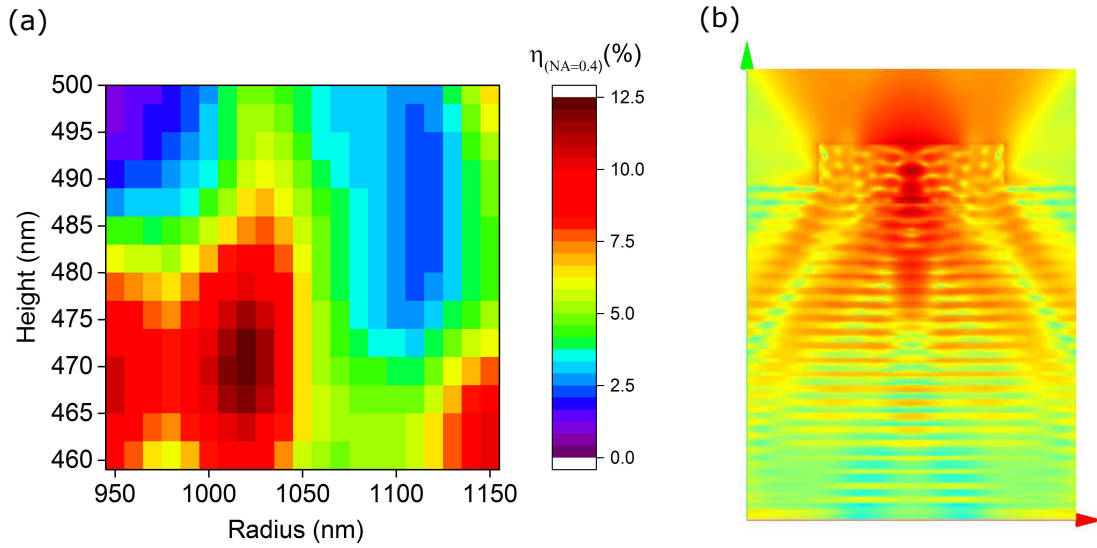


Figure 5.4: Finite-element simulation results for a QD micromesa with backside DBR mirror, where the QD is represented by an electromagnetic dipole. (a) A parameter scan for the height and radius of the micromesa is implemented to find the values that maximize the photon-extraction efficiency into a numerical aperture of 0.4. (b) Electromagnetic field distribution for the micromesa calculated with the optimum parameter values $R = 1020$ nm and $H = 468$ nm.

meet the second-order cavity mode maximum observed for the planar case in Figure 5.2. Exact results for the calculated efficiency $\eta^{\text{NA}=0.4}$ together with the geometric parameters and the corresponding Purcell factor F_P are shown in Table 5.1. For the gold mirror the absorption values are given as well, which are slightly higher for the $d = 60$ nm case. Additionally, Figure 5.6 shows the PE as a function of the NA of the collection optics. The micromesa with small distance to the gold mirror gives the highest value for the PE with $\eta_{(\text{gold}, 60 \text{ nm})}^{\text{NA}=0.4} = 28$ % for an NA of 0.4 and $\eta_{(\text{gold}, 60 \text{ nm})}^{\text{NA}=1.0} = 82$ % for an NA of 1.0. The Purcell factor is smaller than one for this combination, which means that the lifetime of the emitting state will be longer for the emitter in the cavity than compared to the emitter in bulk material. This can become relevant when high emission rates of the device are required either in optical or electrical excitation. As long as the targeted emission rate in triggered excitation is smaller than $\frac{1}{\tau_X}$ with τ_X being the lifetime of the emission, the only factor that determines the extraction rate is the PE η , assuming a quantum efficiency of 1 for the photon emission by the emitter. In that case the DBR mirror is the worst option for the combination with a micromesa structure of the chosen design resulting in $\eta_{\text{DBR}}^{\text{NA}=0.4} = 12$ %. This is, however, still an increase by a factor of 2 as compared to the planar case, cf. Figure 5.2.

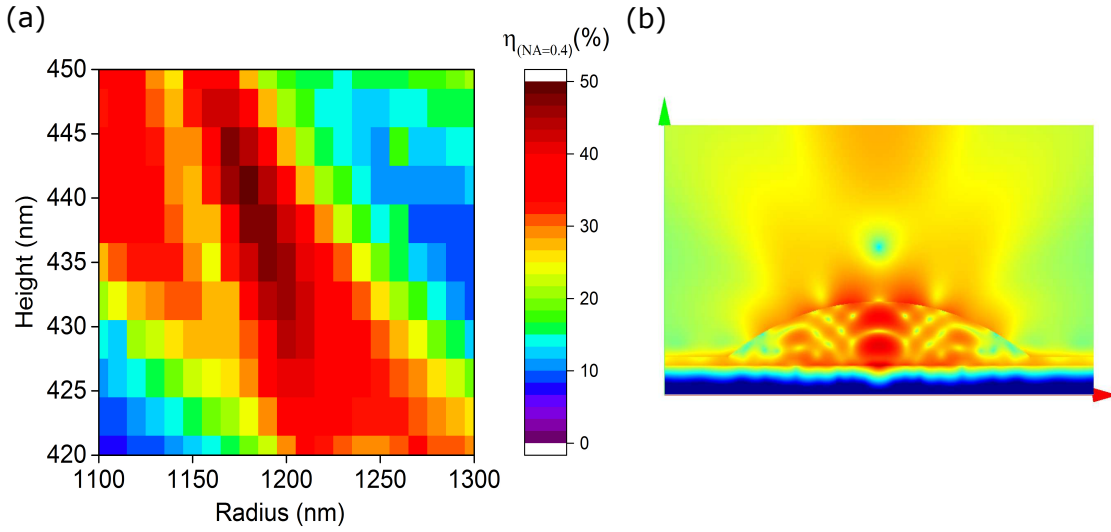


Figure 5.5: Finite-element simulation results for a QD microlens with backside gold mirror, where the QD is represented by an electromagnetic dipole. (a) A parameter scan for the height and radius of the lens is implemented to find the values that maximize the photon-extraction efficiency into a numerical aperture of 0.4. (b) Electromagnetic field distribution for the QD microlens calculated with the optimum parameter values $R = 1090$ nm and $H = 435$ nm.

Cavity effects can be combined with effects created by a change in the geometry of the structure to gain an additional increase in the outcoupling efficiency. A ray-optical perspective can be taken to explain these effects. As mentioned above, the amount of emission from a planar structure or a micromesa is partly limited by the total internal reflection at the GaAs-air interface. By changing the surface from planar to curved, one can decrease the angle between the radiated light and the surface normal. The optimum case for an NA of 1 is given by a half-sphere with the emitter in its center, which results in a zero degree angle between surface normal and light rays [Ma15]. In the scope of this work, a section of a sphere is used with the QD at its bottom. The radius in the plane of the QD is around three times higher than the height above the QD. This is advantageous when measuring with small numerical apertures, e.g. objectives with $NA = 0.4$, as more light is directed upwards than sideways.

A scan of radius and height of the lens is presented in Figure 5.5 (a) showing an optimum with $\eta_{(\text{gold}, 60 \text{ nm})}^{\text{NA}=0.4} = 48 \%$ for the combination of microlens and gold mirror. The corresponding field distribution in Figure 5.5 (b) shows that almost the full emission is directed into the upper half sphere. An absorption of $A = 15.2 \%$, limits the result, but in this case a slight Purcell factor with $F_P = 1.69$ can be combined with a high PE. Table 5.1 also shows the optimum value for a lens structure with $d = 200$ nm with $\eta_{(\text{gold}, 200 \text{ nm})}^{\text{NA}=0.4} = 42 \%$ requiring parameter values $H = 590$ nm and $R = 1130$ nm. A second value with fixed

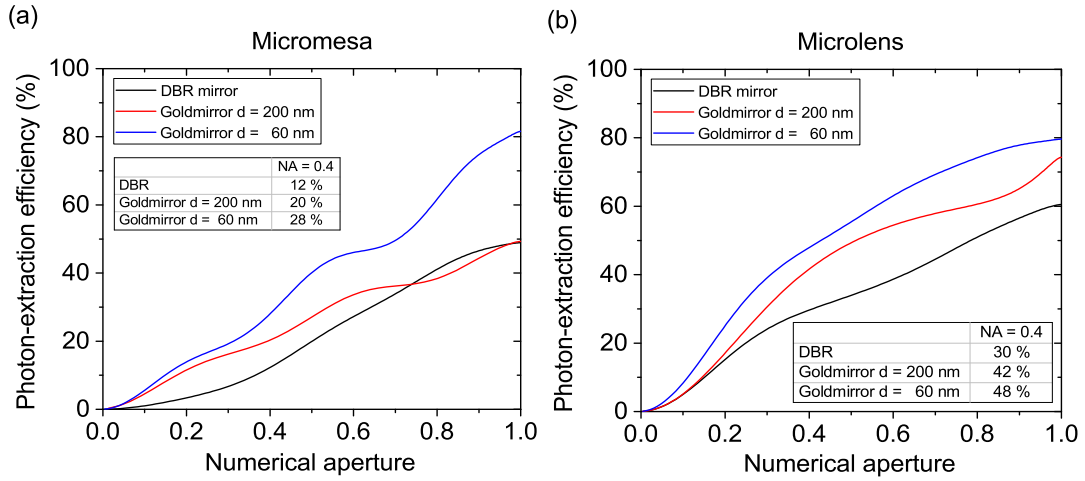


Figure 5.6: Finite-element simulation results for different QD microstructures, where the QD is represented by an electromagnetic dipole. For all lines the optimum parameter values for radius R and height H are chosen such that the photon-extraction efficiency into a numerical aperture of 0.4 is optimized. The graphs show the photon-extraction efficiency as a function of the numerical aperture of the collection optics of (a) micromesa and (b) microlens structures with different bottom mirrors.

structure height $H = 570$ nm is given as this corresponds to the wafer material grown to realize the structures in the experimental part of this thesis.

5.4 Parameter variations

The values for the PE in the last section show the high potential of QD microstructures for the realization of efficient single-photon sources. The parameter scans in Figure 5.4 (a) and Figure 5.5 (a) indicate that these optimum results can only be achieved if all relevant parameters are met with a very high accuracy in the fabrication process.

For all parameters that are determined by the growth process, such as structure height H or position of the QD above the gold mirror d , an accuracy of ± 2 % can be achieved. The radius R of the structures is influenced by the proximity effect during the in-situ EBL process, as well as by the ICP-RIE process, which is never fully anisotropic. This leads to an accuracy of $\Delta R = \pm 50$ nm for the radius of micromesa and -lens. Figure 5.7 (a) shows the influence of a variation in these parameters on the PE of a microlens with backside gold mirror at a distance $d = 60$ nm. It is found that a change in d is less critical, but that variations in R and H on the scale of the fabrication accuracy can induce a decrease in the PE by more than 10 %. Another parameter that needs to be taken into account is the lateral position of the QD inside the microlens. The achievable positioning accuracy

Micromesa					
Design	R (nm)	H (nm)	$\eta^{(\text{NA}=0.4)}$ (%)	F_P	A (%)
DBR	1020	468	12	0.8	0
Gold mirror $d = 200$ nm	911	574	20	1.0	10
Gold mirror $d = 60$ nm	1130	430	28	1.4	12
Microlens					
Design	R (nm)	H (nm)	$\eta^{(\text{NA}=0.4)}$ (%)	F_P	A (%)
DBR	1036	487	30	1.0	0
Gold mirror $d = 200$ nm	1130	590	42	1.1	5
Gold mirror $d = 200$ nm	1264	fixed: 570	28	0.8	6
Gold mirror $d = 60$ nm	1190	435	48	1.7	15

Table 5.1: The table gives results from an optimization of different microstructures using finite-element simulations. The QD is described as an electromagnetic dipole and the design parameters are optimized to gain a maximum photon-extraction efficiency $\eta^{(\text{NA}=0.4)}$ for a numerical aperture of 0.4. Mesa and lens structures are considered for different types of backside mirrors. The optimum values for radius R and height H of the structures are given next to the PE and the Purcell-factor F_P of the respective design. For the gold mirrors, the material absorption A in the gold layer has also been calculated.

of the microstructure to the QD has been determined to $\Delta x_{\text{QD}} = 34$ nm [Gsc15a]. As shown in Figure 5.7 (b), a misalignment on that scale can decrease the optimum value by around 4 %.

The QDs are grown randomly distributed in position and wavelength with an inhomogeneous broadening of $\Delta\lambda_{\text{in}} = \pm 15$ nm. As a consequence, not in every map taken of the sample surface in the in-situ EBL process, a QD which is emitting at exactly the desired wavelength can be found. For that reason, an additional parameter to consider when evaluating the deviations in the fabrication process is the emission wavelength of the QD. Figure 5.7 (c) shows that the increase in PE is very broadband when compared to high-Q emitters such as micropillars [Rei10], but still there is a significant impact if the wavelength is shifted by more than 5 nm. All of these results only give a basic idea of the influence of deviations from the optimum parameter values, as a combination of the effects could either counterbalance losses but also lead to further reductions in the PE.

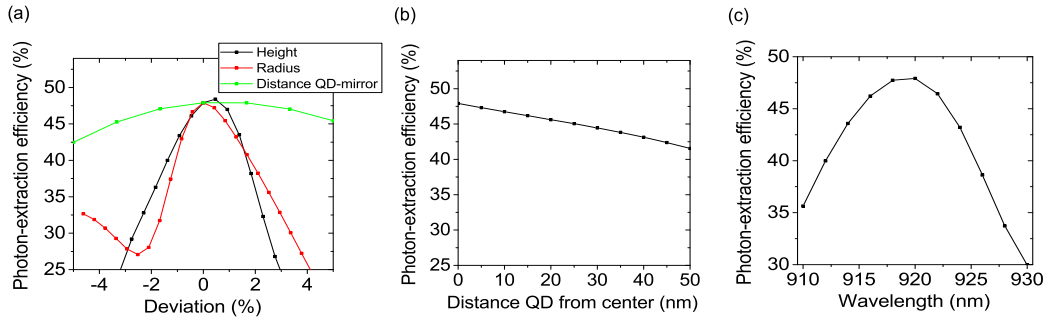


Figure 5.7: Calculated photon-extraction efficiency of a QD microlens with backside gold mirror ($d = 60$ nm) under variation of different parameters: (a) Height H (black) and radius R (red) of the microlens and distance between QD and gold mirror (green). (b) Distance Δx_{QD} of the QD from the center of the microlens. (c) Emission wavelength of the QD.

5.5 Discussion

This chapter numerically analyzes the microstructures that are created and investigated in the experimental part of this thesis. Finite-element simulation results allow us to compare the PEs that are achievable with micromesas and microlenses combined with different types of backside mirrors. The optimum result is found for a combination of a microlens with a backside gold mirror, where the emitter is approximately situated in the first antinode of the electromagnetic field inside the structure. The results show a high dependence of the PE on the numerical aperture of the collection optics. If light could be collected from the full upper half sphere, efficiencies of up to 80 % would be achievable, while for an NA of 0.4 it is possible to reach a PE of $\eta^{\text{NA}=0.4} = 48$ %. However, for applications working with a direct fiber coupling with small NAs of 0.2 or lower, the PE is limited to less than 20 %. For a coupling of the single-photon emission to standard optical fibers this means that the photons should optimally be collected from a large NA and then focused with perfect mode matching into the fiber. Chapter 8.2 will introduce a proof-of-principle implementation of this idea using a microobjective created by 3-D femtosecond direct laser writing.

The variation of some of the simulation parameters shows that the PE is sensitive especially to changes in the height and radius of the microstructure. This is significant for the experimental results, as every processing step is limited in the parameter accuracy that can be achieved. For some parameters, however, intentional variations during the fabrication process can limit this effect. When writing mesas or lenses during the in-situ EBL process the radius can be slightly altered between different structures. During the characterization of the sample the structures with the most accurate parameter values

can be chosen. This decreases the yield of our method, but improves the optimum result achieved with one sample.

Another interesting feature that is omitted in this work is the influence of surface roughness, as it requires computationally demanding 3-D calculations. It was recently found by Schneider et al. [Sch18c] that surface irregularities with a roughness amplitude larger than 10 nanometer can have a significant impact on the optical performance of microlens devices.

In some cases it is advantageous to combine a semiconductor device with on-chip optical elements to collect the emission and direct it into the collection optics. An impressive demonstration was given by Chen et al. [Che18], where a PE of $\eta_{\text{Exp}} = 65 \pm 4 \%$ can be achieved by use of a GaP solid immersion lens. Similarly, in this work a QD microlens is combined with on-chip microoptics, as described in Chapter 8.

6 Experimental implementation of a backside gold mirror for quantum dot microstructures

As demonstrated in the previous chapter, a backside gold mirror in a small distance to a QD microstructure can give a significant increase in the PE as compared to a structure with bottom DBR mirror. Moreover, it can serve as a backside contact in future sample designs for electrical excitation. Previous works already showed that planar cavities can be created by a combination of bottom gold mirror and upper DBR mirror [Tro12a] or that a backside gold mirror can be integrated with photonic nanowires [Cla10]. In this chapter, deterministically written QD micromesas with backside gold mirror are presented including micro-photoluminescence measurement results. The processing method explained here can be regarded as an intermediate step towards the combination of QD microlenses with piezoelectric actuators, which is presented in the next chapter.

6.1 Sample fabrication

The single-photon sources characterized in this chapter are created by combining the flip-chip gold bonding technique with the in-situ EBL method, which are both introduced in Chapter 3. The basic steps are visualized in Figure 6.1.

The initial sample structures are grown using MOCVD such as sketched in Figure 6.1 (a). Appendix B (a) gives the exact layer design, which starts with an $\text{Al}_{0.97}\text{Ga}_{0.03}\text{As}$ etch-stop layer on top of the (001)-GaAs substrate, 370 nm below the InGaAs QD layer. Above the QDs, a layer of either 200 or 60 nm of GaAs is grown, which defines the distance between QDs and gold mirror after the flip-chip process. As explained in the last chapter, these numbers correspond to intensity maxima of the cavity formed by the mirror and the GaAs-air interface of a QD sample after bonding. Pieces of approximately $5\text{ mm} \times 5\text{ mm}$ in size are bonded onto GaAs carrier samples by flip-chip thermocompression gold bonding, as displayed in Figure 6.1 (b). Thin membranes of either 570 nm or 430 nm containing the QDs remain of the sample bonded to the carrier after removal of the GaAs substrate and the etch stop layer. The in-situ EBL process is initiated by spin-coating of the *AR-P 6200* (CSAR 62) resist. The achieved resist layer with a nominal thickness of 90 nm can

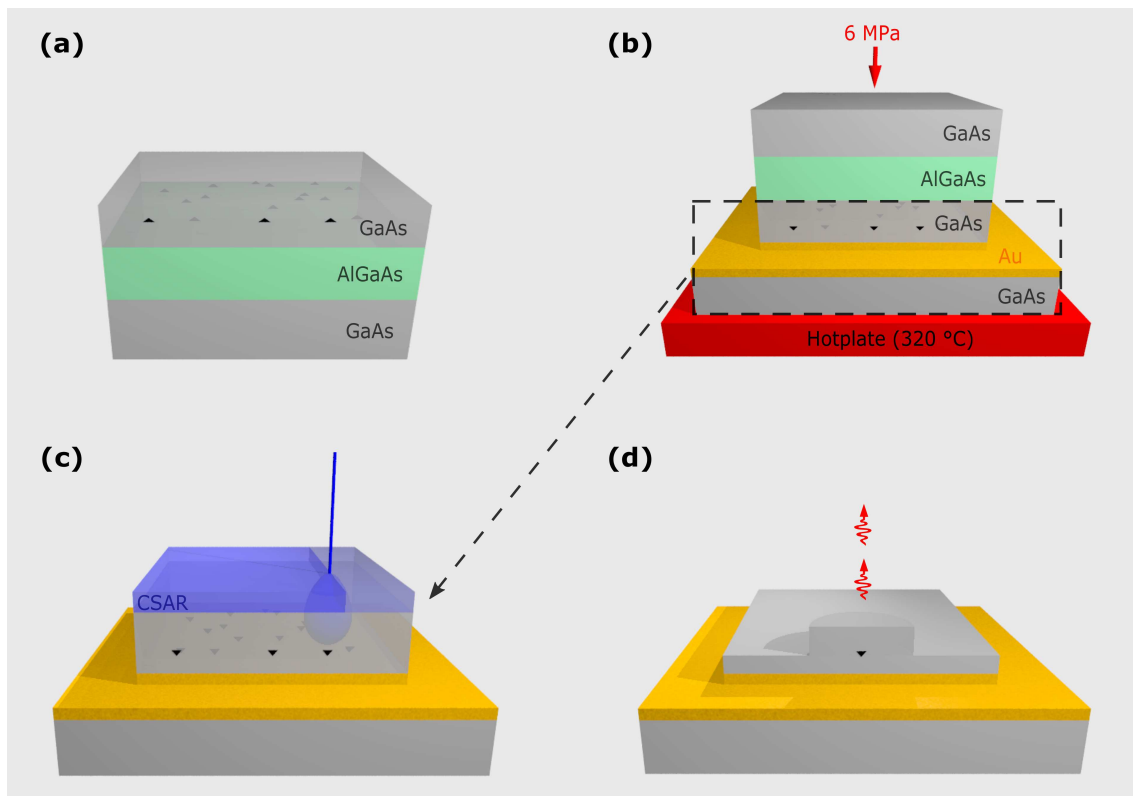


Figure 6.1: Sketch of the fabrication process of a QD micromesa above a backside gold mirror. (a) A layer structure including the InGaAs QDs is grown by MOCVD. (b) 200 nm of gold are evaporated onto the sample, before it is placed upside-down on a gold-coated GaAs carrier for thermocompression bonding. (c) After the GaAs substrate and the AlGaAs etch-stop layer are removed by wet etching, microstructures can be deterministically written on top of the QDs by in-situ EBL. (d) After ICP-RIE etching, the structures are transferred into the GaAs capping layer and serve to increase the single-photon emission from the preselected QDs.

show slight irregularities as the membrane often contains small unevenness or clusters of GaAs remaining from the etch process. Nevertheless, large areas with the desired resist thickness can be found, which can be identified by their homogeneously blue color due to thin-layer interference effects.

In the next step, selected QDs are deterministically integrated into mesa structures by in-situ EBL. As presented in the last chapter, these give a slightly lower PE than QD microlenses. Micromesas, however, promise a higher fabrication yield on bonded samples than 3-D structures, as the latter require an exact knowledge of the resist characteristics for the specific sample. These can vary between different samples due to small variations in the spin-coating process. The exact dose characteristics can be determined for samples

with DBR mirror prior to the in-situ EBL, as they can be spin-coated in large sample sizes and then cut into smaller pieces. A first piece is then used to write electron-dose gradients in a pre-processing step, which serve to determine the 3-D lithography dose area. Bonded samples, however, can not be cleaved into small pieces and have to be spin-coated sample by sample. Thus, for the proof-of-principle approach in this chapter, the microstructures are written with a uniform dose above the estimated threshold dose D_{max} , such that the QDs are integrated into mesa structures.

Two samples are processed and characterized: The first one is registered as NP6587_2_CLL01 (name convention: *wafer name_wafer quarter_sample name*) and will be called Sample A in the following, the second one is NP6632_1_CLL02 and will be referred to as Sample B. The main difference is that Sample A has a distance of 200 nm between QDs and gold mirror, while 60 nm are chosen for Sample B. As explained in the previous chapter, the smaller distance theoretically gives a higher extraction efficiency, yet has a thinner and thus more delicate GaAs membrane after the wet-etching process.

The micromesas on both samples are written by in-situ EBL with a mapping dose of 3 mC/cm^2 and a lithography dose of 10 mC/cm^2 . The radius is varied slightly between 900 and 1100 nm for Sample A and 1000 and 1200 nm for Sample B, as the radius can only be chosen with an accuracy of around $\pm 50 \text{ nm}$ due to the proximity effect during the in-situ EBL. ICP-RIE etching of the samples for 210 s achieves an etch depth of $(370 \pm 10) \text{ nm}$ such that the structures are transferred into the GaAs and the QDs around the mesa structures are removed. Finally, both samples are characterized in the SEM where the diameter of the micromesas can be determined with an accuracy of approximately 10 nm. Both samples have around 3 maps containing micromesas with the required radius for each design, that are characterized by micro-photoluminescence measurements as described in the following.

6.2 Micro-photoluminescence measurement results

To conduct micro-photoluminescence measurements, the samples with backside gold mirror are placed in the cryostat of Setup A, that was introduced in Chapter 4. All of the following measurements are performed at a temperature of $T = 10 \text{ K}$ and a tunable Ti:Sapphire laser is used for the optical excitation of the samples in continuous wave as well as in pulsed emission mode.

Figure 6.2 (a) shows a spectrum of a QD integrated into a micromesa on Sample A. The excitation laser wavelength is chosen as $\lambda_{\text{Laser}} = 870 \text{ nm}$ with an average power of $P_{\text{Laser}} = 11 \text{ }\mu\text{W}$. A bright transition is visible at $\lambda = 926.5 \text{ nm}$ and a less pronounced one

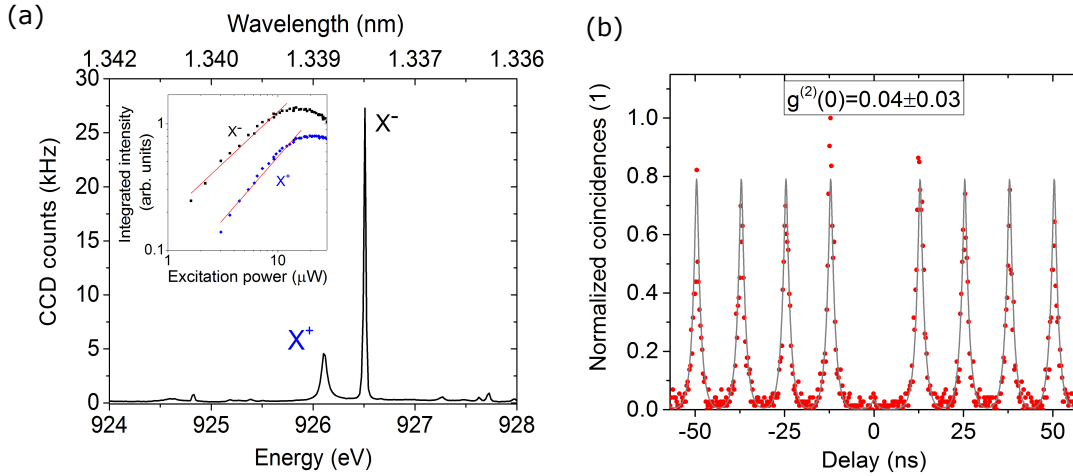


Figure 6.2: (a) Micro-photoluminescence spectrum of a QD integrated into a micromesa with 200 nm distance between QD and gold mirror. Inset: Excitation-power-dependent measurement showing the integrated intensities indicating single excitonic characteristics of the emission lines with linear fits with a slope of $m_X = 0.80 \pm 0.03$ for both lines. (b) Photon autocorrelation measurement of the X^- transition in pulsed quasi-resonant excitation ($f_{\text{Laser}} = 80$ MHz) (red dots). The data is fitted with double exponential decay functions according to Equation 6.2 (grey line) resulting in $g^{(2)}(\tau = 0) = 0.04 \pm 0.03$.

is found at $\lambda = 926.1$ nm. The dependence of the integrated intensity on the excitation power on logarithmic scales shows a slope of $m_X = 0.80 \pm 0.03$ for both lines, which indicates that the emission originates from single excitonic transitions ($m \leq 1$) [Abb09]. The spectral lines do not show any shift in the emission energy in a polarization scan, which is why the bright line is tentatively identified as a negative trion (X^-), while the other transition is assumed to be a positive trion (X^+).

As described in Chapter 4, the PE of the sample can be determined by evaluation of the count rate measured on the SPCMs in pulsed excitation ($f_{\text{Laser}} = 80$ MHz) divided by the setup efficiency and the excitation rate. A count rate of $n_{X^-} = (88.9 \pm 0.9)$ kHz is measured for the negative trion using a monochromator grid with 1500 l/mm and exit and entrance slits of 100 μm . With the corresponding setup efficiency $\eta_{1500 \text{ l/mm}} = 0.011 \pm 0.001$ an extraction efficiency of

$$\eta_{(d=200 \text{ nm})} = \frac{n_{X^-}}{f_{\text{Laser}} \cdot \eta_{1500 \text{ l/mm}}} = (10 \pm 1) \% \quad (6.1)$$

is determined for that emission line.

To demonstrate the single-photon characteristics of the QD emission, photon autocorrelation measurements are implemented for the X^- transition. Quasi-resonant excitation into

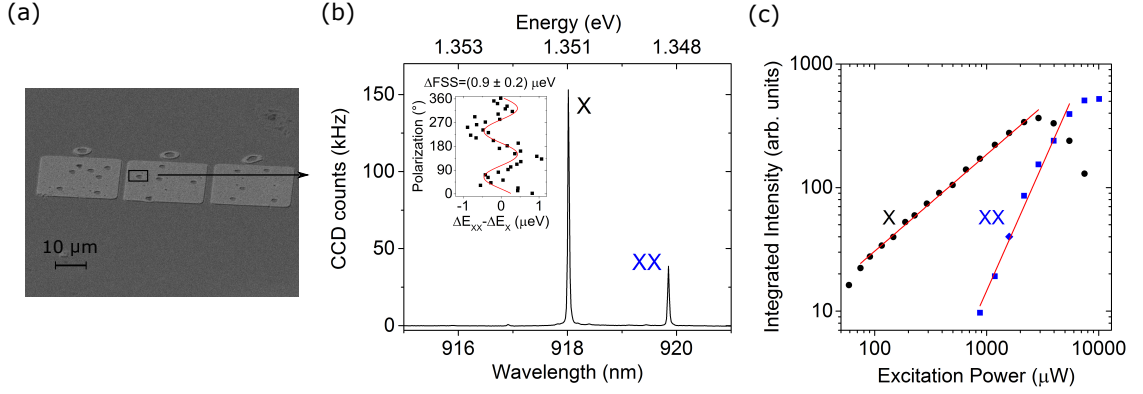


Figure 6.3: (a) SEM images of 3 maps containing QD micromesas. (b) Micro-photoluminescence spectrum of a QD integrated into a mesa structure with 60 nm distance between QD and gold mirror. Inset: Polarization-dependent measurement indicating a non-zero fine-structure splitting. (c) Excitation-power-dependent measurement showing the integrated intensities of the X and XX line on logarithmic scales fitted linearly with a slope of $m_X = 0.78 \pm 0.01$ for the exciton and $m_{XX} = 1.9 \pm 0.1$ for the biexciton.

wetting-layer states is used with a laser wavelength of $\lambda = 907$ nm in saturation of the emission with an excitation power of $P_{\text{Laser}} = 113$ μW. A clear antibunching at $\tau = 0$ is found in the measurement results which are plotted in Figure 6.2 (b). This shows a strong suppression of multi-photon emission events. To gain a figure of merit for this result, the peaks are fitted by two-sided exponential decay functions with a different amplitude at $\tau = 0$ than for the other peaks. The fit can be described by the following function

$$g^{(2)}(\tau) = N \cdot \left(g^{(2)}(0) \cdot e^{-\frac{|\tau|}{\tau_{sp}}} + \sum_{n \neq 0} e^{-\frac{|\tau - n \cdot t_{rep}|}{\tau_{sp}}} \right) * G_A(\tau) \quad (6.2)$$

where N is a normalization constant, $t_{rep} = \frac{1}{f} = 12.5$ ns is the time between two excitation pulses and $G_A(\tau)$ is a Gaussian distribution which describes the timing resolution and system response of the measurement setup. A prerequisite for this description is that $t_{rep} \gg \tau_{sp}$ and that the coincidences around $\tau = 0$ can be described by a single exponential function, which could be hindered e.g. by recapture processes [Aic04, Pet07, Kum16]. In our case the fit (gray trace) gives an estimate of the photon autocorrelation at $\tau = 0$ of $g^{(2)}(0) = 0.04 \pm 0.03$, corresponding to a high suppression of multi-photon emission events.

In the following, a QD integrated into a micromesa on Sample B with 60 nm distance between QD and gold mirror is presented. Figure 6.3 (a) shows SEM images of 3 maps created by the cathodoluminescence measurement step during the in-situ EBL. Several

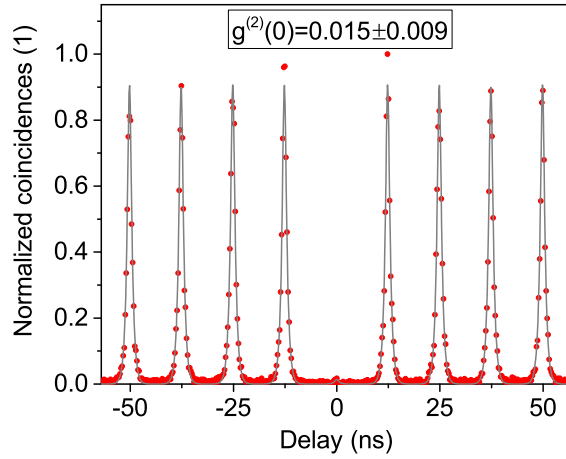


Figure 6.4: Photon-autocorrelation measurements of the excitonic line of a QD micromesa with $d = 60$ nm distance between emitter and backside gold mirror (red dots). The data points are fitted with double-exponential decay functions (grey line) according to Equation 6.2 which yields $g^{(2)}(\tau = 0) = 0.015 \pm 0.009$.

mesa structures were written in each map. For the characterization of this sample, Setup A is used in a monochromator configuration with a grating with 1200 1/mm and an entrance and exit slit of 50 μm . A spectrum of a bright QD integrated into a micromesa is displayed in Figure 6.3 (b). It shows an emission line at $\lambda_X = 918.0$ nm which can be identified as an excitonic transition together with the biexcitonic transition at $\lambda_{XX} = 919.9$ nm. The dependence on the excitation power on logarithmic scales in Figure 6.3 (c) reveals the single excitonic character of the X transition with a slope of $m_X = 0.78 \pm 0.01$ while the XX transition shows a slope of $m_{XX} = 1.9 \pm 0.1$. The fine-structure splitting is determined by the polarization-dependent measurements shown in the inset in Figure 6.3 (b) and is rather small for this structure with $\Delta\text{FSS} = (0.9 \pm 0.2)$ μeV .

For this setup configuration the setup efficiency has been determined to $\eta_{1200\text{ 1/mm}} = 0.009 \pm 0.001$. The measurements in pulsed excitation ($f_{\text{Laser}} = 80$ MHz) in saturation of the X emission line give count rates of $n_X = (132 \pm 4)$ kHz which, following Equation 6.1, results in an extraction efficiency of $\eta_{\text{Exp}}^{(d=60\text{ nm})} = (18 \pm 2)$ %.

Photon autocorrelation measurements are conducted for the single excitonic transition in pulsed wetting layer excitation at $\lambda = 889$ nm with an average power of $P_{\text{Laser}} = 166$ μW , which corresponds to saturation of the transition in this excitation mode. The results are presented in Figure 6.4 and fitted by the function of Equation 6.2 (gray trace). The decay time is determined to be $\tau_{sp} = 0.58 \pm 0.01$ ns and the small dip at $\tau = 0$ results in value for the second-order autocorrelation of $g^{(2)}(0) = 0.015 \pm 0.009$.

6.3 Comparison and discussion

In this chapter two microstructures are introduced containing a QD that is integrated into a combination of a backside gold mirror and a micromesa with optimized geometry. Both samples show clear QD emission spectra and the brightest lines prove excellent single-photon characteristics with $g^{(2)}(0)$ -values below 0.05. The crucial difference between the samples is the distance in which the QD is located to the gold mirror. Finite-element simulations predict an extraction efficiency into a numerical aperture of 0.4 of $\eta_{\text{Sim}}^{(d=200 \text{ nm})} = 20 \%$ for a distance of 200 nm and $\eta_{\text{Sim}}^{(d=60 \text{ nm})} = 28 \%$ for the distance of 60 nm between QD and mirror. The measurement results give lower values with $\eta_{\text{Exp}}^{(d=200 \text{ nm})} = (10 \pm 1) \%$ and $\eta_{\text{Exp}}^{(d=60 \text{ nm})} = (18 \pm 2) \%$. As discussed in Chapter 5.4, the difference between simulation results and measured values is explained by the variance range of the parameters during fabrication, such as the radius and height of the micromesa and the distance between QD and gold mirror. Moreover, the structures are optimized for an emission wavelength of $\lambda_{\text{opt}} = 920 \text{ nm}$, which only approximately corresponds to the available QD emission lines. With that in mind, the extraction efficiencies meet the expectations for micromesas with backside gold mirror. The predicted improvement by the reduction of the distance between QD and gold mirror to 60 nm was correspondingly found in the experimental results.

The successful fabrication of QD micromesas with backside gold mirror shows that the introduced flip-chip thermocompression gold bonding step in combination with in-situ EBL serves for the creation of single-photon sources with high extraction efficiencies. A further increase in the outcoupling is theoretically expected from the implementation of microlenses instead of mesa structures. The presented results are promising for further extensions of the sample design such as the usage of the gold mirror as a backside contact for electrical excitation or, as presented in the next chapter, a bonding of the structures onto piezoelectric actuators for strain tuning of the emission wavelength of the QDs.

7 Wavelength tuning of single-photon sources

Advanced applications of quantum information processing require precisely tunable single-photon sources. To create, for instance, quantum repeater or quantum memories for large networks of sources, an accuracy in the emission wavelength of the emitter on the scale of its linewidth needs to be achieved.

In this chapter, the flip-chip thermocompression gold bonding process is used to fabricate a sample with deterministically written QD microlenses integrated onto a piezoelectric actuator. An advantage of this approach is that, during the processing of the lens structures, QDs with the desired emission wavelength can be pre-selected by their cathodoluminescence signal with an accuracy of 0.3 nm. The strain tuning is consequently applied to achieve a fine-tuning of the emission characteristics.

The beginning of the chapter gives an overview of different tuning methods for semiconductor QDs to explain why a strain tuning mechanism has been chosen for our samples. After a description of the fabrication process, micro-photoluminescence measurements are presented, which demonstrate that a tuning of $\Delta\lambda = 1.7$ nm can be achieved while maintaining high PEs. Second-order autocorrelation measurements demonstrate the single-photon characteristics, which only deteriorate under strong tensile strain. For a more detailed understanding of the tuning effects, the experimental results are compared to calculations using continuum elasticity and the 8-band $k \cdot p$ -method in combination with the configuration interaction method.

7.1 Tuning methods for quantum dot based nanostructures

An optimal tuning method should achieve a high precision in the control of the emission wavelength. At the same time it should not cause any detrimental impact, such as increased charge carrier or phonon effects, and it should leave the sample design as simple as possible. Three frequently used tuning options are temperature, electrical and strain tuning.

7.1.1 Temperature tuning

The band gap $E_g(T)$ of a semiconductor material is affected by its temperature, which can be described by the Varshni equation [Var67]

$$E_g(T) = E_g(0) - \frac{\alpha T^2}{T + \beta}, \quad (7.1)$$

where $E_g(0)$ is the bandgap at $T = 0$ K and α and β are material dependent parameters. Consequently, the energy gap of a QD and its matrix material are affected by temperature changes, which can be used to tune the emission energy of the excitonic states of the QD [Far08]. An increase in temperature, however, increases the interaction of charge carriers with phonons, which leads to a spectral broadening [För03] and as such deteriorates the indistinguishability of the emitted photons [Tho16]. These characteristics are already altered significantly at a temperature above $T = 15 - 20$ K, such that realistically tunings of only few nanometers can be achieved [Rei04].

7.1.2 Electrical tuning

Vertical or lateral electric fields can be applied to the QD device to alter the emission wavelength via the quantum-confined Stark effect (QCSE) [Hel98, Kow05, Kis08]. Next to a tuning in the range of several nanometers, the fine-structure splitting can be reduced by the application of large electric fields, such that in principle entangled photon pairs can be created [Ben10]. A disadvantage of an electrical tuning is that a decrease in the decay rate of the electron-hole pair can be caused by a separation of the charge carriers in response to the electric field [Dis95]. This can even result in charge carriers tunneling out of the QD [Her10b], thereby reducing the quantum efficiency. Moreover, the electrical tuning rules out the option to simultaneously pump the source electrically, which is necessary to create plug-and-play, on-demand single-photon sources.

7.1.3 Strain tuning

As explained in Chapter 2.2, the size and form of a QD as well as the strain conditions at the location of the QD have a significant impact on the position of its energy levels and with that on the emission wavelength of the excitonic states. Consequently, straining the matrix material and the integrated QDs showed to be a reversible tuning mechanism [Sei06, Din10], which gave tuning ranges of up to 20 meV [Tro12a], corresponding to almost 15 nm. The strain transfer is usually implemented by attaching the QD sample onto a piezoelectric actuator. It could already be demonstrated that this method can be

combined with electrically contacted samples [Tro12a, Zha15].

7.2 Strain tuning of quantum dot microlenses by the use of piezoelectric actuators

The tuning of single-photon sources via temperature or electric fields has a strong impact on many emission characteristics apart from their emission wavelength, and with that limits the usable tuning range. A strain transfer to semiconductor QDs already proved to give large tuning ranges, and even served to concurrently eliminate the fine-structure splitting by use of several tuning axes while shifting the emission energy on a range of 7 meV [Tro15b]. It is a promising approach for a combination with QD microlenses, as the gold layer that is required to bond a QD sample onto a piezoelectric actuator can serve as the backside mirror. Moreover, it could form a backside contact in future sample designs for electrical excitation of the emission, similar to the approach used for QD microlenses with backside DBR mirror [Sch16a].

The strain-tunable microlenses are fabricated by a combination of thermocompression gold bonding and in-situ EBL as described in Chapter 6. To our knowledge, this is the first time a strain tuning mechanism is combined with a deterministic processing method for the fabrication of single-photon sources.

7.2.1 Properties of piezoelectric materials

The general characteristics of piezoelectricity have already been introduced in Chapter 2.2.3. Some materials that show a large piezoelectric effect are used for applications such as sensors, the generation of ultrasonic movement or precise motion systems. Polycrystalline ceramics, e.g. based on lead zirconate titanate (PZT), as well as single-crystal materials with an acentric structure of the unit cell, such as lithium niobate (LiNbO_3) or lead magnesium niobate-lead titanate (PMN-PT), belong to that category.

To achieve a strain tuning we use the inverse piezoelectric effect by application of a voltage U along one direction k of the piezoelectric element with thickness D_k , which induces an electric field $F_k = \frac{U}{D_k}$. In the case of small electric field changes, the relation between strain and electric field is assumed to be linear, but is in most cases not isotropic. Therefore, a tensor representation is chosen such that

$$\epsilon_l = \sum_k d_{kl} F_k \quad (7.2)$$

in a reduced matrix formulation with the piezoelectric coefficients d_{kl} , where $l = 1, 2,$ and 3 define the deformations $\epsilon_{11}, \epsilon_{22}$ and ϵ_{33} along the spatial axes, whereas $l = 4, 5,$ and 6 correspond to the shear strains $\epsilon_{23}, \epsilon_{13}$ and ϵ_{12} , respectively. The linear relationship between electrical polarization and displacement is superimposed by elastic, dielectric and thermal properties, and in the case of polycrystalline materials also by microstructural effects [Top14]. Measurable consequences can be a hysteresis loop between applied field and strain, and a logarithmic creep in time.

The creep of piezoelectric materials can be described by the change in strain $\Delta\epsilon$ along an arbitrary axis depending on the time t passed after application of the electric field. The relation follows a logarithmic function [Vie86]

$$\Delta\epsilon = \Delta\epsilon_0 \left(1 + \gamma \log_{10} \left(\frac{t}{\bar{t}} \right) \right) \quad (7.3)$$

where $\Delta\epsilon_0$ is the change in strain in an arbitrary direction one time unit \bar{t} after the electric field was applied. The parameter γ is the creep factor which can vary with the applied electric field and the history of previously applied fields [Jun00].

7.2.2 Characteristics of the piezoelectric actuators

The piezoelectric elements used in this work were acquired from *CTS Advanced Materials*¹. They are based on the material $\text{Pb}(\text{In}_{1/2}\text{Nb}_{1/2})\text{O}_3\text{-Pb}(\text{Mg}_{1/3}\text{Nb}_{2/3})\text{O}_3\text{-PbTiO}_3$ (PIN-PMN-PT), which is a piezoelectric single crystal. Its coercive field with $F_c = 6$ kV/cm is more than two times larger than that of the single crystal PMN-PT material [J.T07], which allows for higher voltages to be applied before the material is depolarized.

The piezoelectric crystals are grown using a modified Bridgman technique [Bri25, J.T07] and cut in (011) direction. They are customized in size to fit our processing capabilities to 10 mm of length and 7 mm of width. The piezoelectric coefficients are specified by the company as $1200 \text{ pC/N} < d_{31} < 1800 \text{ pC/N}$, $d_{33} < 500 \text{ pC/N}$ and $d_{36} < 2500 \text{ pC/N}$. The Curie-Temperature is determined as $140^\circ\text{C} < T_C < 170^\circ\text{C}$. Above this temperature, the crystal is fully or partially depolarized due to changes in the lattice structure, which is also referred to as the ferroelectric phase transition [Kän57, Zha11]. The polarization can be reinstalled by application of an electric field that is higher than two times the coercive field at room temperature.

The characteristics of the piezoelectric actuator at cryogenic temperatures may significantly alter from that at room temperature. It has been shown for PMN-PT down to cryo-

¹ <http://www.hemat.com>

genic temperatures [Her10a] and for PIN-PMN-PT at temperatures down to $T = -150$ °C [Li10, Zha11], that the piezoelectric coefficient significantly decreases at low temperatures. This can be compensated, however, by application of higher electric fields, as the coercive field is shown to increase with decreasing temperature.

7.2.3 Sample fabrication

The sample used for our tuning experiments is named NP6587_3_CLL01. It corresponds to the layer structure shown in Appendix B (a) where 200 nm of GaAs are chosen for the capping layer. 200 nm of gold are evaporated on top before the sample is bonded onto a PIN-PMN-PT crystal. As described in Section 3.3.5, the substrate and the $\text{Al}_{0.97}\text{Ga}_{0.03}\text{As}$ -layer are removed by wet etching, such that a layer of 570 nm including the QDs remains above the gold layers. Finally, in-situ EBL is used to structure microlenses on top of selected QDs, while varying the microlens radius between 1100 and 1300 nm. ICP-RIE etching for 210 s serves to transfer the microlenses 370 nm deep into the GaAs capping layer.

7.2.4 Micro-photoluminescence measurements

The sample is characterized using Setup A at a temperature of $T = 10$ K. The piezoelectric actuator is contacted with a copper wire that is connected to a biaxial cable via a vacuum feedthrough of the cryostat. A high voltage source from the company *Scientific Research Systems* is used, which can be adjusted with an accuracy of $\Delta U = 2$ V on a range between -20 and 20 kV.

A typical spectrum of a tunable QD microlens is shown in Figure 7.1 (a). Power- and polarization dependent measurements (cf. Figure 7.1 (b) and (c)) allow to identify an X^- transition at $\lambda_{X^-} = 916.9$ nm and an excitonic transition at $\lambda_X = 915.9$ nm, where no corresponding biexciton is observable. The lower line at $\lambda_{XX^+\setminus-} = 918.9$ nm shows a quadratic power-dependence but no polarization-dependence, such that it is tentatively identified as an XX^+ or an XX^- line.

The PE of the bright X^- transition is determined in pulsed excitation ($f_{\text{Laser}} = 80$ MHz), resulting in a count rate of $n_{X^-} = (145.2 \pm 1.1)$ kHz using the grating with 1500 lines/mm and entrance and exit slits of 100 μm . This corresponds to an efficiency of $\eta(F = 0) = (17 \pm 2)$ %, where F denotes the electric field that is applied to the piezoelectric actuator. The single-photon emission of our source is verified in pulsed wetting-layer excitation at $\lambda_{\text{Laser}} = 897$ nm. Figure 7.2 (a) shows a time-resolved measurement of the lifetime of the X^- transition, which can be fitted with an exponential decay function to gain a value of $\tau_{\text{dec}} = 0.72 \pm 0.01$ ns. A small decay time corresponds to a good overlap of the

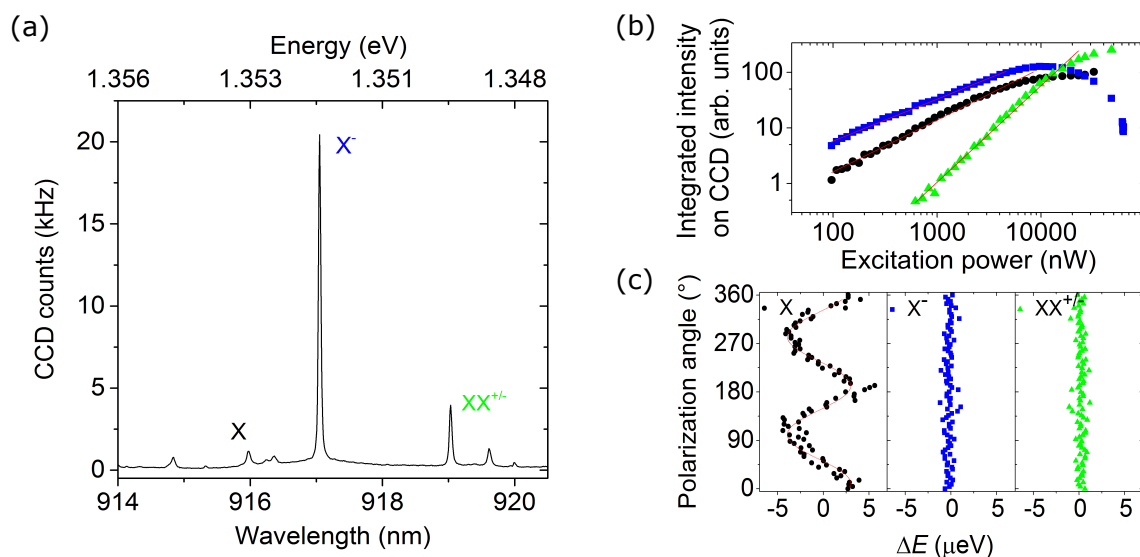


Figure 7.1: (a) Micro-photoluminescence spectrum of a QD microlens bonded onto a piezoelectric actuator. (b) Dependence of the integrated intensity of the three characteristic QD transitions on the excitation power of the laser plotted on logarithmic scales. Linear fits characterize the lines as two excitonic transitions with slope $m_{X^-} = 0.75 \pm 0.01$ and $m_X = 0.93 \pm 0.02$ and one biexcitonic transition with $m_{XX^{+/-}} = 1.74 \pm 0.03$. (c) Polarization-dependent measurement showing the relative changes in emission energy of the three characteristic QD transitions. One of the excitonic transitions shows a characteristic fine-structure splitting of $\Delta\text{FSS} = 7.0 \pm 0.4 \mu\text{eV}$.

electron and hole wavefunction and might also indicate a slight Purcell effect experienced by the QD in the cavity between bottom mirror and GaAs-air interface. In Figure 7.2 (b) the second-order photon autocorrelation measurement is plotted which shows a clear antibunching at $\tau = 0$. Fitting the peaks with two-sided exponential functions as described by Equation 6.2 in Chapter 6.2 leads to an estimate of $g^{(2)}(\tau = 0) = 0.04 \pm 0.02$, which verifies a high suppression of multi-photon emission events. The spontaneous decay time resulting from this fit corresponds very well with the separate lifetime measurement with $\tau_{sp} = 0.71 \pm 0.01 \text{ ns}$.

Tunability of the single-photon emission

To demonstrate the wavelength tuning of the single-photon source, voltages U_P between -600 and +600 V are applied to the piezoelectric actuator as visualized in Figure 7.3 (a). With a thickness of the PIN-PMT-PT of $D_P = 0.03 \text{ cm}$ this corresponds to an applied electric field F between -20 and +20 kV/cm that induces a compressive (+) or tensile (-) strain via the piezoelectric effect. The strain is transferred to the GaAs sample and influences the emission of the X^- line as plotted in Figure 7.3 (b). A slight correction

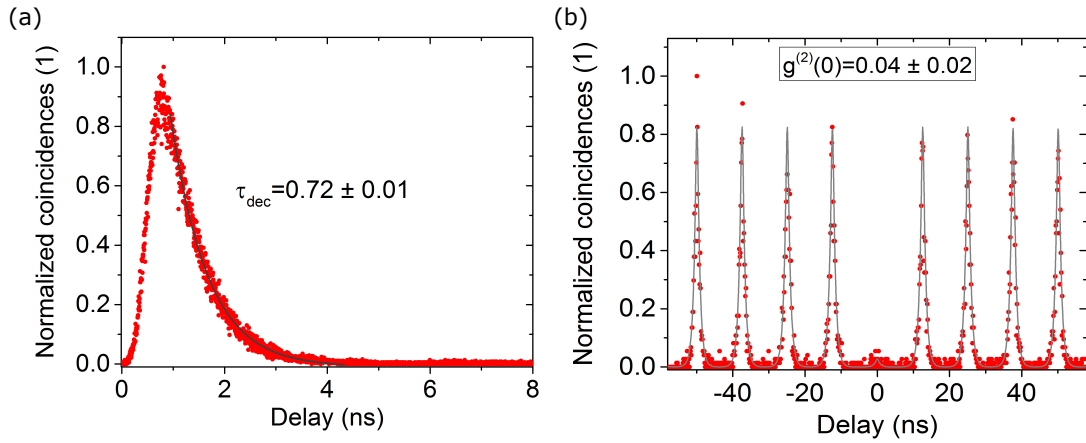


Figure 7.2: Time-resolved measurements of the X^- transition of a QD microlens in pulsed excitation ($f_{\text{Laser}} = 80$ MHz) (a) Lifetime-measurement (red dots) fitted with an exponential decay function (gray line) (b) Second-order photon autocorrelation measurement (red dots) in pulsed excitation ($f_{\text{Laser}} = 80$ MHz) of the X^- line, fitted with double exponential decay functions (gray line) according to Equation 6.2.

of the position of the microscope objective has to be made for every tuning value, as the sample is moved out of the focal spot by the strain of the piezoelectric actuator in lateral as well as vertical direction. A waiting time of 5 minutes is kept after adjustment of the electric field to account for the time dependent creep that is further evaluated in the following. Its impact can last for several hours, but a large fraction of the change in wavelength is observed during the first few minutes. Following that measurement scheme, a tuning range of $\Delta\lambda = 1.7$ nm can be observed.

The intensity measurement in Figure 7.3 (b) also reveals a change in the amplitude of the charged excitonic line in the emission spectrum. We further investigate this effect by measuring the PE as previously described for 21 values of the applied electric field within the full tuning range. The results presented in Figure 7.4 (a) show that the highest efficiency is achieved at a field value $F_{\text{max}} = 12$ kV/cm with $\eta(F = F_{\text{max}}) = (20 \pm 2)$ %. For a strong tensile tuning, the PE decreases down to $\eta(F = F_{\text{min}}) = (6 \pm 1)$ % at the lowest field value $F_{\text{min}} = -20$ kV/cm. Similarly, the results for the second-order photon autocorrelation deteriorate at strong negative field values as shown in Figure 7.4 (b). While $g^{(2)}(\tau = 0)$ stays below 0.05 for all positive and small negative field values, it increases up to $g^{(2)}(\tau = 0, F = -15$ kV/cm) = 0.10 ± 0.03 for a strong tensile strain.

A possible explanation for such changes in the emission characteristics is a separation of the electron and hole wavefunction by the influence of electric fields (QCSE, cf. Section 7.1.2), which could be generated by different effects. The strong electric fields applied to the piezoelectric actuator might influence the QD, which could be ruled out in further

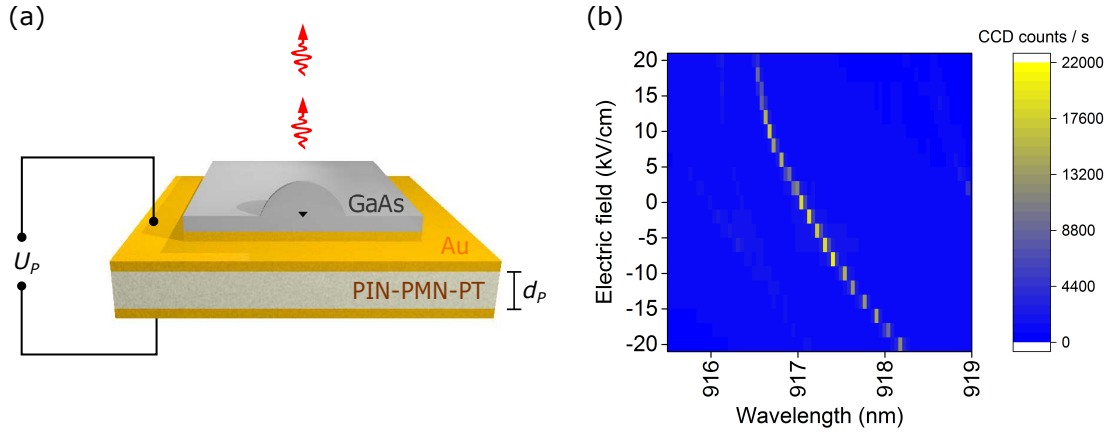


Figure 7.3: (a) Sketch of a tunable QD microlens device. A voltage U_P is applied to the piezoelectric actuator to achieve a strain transfer to the QD microlens. This evokes a tuning of the emission wavelength. (b) Wavelength tuning of the X^- transition by application of an electric field $F_P = \frac{U}{D_P}$ to the piezoelectric actuator.

measurements by changing top and ground contact of the crystal. Another source of field variations can be related to charged states on the surface of the microlens, which create an electric field in the microlens structure that is altered by the strain tuning. If the QD is at a slightly off-centered position inside the lens, it can be influenced by these fields. The lateral accuracy of the positioning of the microstructures by in-situ EBL was determined to 34 nm [Gsc15a], which could be a sufficient deviation from the center of symmetry to see an effect from the changing electric fields. A third possible source of electric fields influencing the electron and hole wavefunctions could result from piezoelectric effects, as the strain transferred from the piezoelectric crystal ([011] poled) is not purely biaxial. It was shown by Aberl et al. [Abe17] that a shear component of the external strain can induce significant first- and second-order piezoelectricity, which influence the size and position of the electron and hole wavefunction and can even shift the sign of the exciton dipole moment.

A deterioration of the emission characteristics under strong tensile strain, however, does not harm the usability of our sources, as our tuning range is much larger than required. The pre-selection of the QDs during the in-situ EBL fabrication step allows us to choose the emission wavelength with an accuracy of $\Delta\lambda = 0.3$ nm such that the tuning can be limited to the range of the optimum emission characteristics.

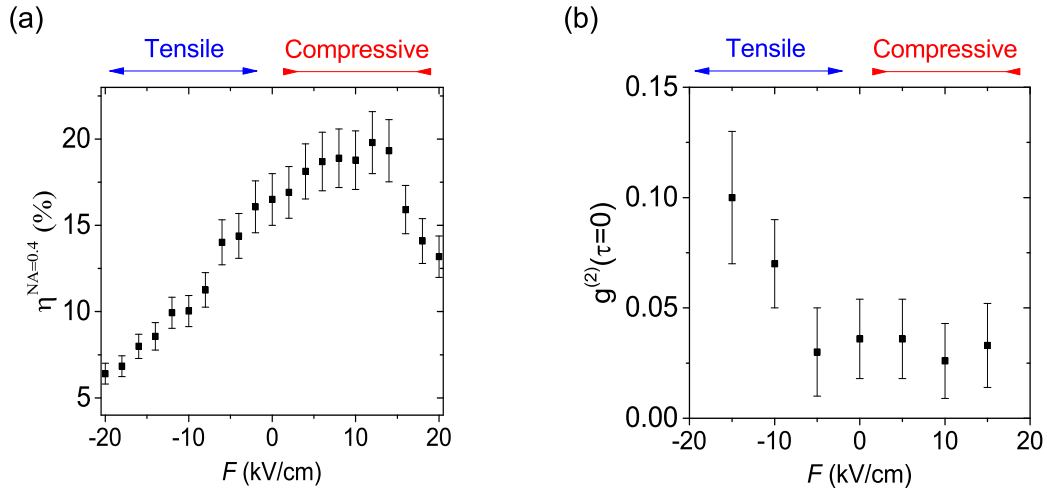


Figure 7.4: Characteristics of the QD microlens depending on the electric field applied to the piezoelectric actuator: (a) Photon-extraction efficiency into a numerical aperture of 0.4. (b) Second-order photon autocorrelation at $\tau = 0$ of the X^- transition. Both quantities are measured in pulsed excitation ($f_{\text{Laser}} = 80$ MHz).

Time-dependent behavior of the tunability

As previously described, piezoelectric crystals often show a time-dependent creep, which should transfer to a time-dependent drift in the tuned emission wavelength. To observe the impact of a creep-behavior on our sample, a time-series of CCD spectra is measured for more than 4 hours after application of a field $F = 12$ kV/cm. The center wavelength of the X^- emission in each spectrum is estimated by fitting the peak with a Lorentzian function. The result is plotted in Figure 7.5 (a). A logarithmic behavior can be observed for approximately the first 30 minutes. A fit according to Equation 7.3 is implemented, giving a creep factor of $\gamma = 1.045 \pm 0004$ at an initial change of $\Delta\epsilon_0 = 0.02$ nm, beginning with the second measurement value after the first 30 seconds. A rather linear curve is observed for the next 2.5 hours, before the wavelength stays constant after around 3 hours. Once a stable state has been achieved, small adjustments in the tuning can be made on a much shorter timescale. Figure 7.5 (b) shows how two positive field changes by $\Delta F = 0.067$ kV/cm followed by a negative change of the same amount are applied, which all stabilize after around 10 minutes and induce a change in the emission wavelength of $\Delta\lambda = (0.004 \pm 0.001)$ nm.

For a usage of the sample as a tunable single-photon source, this means that an approximate value of the required wavelength needs to be set around 3 hours before the start of the experiment, while a fine-tuning can be made at any time on a timescale of 10 minutes.

7.2.5 Comparison to simulation results

To gain a deeper understanding of the tuning effects in a QD microlens, the measurement results are compared with theoretical calculations, which were implemented by Dr. Andrei Schliwa at the Technische Universität Berlin (TU Berlin). The strain distribution in the GaAs microlens is obtained using a continuum elasticity model, as described in Chapter 2.2.3. To represent the strain transfer from the piezoelectric actuator, the lattice constant a_0 of the lowest GaAs layer above the gold mirror is adjusted to $a = a_0 - c \cdot a_0$. The shear component of the piezoelectric actuator is omitted for simplification. We distinguish between hydrostatic strain ϵ_{hy} and biaxial strain ϵ_{biax} , where the latter describes a combination of a compressive lateral and a tensile vertical strain or vice versa. Hydrostatic strain effects are responsible for band-shifts in the QD while (unequal) biaxial changes influence the heavy-hole light-hole splitting [Sch07]. Figures 7.6 (a1) and (b1) show the strain distribution inside a QD microlens without any external influence. The QD and the wetting-layer are permanently subject to compressive as well as tensile effects of hydrostatic and biaxial strain components. An external tuning only adds small relative changes to these values as shown in Figures 7.6 (a2) and (b2), which nevertheless have a measurable impact on the energy states of the QD. Additional strain may affect the energies of the localized electronic states via (i) deformation potentials, thus changing the local band position [Bar50], (ii) the alteration of the quantization energies, and (iii) the change in electron-hole Coulomb interaction. In previous works, (i) showed to be the dominant contribution [Bah90, Sch09b], which is why the other effects are omitted in the following discussion.

The experimentally achieved tuning of $\Delta\lambda = 1.7$ nm can be matched in the simulation by choosing a relative change in the lattice constant by $\tilde{c} = \pm 0.0012$ for compressive (+) and tensile (-) strain. From that we gain a change in the hydrostatic strain component $\Delta\epsilon_{hy}(\tilde{c}) = \epsilon_{hy}(c = \tilde{c}) - \epsilon_{hy}(c = 0) = \pm 0.81 \cdot 10^{-3}$ and a change in the biaxial strain component $\Delta\epsilon_{biax}(\tilde{c}) = \epsilon_{biax}(c = \tilde{c}) - \epsilon_{biax}(c = 0) = \pm 4.65 \cdot 10^{-3}$. An approximation of the impact on the groundstate energy can be gained by the use of deformation potentials. They are linearly interpolated for an $\text{In}_{0.3}\text{Ga}_{0.7}\text{As}$ QD by the literature values for GaAs and InAs to $a_g = -6725.9$ meV for the hydrostatic [Ada05] and $b_v = -1807.2$ meV for the biaxial component [Mad82]. With that the tuning is calculated as

$$\Delta E(\tilde{c}) = a_g \cdot \Delta\epsilon_{hy}(\tilde{c}) - 1/2 \cdot b_v \cdot \Delta\epsilon_{biax}(\tilde{c}) = \pm 1.25 \text{ meV} \quad (7.4)$$

which corresponds to a tuning range of $\Delta\lambda = 1.7$ nm at around $\lambda = 920$ nm. Small variations between the tensile and compressive results of the hydrostatic component are

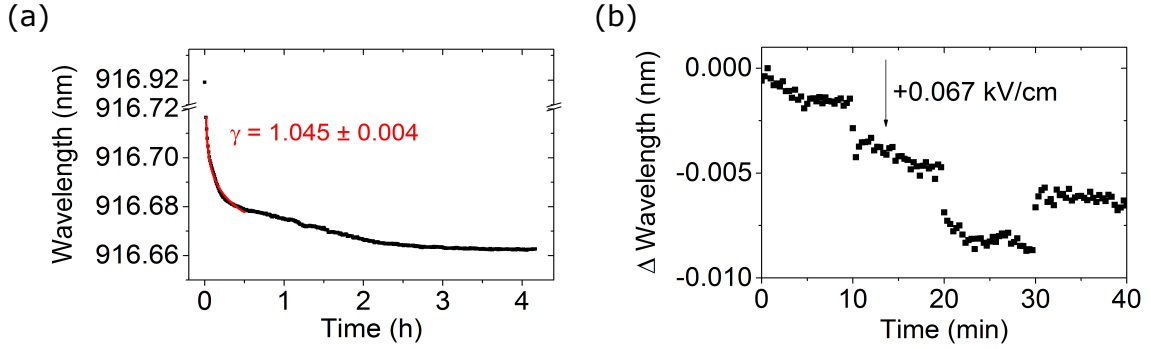


Figure 7.5: (a) Time series of the emission wavelength of the X^- transition after application of the electric field $F = 12$ kV/cm to the piezoelectric actuator. (b) Time-dependent change in the emission energy with small variations in the field applied to the piezoelectric actuator after a first stabilization as shown in (a). Two changes by $\Delta F = +0.067$ kV/cm at $t = 10$ min and $t = 20$ min and one change by $\Delta F = -0.067$ kV/cm at $t = 30$ min can be observed.

omitted here for simplification.

Using the piezoelectric coefficient $d_{31} \approx 1500$ pC/N as published by the manufacturer, the maximum strain that is induced in one lateral direction during the measurement can be estimated to $\epsilon_{\text{Exp}} = d_{31} \cdot F_{\text{max}} = 1500$ pC/N \cdot 20 kV/cm = 0.003. Compared to the theoretical value of $\tilde{\epsilon} = 0.0012$ matching the calculation results with the achieved tuning, it can be roughly estimated that a fraction of $\frac{\tilde{\epsilon}}{\epsilon_{\text{Exp}}} = 40\%$ of the strain effect at the piezoelectric crystal is transferred to the QD sample. This estimation, however, neglects the mentioned temperature dependence of the piezoelectric coefficient. The decrease of this factor at low temperatures indicates a lower actually applied strain, which could

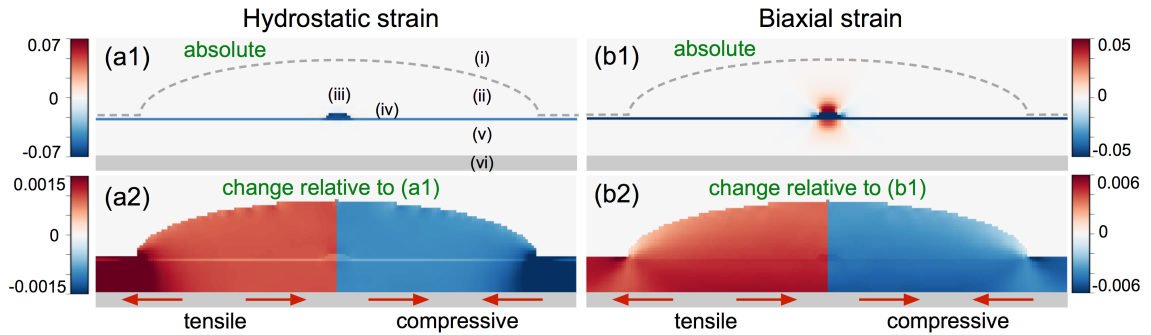


Figure 7.6: Calculated hydrostatic (a1/a2) and biaxial (b1/b2) strain distribution in a QD microlens. The domain is divided into (i) air, (ii) lens, (iii) QD, (iv) wetting layer, (v) spacer layer, and (vi) the piezoelectric actuator. (a1/b1) refer to the situation in absence of external strain, while (a2) and (b2) show the additional effects by external tensile (left) and compressive strain (right).

explain the discrepancy to the result extracted from theoretical calculations.

7.3 Outlook and discussion

In this chapter, a wavelength-tunable QD microlens structure is presented, which is fabricated by a combination of a thermocompression gold bonding method and in-situ EBL. A tuning range of $\Delta\lambda = 1.7$ nm is achieved with a maximum PE of $\eta(F = F_{max}) = (20 \pm 2)$ %. Larger tuning effects have already been demonstrated with semiconductor QDs [Tro12a, Höf17], yet in our case a smaller tuning range is preferable. The QD can be pre-selected in the deterministic processing step such that only a fine-tuning of the emission is required. As every voltage source has a limited accuracy, a smaller tuning range actually increases the preciseness that can be achieved, which in our case is determined to $\Delta\lambda = (0.004 \pm 0.001)$ nm.

To guarantee a long-term stability of the source, a feedback compensation could be applied, which monitors the emission wavelength and adjusts the tuning in a feedback-loop, when required. Previous works have locked the QD emission to atomic resonances with an accuracy of 8 μ eV [Ako11] and 30 MHz in an advanced version with Faraday filtering [Zop18], and achieved accuracies of around 20 MHz with a frequency-locking system [Pre13].

This work gives a first demonstration that QD microlenses can be used as tunable single-photon sources. There are many interesting aspects, however, that can be approached in future experiments. We observed an influence of the tuning on the PE, which is presumably caused by surface charges. This theory can be tested by obtaining a large set of tuning results for different QD microlenses, which should show a different influence of the surface charges due to a more or less centered position of the QD. Moreover, it would be interesting to test QDs of different Indium content, as theoretical calculations predict that this should vary the influence of an external strain on the energy states [Sch09b].

In other works it was shown that by strain tuning the fine-structure splitting of a QD-based single-photon source can be reduced to zero [Tro12b, Tro15b], such that fidelities of almost 98 % can be achieved [Hub18b]. The control of the fine-structure splitting requires separate tuning axes in two directions and a third one to maintain the wavelength-tunability. This could in principle be implemented in combination with QD microlenses, which would result in a bright and deterministically fabricated wavelength-tunable source of entangled photons.

8 Using 3-D printed optical elements for high photon-extraction efficiencies and fiber-coupling

Additive free-form manufacturing by 3-D printing has gained high interest in the last decades. Complex 3-D structures can be created layer by layer from a digital draft. Due to the development of two-photon direct laser writing (see Chapter 3.4), this technique can be transferred to the micro- and nanoscale. It has been used to create various types of optical elements that can be integrated with semiconductor structures, such as metamaterials [Ril08], photonic crystals [Deu04] or waveguides for photonic wire bonds [Bil18]. In this work, we combine QD microlenses with 3-D written multi-lens microobjectives [Gis16b] as well as fiber mounts.

QD microlenses proved to be single-photon sources with excellent optical characteristics. Moreover, the design can be easily extended, e.g. with electrical contacts [Sch16a] or, as demonstrated in the previous chapter, with a tuning mechanism for the emission wavelength. In Chapter 4 it was shown how a high photon-extraction efficiency into the upper half-sphere can theoretically be achieved with a QD microlens. Unfortunately, in most experiments, for instance with a free-beam path or in a fiber-coupling approach, the luminescence is collected only from a limited NA. To decrease the amount of emission lost into large angles, microscale 3-D printed objectives can collect and collimate light almost from the full upper half-sphere.

In a first approach described in the following, the microobjectives are used to collect light from an NA of 0.7 and redirect it into a smaller angle, such that it can be collected with NA-limited free-beam optical experiments. At a further stage, presented in the second part of this chapter, a combination of optics and a fiber mount are created to achieve a direct single-mode fiber-coupling of the emission from a QD microlens. The growth of the samples, the fabrication of the QD microlenses as well as the photoluminescence measurements are implemented at the TU Berlin. All sample pieces are taken from the wafer NP6581, which was grown by Arsenty Kaganskiy according to the layer structure shown in Appendix B (b). The components created by 3-D direct laser writing are fabricated at the University of Stuttgart by Timo Gissibl, Simon Ristok and Ksenia Weber in the group of Prof. Harald Giessen.

8.1 Increasing the photon-extraction efficiency of single-photon sources with 3-D written microobjectives

A high fraction of the emission from a QD microlens is emitted into large solid angles, where it is lost for our free-beam measurement setups, which are equipped with collection optics with an NA of 0.4. On-chip optics, however, can serve to collect and redirect the emission allowing for a significant increase in the amount of photons available for experiments and applications. In this work, a microobjective is written by 3-D direct laser writing on top of a QD microlens, as visualized in Figure 8.1 (a), to increase the achievable PE.

8.1.1 Design and fabrication

The microobjective tested here is designed for the collection of light from an NA of 0.7 and creates a collimated beam shape. The four aspherical surfaces were optimized using the ray-tracing software *Zemax* from the company *Zemax LLC*. All ray-tracing simulations presented in this chapter were implemented by Simon Thiele from the group of Prof. Alois Herkommer at the University of Stuttgart. Due to the large difference in size compared to the microobjective, the QD microlens is approximated to be an isotropic point source in the ray-tracing calculations. In the optimum design of the microobjective shown in Figure 8.2 (a), the upper lens is larger than the lower one with lens diameters of around $120\ \mu\text{m}$ and $78\ \mu\text{m}$, respectively. The parameters for the QD microlens are chosen according to the optimization explained in Chapter 5. Figure 8.2 (b) shows the calculated PE of the QD microlens depending on the NA of the collection optics. For an NA of 0.4, a maximum PE

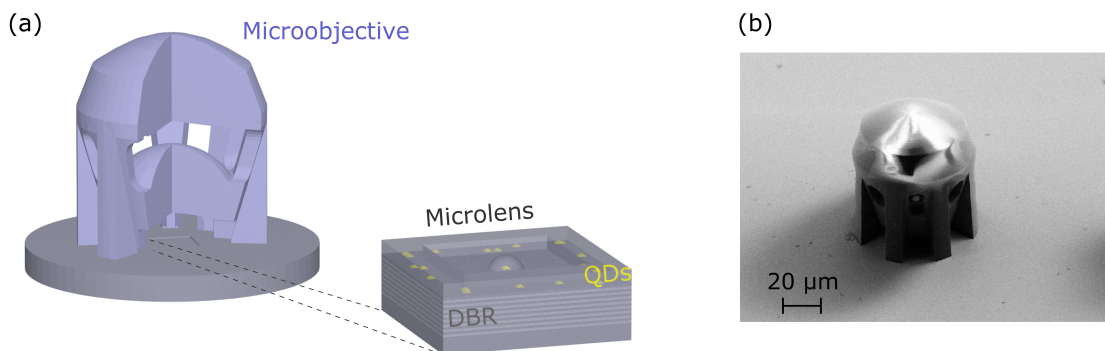


Figure 8.1: (a) Visualization of a double-lens microobjective written onto a QD sample with microlens and bottom DBR mirror. (b) SEM image of a microobjective written on top of a QD microlens.

of $\eta_{\text{Sim}}^{\text{NA}=0.4} = 31\%$ (dashed black lines) is expected. The blue arrow visualizes the effect achieved with the microobjective: It is designed to collect the full emission from an NA of 0.7 and send it into a collimated beam, which should allow for an extraction efficiency of $\eta_{\text{Sim}}^{\text{NA}=0.7} = 41\%$ (dashed blue lines) that can be achieved with the collection optics with an NA of 0.4.

The sample piece used for this experiment is named NP6581_1_CLL07. The layer structure deposited onto this wafer can be found in Appendix B (b). InGaAs QDs are grown above a DBR with 23 $\text{Al}_{0.9}\text{Ga}_{0.1}\text{As}/\text{GaAs}$ mirror pairs and capped with 420 nm of GaAs. Several microlenses are created by in-situ EBL, however only one microlens is written per cathodoluminescence map to avoid stray-light from neighboring lenses to reach the microobjective. Moreover, a sufficient distance of around 300 μm needs to be kept between different maps to leave enough space for the processing of the microobjectives. The sample is pre-characterized at TU Berlin by micro-photoluminescence measurements, then send to the University of Stuttgart for integration of the microobjectives by 3-D femtosecond direct laser writing and returned to TU Berlin for characterization of the full device.

8.1.2 Micro-photoluminescence measurements

All micro-photoluminescence measurements introduced in this chapter are implemented using Setup B at a sample temperature $T = 10\text{ K}$ with an excitation laser emitting at 655 nm. Figure 8.3 (a) displays a spectrum (black trace) of a QD microlens before processing of the microobjective. The excitation power is set to $P_{\text{Laser}} = 19\ \mu\text{W}$ corresponding to saturation of the brightest emission line. The relevant transitions are identified as a neutral exciton X with an emission wavelength of $\lambda_X = 949.2\text{ nm}$, two charged states, X^+ at $\lambda_{X^+} = 947.3\text{ nm}$ and X^- at $\lambda_{X^-} = 950.2\text{ nm}$, and the biexciton XX at $\lambda_{XX} = 950.9\text{ nm}$ by polarization- and excitation-power-dependent measurements. In order to determine the PE of the QD microlens, the emission is directed into the fiber-coupled part of the setup and SPCM counts are acquired in pulsed excitation ($f_{\text{Laser}} = 80\text{ MHz}$) of the three excitonic complexes in saturation of the X transition. We acquire count rates of $n_X = (21.8 \pm 0.2)\text{ kHz}$, $n_{X^+} = (6.4 \pm 0.1)\text{ kHz}$ and $n_{X^-} = (5.6 \pm 0.1)\text{ kHz}$ and sum up the intensities to an overall PE of the QD microlens of $\eta_{\text{Exp}}^{\text{w/o}} = (17 \pm 2)\%$.

The blue trace in Figure 8.3 (a) shows the QD spectrum after combination of the same QD microlens with the microobjective in saturation of the X^+ line. A blue-shift of 0.2 nm is observed for all emission lines. It is probably induced by the altered strain configuration at cryogenic temperatures in the vicinity of the QD. Four posts carrying the lenses of the microobjective have direct contact to the sample surface, as displayed in the SEM image in Figure 8.1 (b). The thermal expansion coefficient of GaAs at room-temperature

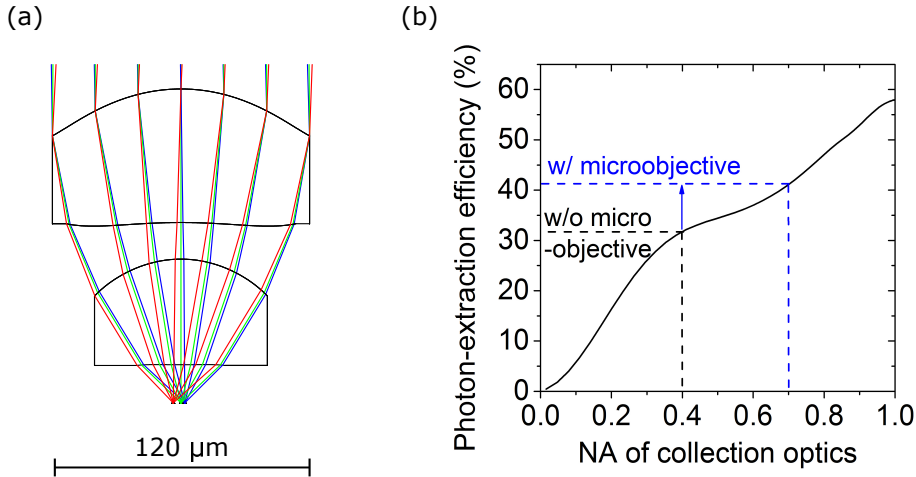


Figure 8.2: (a) Basic design of the microobjective, optimized with the ray-tracing software Zemax. (b) Simulation of the emission from a QD microlens with backside DBR with the software JCMSuite. The microobjective collects the emission from an NA of 0.7 and redirects it into a collimated beam, such that it can be characterized in a setup with an NA of 0.4 of the collection optics.

is $\alpha_{(GaAs)} = 5.7 \cdot 10^{-6} \text{ K}^{-1}$ from where it decreases with decreasing temperature [Som82]. For the exposed photoresist the thermal expansion behavior is difficult to determine and can be larger as well as smaller than this value, as it was shown to be influenced for similar photoresist materials by the exposure dose and method [Qu17]. Consequently, no quantitative estimation of the induced strain can be found with the available material data. The strain effects, however, do not hinder the increase in extraction efficiency gained by application of the microobjective. All excitonic lines exhibit a significant increase in the CCD count rate, where the largest emission intensity and the strongest relative increase of intensity is observed for the X^+ transition. The emission from the X transition is less dominant than before, which indicates a change in excess charge carriers at the QD position.

The PE of the device with microobjective is determined as during the pre-characterization in pulsed excitation by measurement of the SPCM count rates. With $n_X = (25.2 \pm 0.2) \text{ kHz}$, $n_{X^+} = (43.0 \pm 0.4) \text{ kHz}$ and $n_{X^-} = (9.6 \pm 0.1) \text{ kHz}$ an overall sum of the excitonic transitions of the QD gives a PE of $\eta_{\text{Exp}}^w = (40 \pm 4) \%$. This corresponds to an increase by a factor of 2.4 ± 0.4 as compared to the sample before integration of the microobjective and is the highest value so far achieved with a QD microlens. Moreover, it is very well predicted by the result of the simulation of $\eta_{\text{Sim}}^{\text{NA}=0.7} = 41 \%$. As the PE measured without the microobjective ($\eta_{\text{Exp}}^{w\setminus o} = (17 \pm 2) \%$) is significantly lower than the theoretically expected value ($\eta_{\text{Sim}}^{\text{NA}=0.4} = 31 \%$), a higher amount of the emission from the QD microlens

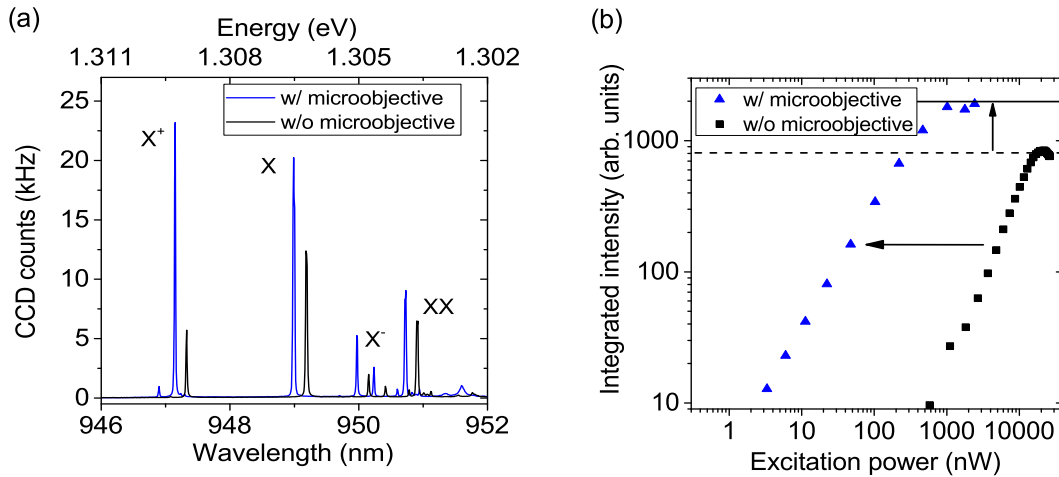


Figure 8.3: (a) Micro-photoluminescence spectra of a QD microlens with (blue) and without a microobjective (black). (b) Integrated intensity (sum of X, X⁺, and X⁻) of a standard QD microlens (black) and the same device with a microobjective (blue) depending on the power of the excitation laser.

is directed into an NA larger than 0.4 than predicted by theoretical calculations. Two other devices on the same sample support this result, as the microobjectives also gave an increase of the PE by a factor of 2.4 and 3.1 at slightly lower overall efficiencies.

Another attractive aspect of the microobjectives is that they induce an additional focusing of the excitation light onto the microlens. Figure 8.3 (b) gives excitation-power-dependent values of the sum of the integrated intensities of all three excitonic emission lines. It indicates a strong decrease of the required pump power for saturation of the emission by more than one magnitude. This is highly beneficial for the implementation of experiments with resonant optical excitation, where it is a challenge to filter the QD luminescence from the scattered excitation light.

Finally, photon-autocorrelation measurements with the fiber-coupled HBT setup are used to demonstrate that the integration of the microobjective has no detrimental impact on the quality of the single-photon emission. A wavelength-tunable Ti:Sapphire laser is used as the pulsed excitation source at a wavelength of $\lambda_{\text{Laser}} = 850$ nm, corresponding to wetting-layer excitation, with a frequency of $f_{\text{Laser}} = 80$ MHz. Measurements with the X⁺ line give the second-order photon autocorrelation results shown in Figure 8.4 at a saturation pump power of $P_{\text{Laser}} = 87$ nW. An almost vanishing dip at $\tau = 0$ demonstrates the strong suppression of multiphoton-emission events. The inset gives a closer look at the correlation results at small delay times. The two small maxima at around one nanosecond delay time indicate recapture processes of additional charge carriers created

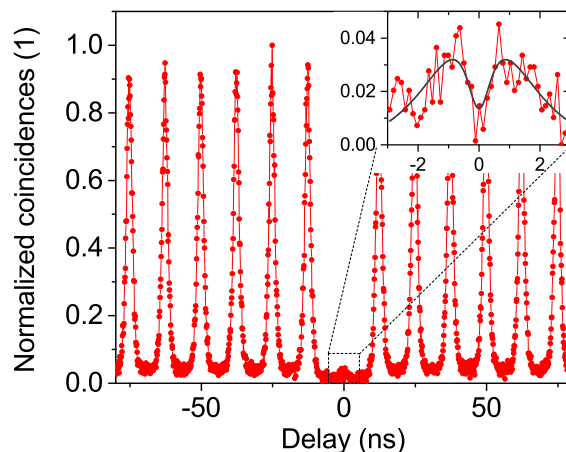


Figure 8.4: Photon-autocorrelation measurement of the X^+ of a QD microlens/microobjective device in saturation under pulsed excitation. The inset shows a zoom-in of the data around $\tau = 0$ (red dots and line) and a fit according to Equation 8.1 (gray line).

by the wetting-layer excitation. They are transferred into the excitonic states and lead to additional emission events before the arrival of the next excitation pulse. This effect cannot be fitted with the previously used Equation 6.2. Similarly to the approach found in Reference [Dal08], the function

$$g^{(2)}(\tau) = \exp\left(\frac{-|\tau|}{\tau_{dec}}\right) - \exp\left(\frac{-|\tau|}{\tau_{cap}}\right), \quad (8.1)$$

was fitted to the results to determine the time constant for the recapture after the first emission $\tau_{cap} = (0.78 \pm 0.05)$ ns and the time until the second decay $\tau_{dec} = (0.85 \pm 0.06)$ ns. To gain a value for the photon-autocorrelation at zero time delay, we integrate the area under the central peak A_0 and divide it by the average area \bar{A} of the peaks at $\tau \neq 0$

$$g^{(2)}(\tau = 0) = \frac{A_0}{\bar{A}} = \frac{0.222}{2.707} = 0.082 \pm 0.002 \quad (8.2)$$

The recapture events could be significantly reduced in resonant excitation of the QD, which would presumably lead to a decrease of this value.

In summary, the microobjectives proved their capability to increase the PE of a single-photon source by alteration of the radiation profile. This can be utilized for advanced approaches with small-NA collection optics, as introduced in the next section.

8.2 Coupling to single-mode fibers with 3-D written objectives and mounting support

As previously described, 3-D-printed microobjectives can serve to collect light from a large NA and redirect it into smaller emission angles. This is especially interesting for applications where a fiber-coupling is required, as optical fibers are restricted in the incidence angle of the light modes that can be coupled into the fiber. Single-mode fibers are usually limited to an NA of 0.1, while standard multimode fibers work with an NA of 0.2 to 0.3. Next to the acceptance angle, other aspects such as the stable connection between a small semiconductor device and an optical fiber as well as the usage under cryogenic temperatures make the direct fiber-coupling of single-photon streams a challenging task. First approaches with QD-based devices were implemented using evanescent coupling from photonic crystal waveguides [Dav17], micro-positioned gluing of the fiber to the sample [Sch18a, Sni18], or positioning of QD-containing microwires onto a fiber tip [Cad16]. Similarly, a nanodiamond containing an N-V center was placed onto the facet of a photonic crystal fiber to collect its single-photon emission [Sch11].

Here, we introduce an approach enabling a direct coupling of the emission from a QD microlens into a single-mode fiber, which is sketched in Figure 8.5 (a). Two microobjectives are written by 3-D femtosecond direct laser writing to optimize the beam shape. A first objective collects and collimates the emission from the microlens such that a second objective positioned on the fiber facet can focus it into the core of the single-mode fiber. The fiber is positioned and glued into a fiber mount, which is structured onto the sample in an additional step by direct laser writing.

8.2.1 Design and fabrication

The single-mode fiber chosen for the fiber-coupling of a QD microlens is of type 780 HP, which is frequently used for near-IR applications. It has a core diameter of 4.4 μm and an NA of 0.13¹. The fiber is cut to a length of around 30 cm and one end is equipped with an FC/PC fiber connector. The open end is supposed to be connected with a sample that originates from the same wafer as the previously described one and is named NP6581_3_CLL05. Microlenses are processed by in-situ EBL with maps containing only one microlens. Afterwards, several microobjectives are written onto the sample. They were designed by ray-tracing calculations to collect all light from the full upper half-sphere by

¹ Information taken from <https://www.thorlabs.com/thorproduct.cfm?partnumber=780HP>, requested on Mai, 12th 2018

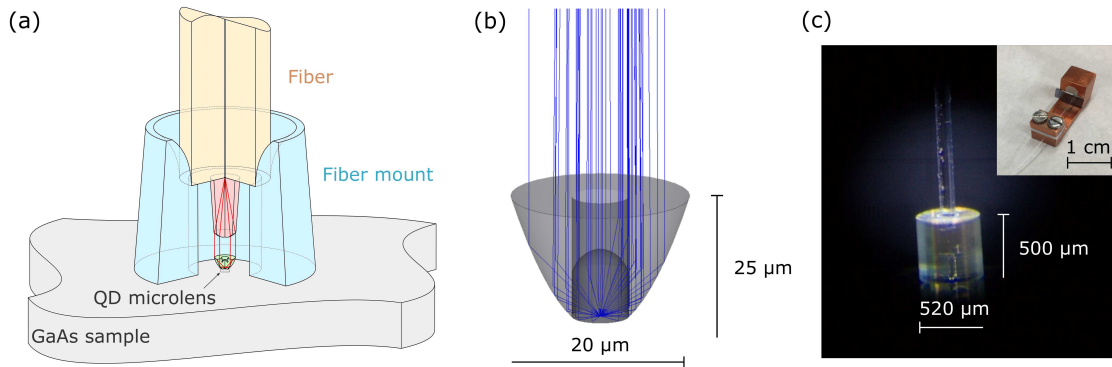


Figure 8.5: (a) Visualization of the fiber-coupling approach based on two objectives and a fiber mount printed by 3-D direct laser writing. (b) Optimized objective that collimates the light from a point source via total internal reflection. (The image was created at the University of Stuttgart by Simon Thiele). (c) Camera image of a fiber that is inserted into a fiber mount written onto a GaAs sample. (The image was taken at the University of Stuttgart in the group of Harald Giessen.) The inset shows the fiber-coupled device placed into a holder that serves to protect the connection between sample and fiber from tension and other forces.

employing total internal reflection (TIR) as shown in Figure 8.5 (b). The microobjective consists of an inner lens collecting the emission under small angles, which is surrounded by an outer cone, that redirects the light emitted under large angles to the sample normal. A pre-characterization by micro-photoluminescence measurements serves to choose a bright device containing QD microlens and TIR microobjective, around which a fiber mount is written in a second direct laser writing step. The mount is a hollow cylinder of $500\ \mu\text{m}$ height, that has an inner radius which is one micrometer larger than the diameter of the fiber end with $126\ \mu\text{m}$. A step with a smaller inner diameter is included to keep the fiber at a distance of $200\ \mu\text{m}$ above the sample surface.

The second type of microobjective is processed directly onto the fiber facet. A clean cleave is created at one end of the single-mode fiber and the fiber cladding is completely removed on a length of $5\ \text{mm}$ from the tip. To locate the fiber core, an optical signal is inserted from the opposite fiber end facet and monitored on a CCD [Gis16a]. Then the fiber objective (FO) is written using a dip-in technique [Büc12]. The elongated spherical lens that is applied serves to collect the collimated emission and focuses it into the fiber core. The design parameters for the fiber objective have been determined to a length of $L_{\text{FO}} = 147\ \mu\text{m}$ and a maximum diameter of $D_{\text{FO}} = 27\ \mu\text{m}$.

After application of the fiber objective, the fiber is inserted and glued into the mount using a microscope setup at the University of Stuttgart. During that process the fiber is fixed with a fiber clamp such that it can be moved using micrometer positioning screws.

The fiber is slowly moved towards and into the fiber mount, as shown in Figure 8.5 (c). Once it has touched the inner base of the mount it is fixed with a drop of glue (*Norland Optical Adhesive 63*).

To be able to securely transport the sample, it is vertically attached with gluing silver inside a copper holder, that is shown in the inset of Figure 8.5 (c). As copper has a high thermal conductivity, it can be used for mounting the sample to any kind of cryostat instead of directly gluing the sample onto a coldfinger. The fiber is carefully clamped between two teflon plates by tightening two screws such that the transfer of tension to the fiber mount is reduced but the fiber is not damaged by the pressure.

8.2.2 Evaluation of the fiber-coupling of a quantum dot microlens

The sample is characterized before and after the application of the TIR-objectives in Setup B under optical excitation at a laser wavelength of $\lambda_{\text{Laser}} = 655$ nm. Three devices are tested, and they all show an increase in their spectral emission when collected from an NA of 0.4. A micro-photoluminescence spectrum of the brightest device is presented in Figure 8.6 (a) at a cryostat temperature of $T = 10$ K (black trace). The spectral lines are identified before fabrication of the microobjective by polarization- and power-dependent measurement results to an X^+ emission at $\lambda_{X^+} = 905.9$ nm, a neutral excitonic transition at $\lambda_X = 910.3$ nm and a biexcitonic transition at $\lambda_{XX} = 909.4$ nm. A comparison of the spectra measured before and after the application of the microobjective (blue trace) shows a wavelength shift of all emission lines by $\Delta\lambda = -3.0$ nm. This is a significantly larger shift than the one found for the microobjectives in the last section. There, however, a strain could only be induced by the posts of the microobjective that are in direct contact to the sample in a distance of several micrometer to the microlens. For the fiber-coupling approach, the microobjective is printed directly onto the microlens, such that a stronger strain transfer to the QD is induced, which is presumably caused by the different thermal expansion characteristics of GaAs and the polymer.

Both spectra are taken in saturation of the X^+ line, where a comparison of the integrated intensities of this transition gives an increase of $\frac{I_{w\lambda}}{I_{w\lambda_0}} = 2.31 \pm 0.03$ by the application of the objective. The PE of the device with objective is determined as the sum of the emission of the exciton and the trion in pulsed non-resonant excitation to $\eta_{\text{Exp}}^{w\lambda} = (16 \pm 1)$ %. The sample is less bright than the one in the first part of this chapter, and the increase of the collected emission by the microobjective is slightly lower although its collection angle is higher. The latter can be explained by the fact that the objective is around five times smaller such that it should be more sensitive to misalignments and inaccuracies in the writing process. The limited dimensions, however, are required to keep the ray diameter

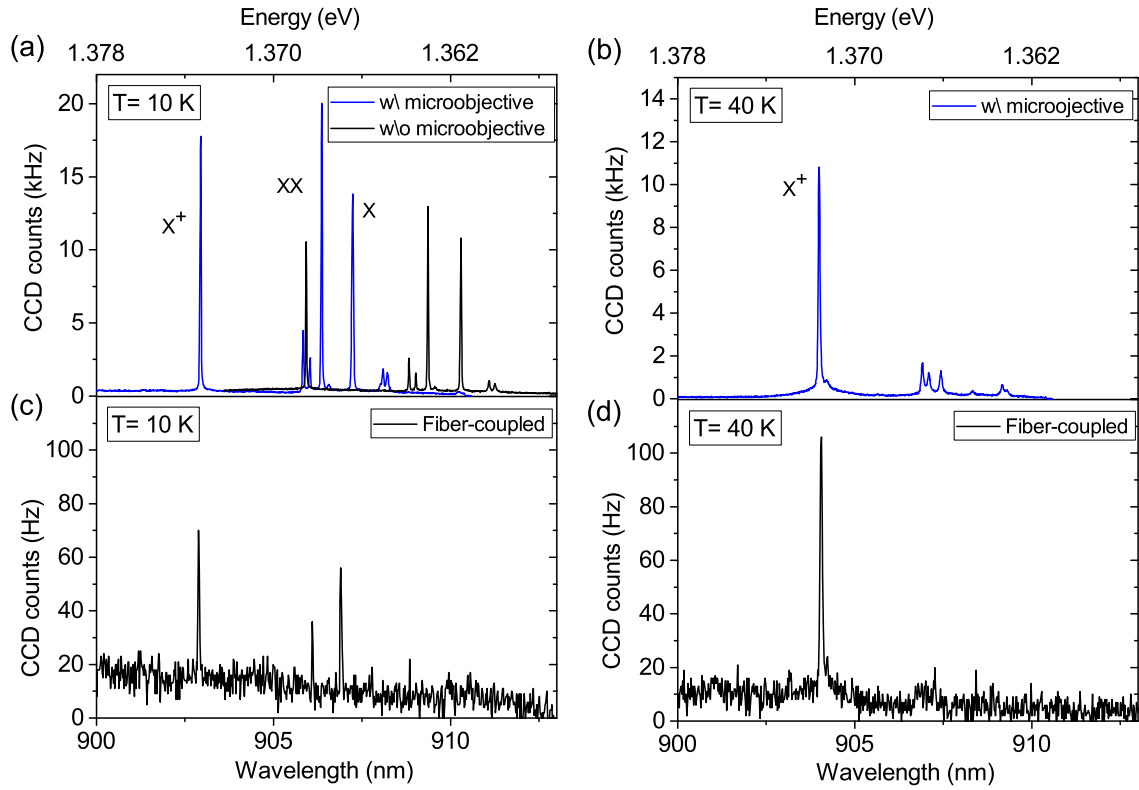


Figure 8.6: Photoluminescence measurements under non-resonant excitation demonstrating the result of the fiber-coupling with a TIR microobjective. (a) Spectrum before (black) and after (blue) application of the TIR microobjective collected by a macroscopic objective with an NA of 0.4 at a temperature of 10 K. (b) Spectrum after application of the TIR microobjective collected by a macroscopic objective with an NA of 0.4 at a temperature of 40 K. (c) Spectrum at a temperature of 10 K collected with a single-mode fiber attached to the sample with a 3-D printed fiber mount. (d) Spectrum at a temperature of 40 K collected with a single-mode fiber attached to the sample with a 3-D printed fiber mount.

small enough such that the emission can be directed into the single-mode fiber by the fiber objective.

Figure 8.6 (b) shows the spectrum after application of the microobjective at a sample temperature of $T = 40$ K, where the X^+ transition is much more pronounced than the other emission lines and is slightly red-shifted to $\lambda_{X^+} = 904.0$ nm. The results at this elevated temperature can be of interest if the sample is supposed to be cooled by a Stirling cooler instead of a liquid-helium flow cycle. The Stirling cooler, e.g. *Sunpower CryoTel GT AVC*, allows to create a stand-alone single-photon source that does not depend on any external sources apart from a power supply [Sch15b, Sch18a].

After processing of the fiber mount and objective as well as fixation of the fiber at the University of Stuttgart, the sample is transported back to TU Berlin inside the copper

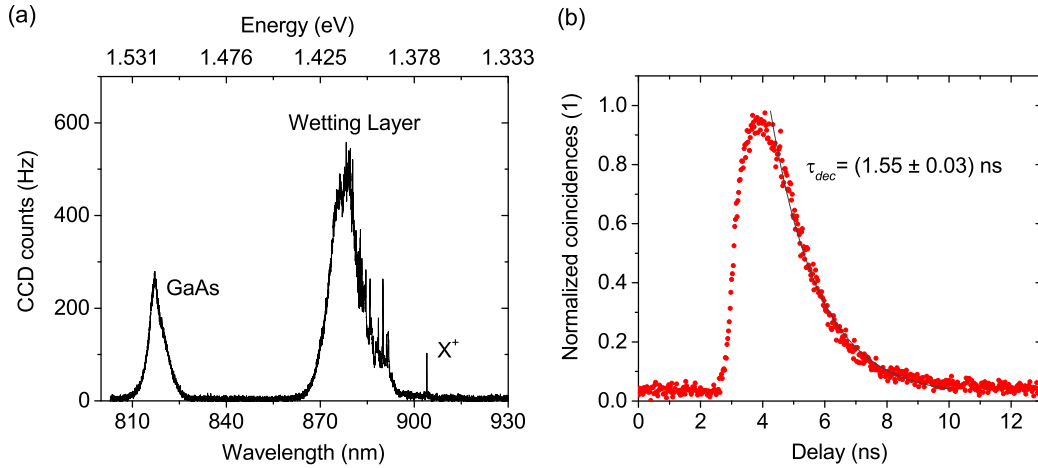


Figure 8.7: (a) Wavelength scan of the emission from a fiber-coupled QD microlens at $T = 40$ K. (b) Time-resolved measurement of the emission from the fiber-coupled QD microlens in pulsed excitation. An exponential fit (gray) of the triggered signal detected by the time-correlated single-photon counting modules (red dots) allows us to determine the decay time constant of the device.

sample holder. The holder can be glued onto the coldfinger inside the cryostat of Setup B and the fiber is guided out of the cryostat by a feed-through designed for this type of fiber. It is connected to the setup configuration for fiber-coupled samples that is introduced in Chapter 4.5. At $T = 10$ K as well as at $T = 40$ K we can find the characteristic lines of the QD spectra as shown in Figure 8.6 (c) and (d). This confirms that the positioning of the fiber mount around the QD microlens and the insertion of the fiber have been successful. The intensity, however, is reduced to less than one percent of the values achieved in the pre-characterization. Figure 8.7 (a) shows a spectrum from the fiber-coupled source which covers a larger spectral range taken by a monochromator scan at $T = 40$ K. It is interesting to see, that the CCD count rates of the GaAs emission and the wetting layer are only around three times and five times higher than the QD emission line, which can be assumed as a normal relation between these spectral features for a QD microlens. This indicates that the lateral placement of the fiber is very accurate, while the loss in efficiency might be caused by the performance of the combination of the two objectives. Either the collimating effect of the TIR objective is insufficient or the objective on the fiber does not focus the emission into the fiber core.

Unfortunately, the achieved count rates are too low to implement photon autocorrelation measurements, but time-resolved measurements of the X^+ transition can be gained. Figure 8.7 (b) shows the result obtained by the TCSPC modules in pulsed excitation. The exponential decay can be fitted following Equation 4.2 to gain an estimate for the decay

constant with $\tau_{dec,X^+} = (1.55 \pm 0.03)$ ns. As this value is in the usual range for a QD at $T = 40$ K, it supports the assumption that the QD has not been severely influenced by the direct laser writing process and that further improvements of the coupling-efficiency will allow for the fabrication of a bright and fiber-coupled single-photon source.

8.3 Discussion

This chapter demonstrates that the combination of QD microlenses with components created by 3-D femtosecond direct laser writing allows for significant improvements in the PE to $\eta_{Exp} = (40 \pm 4)$ %. The emission is collected from an NA of 0.7 by the microobjective and directed into a smaller angle, such that it can be measured using collection optics with an NA of 0.4. Further improvements in the design should allow to collect the emission from the full upper half-sphere. With such a structure, values of the PE of up to $\eta = 80$ % should be possible, if the microobjectives were applied onto a QD microlens with backside gold mirror as presented in Chapter 5.

Components created by direct laser writing can also be used to create fiber-coupled single-photon sources, as demonstrated in the second part of this chapter. A crucial advantage of this approach is that optical components and connector elements can be directly processed onto the sample as well as the fiber facet. The fiber is placed above the sample with such a high vertical accuracy, that additional microscale optical components can be positioned in between. The microobjectives presented in this work did not result in a high coupling efficiency into the fiber, but could demonstrate a high lateral precision of the fiber positioning. A different approach that could increase the coupling efficiency would be to work with only one microobjective that directly focuses the collected light into the fiber. This method would require positioning the fiber in the focal spot of the microobjective, which can be easily realized with the spacer ring inside the fiber mount. Once a more efficient coupling method has been implemented, the combination of QD microlenses with components created by 3-D direct laser writing will lead to a deterministic, reproducible and robust technique for the creation of fiber-coupled single-photon sources.

9 Summary and outlook

In the last decade, first implementations of long-distance quantum communication [Res05, Rau14] proved its potential as a successor of previous cryptography methods. QKD systems with high data rates and a long transmission distance, however, need efficient sources that can be used with quantum repeater concepts. To realize entanglement swapping, a precise tunability of the devices and a high photon indistinguishability is required. Although there is a rapid development in the field of single-photon sources, there is no device so far which could fulfill all requirements of advanced schemes of quantum information technology in one plug-and-play single-photon source. QD microlenses are a promising structure to approach that aim, as they are deterministically fabricated and give a broad-band increase in the extraction efficiency. Moreover, they proved to give excellent values of the second-order photon autocorrelation and a high level of indistinguishability.

This work has gained important results for the creation of a tunable plug-and-play single-photon source based on QD microlenses. The potential of different designs has been explored by the use of calculations of the emitted light fields in finite-element simulations. A thermocompression gold-bonding method was developed and for the first time combined with in-situ EBL to create deterministic QD microstructures with a backside gold mirror. A tunability has been achieved by bonding a sample onto a piezoelectric actuator and microobjectives created by femtosecond direct laser writing were used to increase the brightness of the sources. Moreover, an approach for a robust fiber-coupling of the emission from QD microlenses has been shown, which uses on-chip components fabricated by direct laser writing.

QD microlenses give a significantly increased PE as compared to bulk structures without restricting the light field to a high-Q cavity mode with small bandwidth. The highest PE previously achieved with QD microlenses was limited to $\eta_{\text{Exp}}^{\text{NA}=0.4} = (29 \pm 3) \%$ [Sch15a]. Finite-element simulations were used in this work to show that the combination of QD microlenses with a backside gold mirror has the potential to achieve a PE of above 45 % into an NA of 0.4. By calculation of the impact of varying design parameters, it has been demonstrated that a high accuracy in every processing step is required to achieve these optimum values. An additional option to increase the realized efficiency of the sources is

the collection of the emission from a higher NA. Theoretically, results of $\eta_{\text{Sim}}^{\text{NA}=1.0} > 80\%$ could be achieved for a sample with backside gold mirror by collection from the full upper half sphere.

In the experimental part of this thesis, the combination of a backside gold mirror created by thermocompression gold bonding with deterministic QD microstructures was successfully demonstrated. The introduced devices did not give the theoretically expected PE of more than 40% due to production tolerances of several design parameters. Nevertheless, an expected increase of the PE due to a decrease of the distance between QD and gold mirror from the first order optimum at 200 nm to the zero order optimum at 60 nm could be experimentally found as predicted by the calculation results. Moreover, the combination of a backside gold layer with QD microlenses gives further advantages: The gold layer can serve as a backside contact in future designs for an electrical excitation of the emission, and it proved to be a suitable contact layer for the implementation of a strain tuning. To achieve this, a sample with QD microlenses was integrated onto a piezoelectric actuator of the single-crystal material PIN-PMN-PT.

By the strain transfer to the GaAs sample, a tuning range of $\Delta\lambda = 1.7$ nm of an emission line from a QD microlens was realized. This is sufficient to gain a high flexibility in the choice of the emission wavelength of the single-photon sources, as the QDs integrated into our devices can be pre-selected by their cathodoluminescence signal during the deterministic processing of the microstructures. The tunable lenses showed photon auto-correlation values of $g^{(2)}(0) < 0.05$ and an influence of the imposed strain on the PE with a maximum value of $\eta_{\text{Exp}}^{\text{NA}=0.4} = (20 \pm 2)\%$. In a further step, the indistinguishability of the emitted photons should be confirmed before the sources can be used for experiments such as a Hong-Ou-Mandel measurement with two remote sources [Rei17]. The ability to tune the sources is essential here, as the emitters need to be brought to coinciding wavelengths with an accuracy on the scale of their homogeneous emission linewidth.

Furthermore, by application of femtosecond two-photon direct laser writing, the angle of collection of the single-photon emission from QD microlenses was increased without changing the external setup configuration. Microobjectives were precisely placed above the microstructures to collect and redirect the emission from a larger NA. In that way, a new record value for the PE of a QD microlens could be achieved at $\eta_{\text{Exp}} = (40 \pm 4)\%$. It was measured with an NA of 0.4 of the external collection optics while the microobjective served to collect and collimate the emission with an NA of 0.7. This proved the great potential of on-chip optical elements created by 3-D direct laser writing, which can be easily aligned to QD microlenses.

Consequently, the concept was taken a step further towards a direct fiber-coupling ap-

proach using two microobjectives and a fiber mount created with that technique. Although the coupling efficiency into the fiber was still rather low, the emission from the chosen QD microlens could be clearly identified in the spectrum of the fiber-coupled device, showing that an accurate alignment of the fiber to the QD microlens could be achieved. The efficiency can probably be improved by optimization of the microobjective design and the distance between fiber and sample.

Challenging tasks remain in the field of single-photon technologies. Scaling is an issue for all kinds of sources proposed so far, however significant progress was achieved with QDs by controlled growth [Meh07, Atk08, Unr12], by deterministic processing methods as presented in this work or by a combination of both techniques [Kag18].

Similarly, the on-chip integration of single-photon sources with other optical elements, such as an excitation laser source, waveguides, beam splitters and detectors, is a field with a large potential for further insights into quantum optical effects [Die16, Mun17]. Progress in this field will lead to compact device solutions for the challenges of quantum communication and computation. Here, deterministic methods such as in-situ EBL bring further significant advantages, as the self-assembled QDs can be precisely integrated into complex waveguide systems [Sch18b]. Such devices could also benefit from the integration of a backside gold mirror or a tuning mechanism as introduced in this thesis.

To achieve high on-demand emission rates, an electrical excitation of QDs located inside a p-i-n diode is beneficial, as previously demonstrated in combination with tunable sources [Tro12a] as well as microlenses [Sch16a]. Consequently, an electrically triggered, bright and tunable single-photon source could be created by a combination of both approaches. For commercial applications of single-photon sources, it is a challenge to work with devices that need to be cooled to cryogenic temperatures. First approaches of room temperature operation with nitride-based [Hol14, Hol16] and II-VI QDs [Mic00a, Ari08] have already been made. Their performance, however, is worse compared to InGaAs QDs at cryogenic temperatures in terms of linewidth, suppression of multi-photon emission events and visibility. Another way to tackle this problem is to use the permanently improving cryogenic technology to make cooling systems as small and transportable as possible. It could already be demonstrated that QD microlenses can be used inside a Stirling cryocooler at a temperature of $T = 40$ K [Sch18a]. If this approach could be connected with a high fiber-coupling efficiency, e.g. by use of 3-D written microstructures, together with a strain tuning mechanism and electrical contacts, we would gain a stand-alone plug-and-play single-photon source while maintaining the excellent emission characteristics demonstrated with QD microlenses. This could allow us to enable the implementation of large-scale quantum

networks in the future.

Bibliography

- [Aar13] S. Aaronson and A. Arkhipov, *The Computational Complexity of Linear Optics*, Theory of Computing **9**(4), p. 143 (2013).
- [Abb09] M. Abbarchi, C. Mastrandrea, T. Kuroda, T. Mano, A. Vinattieri, K. Sakoda and M. Gurioli, *Poissonian statistics of excitonic complexes in quantum dots*, Journal of Applied Physics **106**(5), p. 053504 (2009).
- [Abe17] J. Aberl, P. Klenovský, J. S. Wildmann, J. Martín-Sánchez, T. Fromherz, E. Zallo, J. Humlíček, A. Rastelli and R. Trotta, *Inversion of the exciton built-in dipole moment in In(Ga)As quantum dots via nonlinear piezoelectric effect*, Physical Review B **96**, p. 045414 (2017).
- [Ada93] S. Adachi, *Properties of Aluminium Gallium Arsenide*, INSPEC (1993).
- [Ada05] S. Adachi, *Electron and Hole Deformation Potentials*, in *Physical Properties of III-V Semiconductor Compounds*, chapter 8, Wiley-Blackwell (2005), URL <https://onlinelibrary.wiley.com/doi/abs/10.1002/352760281X.ch8>.
- [Aic04] T. Aichele, V. Zwiller and O. Benson, *Visible single-photon generation from semiconductor quantum dots*, New Journal of Physics **6**, p. 90 (2004).
- [Ako11] N. Akopian, L. Wang, A. Rastelli, O. Schmidt and V. Zwiller, *Hybrid semiconductor-atomic interface: Slowing down single photons from a quantum dot*, Nature Photonics **5**, p. 230 (2011).
- [Alb10] F. Albert, S. Stobbe, C. Schneider, T. Heindel, S. Reitzenstein, S. Höfling, P. Lodahl, L. Worschech and A. Forchel, *Quantum efficiency and oscillator strength of site-controlled InAs quantum dots*, Applied Physics Letters **96**(15), p. 151102 (2010).
- [Ari08] R. Arians, A. Gust, T. Kümmell, C. Kruse, S. Zaitsev, G. Bacher and D. Hommel, *Electrically driven single quantum dot emitter operating at room temperature*, Applied Physics Letters **93**(17), 173506 (2008).

- [Asp82] A. Aspect, J. Dalibard and G. Roger, *Experimental Test of Bell's Inequalities Using Time-Varying Analyzers*, Physical Review Letters **49**, p. 1804 (1982).
- [Atk08] P. Atkinson, S. Kiravittaya, M. Benyoucef, A. Rastelli and O. G. Schmidt, *Site-controlled growth and luminescence of InAs quantum dots using in situ Ga-assisted deoxidation of patterned substrates*, Applied Physics Letters **93**(10), p. 101908 (2008).
- [Awa97] K. Awada, D. Jackson, J. Williams, D. Wilton, S. Baumann and P. A.C., *Computational aspects of finite element modeling in EEG source localization*, IEEE Transactions on Biomedical Engineering **44**(8), p. 736 (1997).
- [Bah90] T. B. Bahder, *Eight-band k - p model of strained zinc-blende crystals*, Physical Review B **41**, p. 11992 (1990).
- [Bar50] J. Bardeen and W. Shockley, *Deformation Potentials and Mobilities in Non-Polar Crystals*, Physical Review **80**, p. 72 (1950).
- [Bar02] W. L. Barnes, G. Björk, J. M. Gérard, P. Jonsson, J. A. E. Wasey, P. T. Worthing and V. Zwiller, *Solid-state single photon sources: light collection strategies*, The European Physical Journal D **18**(2), p. 197 (2002).
- [Bay99] M. Bayer, A. Kuther, A. Forchel, A. Gorbunov, V. B. Timofeev, F. Schäfer, J. P. Reithmaier, T. L. Reinecke and S. N. Walck, *Electron and Hole g Factors and Exchange Interaction from Studies of the Exciton Fine Structure in $\text{In}_{0.60}\text{Ga}_{0.40}\text{As}$ Quantum Dots*, Physical Review Letters **82**, p. 1748 (1999).
- [Bay00] M. Bayer, O. Stern, P. Hawrylak, S. Fafard and A. Forchel, *Hidden symmetries in the energy levels of excitonic 'artificial atoms'*, Nature **405**, p. 923 (2000).
- [Bay02] M. Bayer, G. Ortner, O. Stern, A. Kuther, A. A. Gorbunov, A. Forchel, P. Hawrylak, S. Fafard, K. Hinzer, T. L. Reinecke, S. N. Walck, J. P. Reithmaier, F. Klopff and F. Schäfer, *Fine structure of neutral and charged excitons in self-assembled $\text{In}(\text{Ga})\text{As}/(\text{Al})\text{GaAs}$ quantum dots*, Physical Review B **65**, p. 195315 (2002).
- [BB18] F. Basso Basset, S. Bietti, M. Reindl, L. Esposito, A. Fedorov, D. Huber, A. Rastelli, E. Bonera, R. Trotta and S. Sanguinetti, *High-Yield Fabrication of Entangled Photon Emitters for Hybrid Quantum Networking Using High-Temperature Droplet Epitaxy*, Nano Letters **18**(1), p. 505 (2018).

- [Büc12] T. Bückmann, N. Stenger, J. Kadic, M. and Kaschke, A. Frölich, T. Kennerknecht, C. Eberl, M. Thiel and M. Wegener, *Tailored 3D Mechanical Metamaterials Made by Dip-in Direct-Laser-Writing Optical Lithography*, *Advanced Materials* **24**(20), p. 2710 (2012).
- [Bec01] C. Becher, A. Kiraz, P. Michler, A. Imamoglu, W. V. Schoenfeld, P. M. Petroff, L. Zhang and E. Hu, *Nonclassical radiation from a single self-assembled InAs quantum dot*, *Physical Review B* **63**, p. 121312 (2001).
- [Bel64] J. S. Bell, *On the Einstein Podolsky Rosen paradox*, *Physics* **1**(3), p. 195 (1964).
- [Ben84] C. H. Bennett and G. Brassard, *Quantum Cryptography: Public key distribution and coin tossing*, *Proceedings of IEEE International Conference on Computers, Systems and Signal Processing, Bangalore, India* **1**, p. 175 (1984).
- [Ben92] C. H. Bennett, F. Bessette, G. Brassard, L. Salvail and J. Smolin, *Experimental quantum cryptography*, *Journal of Cryptology* **5**(1), p. 3 (1992).
- [Ben98] H. Benisty, H. D. Neve and C. Weibuch, *Impact of Planar Microcavity Effects on Light Extraction - Part I: Basic Concepts and Analytical Trends*, *IEEE Journal of Quantum Electronics* **34**(9), p. 1612 (1998).
- [Ben00] O. Benson, C. Santori, M. Pelton and Y. Yamamoto, *Regulated and Entangled Photons from a Single Quantum Dot*, *Physical Review Letters* **84**(11), p. 2513 (2000).
- [Ben10] A. J. Bennett, R. B. Patel, J. Skiba-Szymanska, C. A. Nicoll, I. Farrer, D. A. Ritchie and A. J. Shields, *Giant Stark effect in the emission of single semiconductor quantum dots*, *Applied Physics Letters* **97**(3), 031104 (2010).
- [Bes06] G. Bester, X. Wu, D. Vanderbilt and A. Zunger, *Importance of Second-Order Piezoelectric Effects in Zinc-Blende Semiconductors*, *Physical Review Letters* **96**, p. 187602 (2006).
- [Bil18] M. R. Billah, M. Blaicher, T. Hoose, P.-I. Dietrich, P. Marin-Palomo, N. Lindenmann, A. Nestic, U. Hofmann, A. Troppenz, M. Moehrle, S. Randel, W. Freude and K. Koos, *Hybrid integration of silicon photonics circuits and InP lasers by photonic wire bonding*, *Optica* **5**(7), p. 876 (2018).
- [Bor01] P. Borri, W. Langbein, S. Schneider, U. Woggon, R. L. Sellin, D. Ouyang and D. Bimberg, *Ultralong Dephasing Time in InGaAs Quantum Dots*, *Physical Review Letters* **87**, p. 157401 (2001).

- [Bou18] S. Bounouar, C. de la Haye, M. Strauß, P. Schnauber, A. Thoma, M. Gschrey, J.-H. Schulze, A. Strittmatter, S. Rodt and S. Reitzenstein, *Generation of maximally entangled states and coherent control in quantum dot microlenses*, Applied Physics Letters **112**(15), p. 153107 (2018).
- [Bra00] G. Brassard, N. Lütkenhaus, T. Mor and B. C. Sanders, *Limitations on Practical Quantum Cryptography*, Physical Review Letters **85**, p. 1330 (2000).
- [Bri25] P. W. Bridgman, *Certain Physical Properties of Single Crystals of Tungsten, Antimony, Bismuth, Tellurium, Cadmium, Zinc, and Tin. (Various Physical Properties of Rubidium and Caesium and the Resistance of Potassium Under Pressure.-The Effect of Tension on the Transverse and Longitudinal Resistance of Metals.)*, volume 60 of *Proceedings of the American Academy of Arts and Sciences*, American Academy of Arts and Sciences (1925), URL <https://books.google.de/books?id=7BMYMwEACAAJ>.
- [Bri98] H.-J. Briegel, W. Dür, J. I. Cirac and P. Zoller, *Quantum Repeaters: The Role of Imperfect Local Operations in Quantum Communication*, Physical Review Letters **81**, p. 5932 (1998).
- [Bro25] L. de Broglie, *Recherches sur la théorie des quanta*, Annales de Physique. **10**(3), p. 22 (1925).
- [BW11] A. Beya-Wakata, P.-Y. Prodhomme and G. Bester, *First- and second-order piezoelectricity in III-V semiconductors*, Physical Review B **84**, p. 195207 (2011).
- [Byl03] J. Bylander, I. Robert-Philip and I. Abram, *Interference and correlation of two independent photons*, The European Physical Journal D - Atomic, Molecular, Optical and Plasma Physics **22**(2), p. 295 (2003).
- [Cad16] D. Cadeddu, J. Teissier, F. R. Braakman, N. Gregersen, P. Stepanov, J.-M. Gérard, J. Claudon, R. J. Warburton, M. Poggio and M. Munsch, *A fiber-coupled quantum-dot on a photonic tip*, Applied Physics Letters **108**(1), p. 011112 (2016).
- [Che89] L. P. Chew, *Constrained Delaunay Triangulations*, Algorithmica **4**, p. 97 (1989).
- [Che13] E. A. Chekhovich, M. N. Makhonin, A. I. Tartakovskii, A. Yacoby, H. Bluhm, K. C. Nowack and L. M. K. Vandersypen, *Nuclear spin effects in semiconductor quantum dots*, Nature Materials **12**, p. 494 (2013).

- [Che16] Y. Chen, I. E. Zadeh, K. D. Jöns, A. Fognini, M. E. Reimer, J. Zhang, D. Dalacu, P. J. Poole, F. Ding, V. Zwiller and O. G. Schmidt, *Controlling the exciton energy of a nanowire quantum dot by strain fields*, Applied Physics Letters **108**(18), p. 182103 (2016).
- [Che18] Y. Chen, M. Zopf, R. Keil, F. Ding and O. G. Schmidt, *Highly-efficient extraction of entangled photons from quantum dots using a broadband optical antenna*, Nature Communications **9**(2994) (2018).
- [Chi04] D. Chithrani, R. L. Williams, J. Lefebvre, P. J. Poole and G. C. Aers, *Optical spectroscopy of single, site-selected, InAs/InP self-assembled quantum dots*, Applied Physics Letters **84**(6), p. 978 (2004).
- [Cho75] A. Cho and J. Arthur, *Molecular beam epitaxy*, Progress in Solid State Chemistry **10**, p. 157 (1975).
- [Cho08] K. Choi, H. Deng, J. Laurat and H. Kimble, *Mapping photonic entanglement into and out of a quantum memory*, Nature **452**, p. 67 (2008).
- [Cla08] J. Clarke and F. K. Wilhelm, *Superconducting quantum bits*, Nature **453**, p. 1031 (2008).
- [Cla10] J. Claudon, J. Bleuse, N. S. Malik, M. Bazin, P. Jaffrennou, N. Gregersen, C. Sauvan, P. Lalanne and J.-M. Gérard, *A highly efficient single-photon source based on a quantum dot in a photonic nanowire*, Nature Photonics **4**, p. 174 (2010).
- [Col00] C. A. Colinge, *Wafer bonding for micro-electromechanical systems (mems)*, in P. L. F. Hemment, V. S. Lysenko and A. N. Nazarov (Editor), *Perspectives, Science and Technologies for Novel Silicon on Insulator Devices*, p. 269–280, Springer Netherlands, Dordrecht (2000), URL https://doi.org/10.1007/978-94-011-4261-8_26.
- [Con75] L. Condra, J. Svitak and A. Pense, *The High Temperature Deformation Properties of Gold and Thermocompression Bonding*, IEEE Transactions on Parts, Hybrids, and Packaging **11**(4), p. 290 (1975).
- [Dal08] P. A. Dalgarno, J. McFarlane, D. Brunner, R. W. Lambert, B. D. Gerardot, R. J. Warburton, K. Karrai, A. Badolato and P. M. Petroff, *Hole recapture limited single photon generation from a single n-type charge-tunable quantum dot*, Applied Physics Letters **92**(19), p. 193103 (2008).

- [Dav17] R. S. Daveau, K. C. Balram, T. Pregolato, J. Liu, E. H. Lee, J. D. Song, V. Verma, R. Mirin, S. W. Nam, L. LMidolo, S. Stobbe, K. Srinivasan and P. Lodahl, *Efficient fiber-coupled single-photon source based on quantum dots in a photonic-crystal waveguide*, *Optica* **4**(2), p. 178 (2017).
- [Deu04] M. Deubel, G. von Freymann, M. Wegener, S. Pereira and C. Soukoulis, *Direct laser writing of three-dimensional photonic-crystal templates for telecommunications*, *Nature Materials* **3**, p. 444 (2004).
- [Die16] C. P. Dietrich, A. Fiore, M. G. Thompson, M. Kamp and S. Höfling, *GaAs integrated quantum photonics: Towards compact and multi-functional quantum photonic integrated circuits*, *Laser & Photonics Reviews* **10**(6), p. 870 (2016).
- [Dim14] F. Dimroth, M. Grave, P. Beutel, U. Fiedeler, C. Karcher, T. N. D. Tibbits, E. Oliva, G. Siefer, M. Schachtner, A. Wekkeli, A. W. Bett, R. Krause, M. Piccin, N. Blanc, C. Drazek, E. Guiot, B. Ghyselen, T. Salvetat, A. Tauzin, T. Signamarcheix, A. Dobrich, T. Hannappel and K. Schwarzburg, *Wafer bonded four-junction GaInP/GaAs//GaInAsP/GaInAs concentrator solar cells with 44.7% efficiency*, *Progress in Photovoltaics: Research and Applications* **22**(3), p. 277 (2014).
- [Din10] F. Ding, R. Singh, J. D. Plumhof, T. Zander, V. Křápek, Y. H. Chen, M. Benyoucef, V. Zwiller, K. Dörr, G. Bester, A. Rastelli and O. G. Schmidt, *Tuning the Exciton Binding Energies in Single Self-Assembled InGaAs/GaAs Quantum Dots by Piezoelectric-Induced Biaxial Stress*, *Physical Review Letters* **104**, p. 067405 (2010).
- [Din16] X. Ding, Y. He, Z.-C. Duan, N. Gregersen, M.-C. Chen, S. Unsleber, S. Maier, C. Schneider, M. Kamp, S. Höfling, C.-Y. Lu and J.-W. Pan, *On-Demand Single Photons with High Extraction Efficiency and Near-Uncertainty Indistinguishability from a Resonantly Driven Quantum Dot in a Micropillar*, *Physical Review Letters* **116**, p. 020401 (2016).
- [Dis95] A. S. Dissanayake, J. Y. Lin and H. X. Jiang, *Quantum-confined Stark effects in CdS_{1-x}Se_x quantum dots*, *Physical Review B* **51**, p. 5457 (1995).
- [Dou08] A. Dousse, L. Lanco, J. Suffczyński, E. Semenova, A. Miard, A. Lemaître, I. Sagnes, C. Roblin, J. Bloch and P. Senellart, *Controlled Light-Matter Coupling for a Single Quantum Dot Embedded in a Pillar Microcavity Using Far-Field Optical Lithography*, *Physical Review Letters* **101**, p. 267404 (2008).

- [Dro98] A. Drost, G. Klink, S. Scherbaum and M. Feil, *Simultaneous fabrication of dielectric and electric joints by wafer bonding*, Proc. SPIE: Micromachined Devices and Components IV **3514**, p. 10 (1998).
- [Dua01] L.-M. Duan, J. I. Lukin, M. D. and Cirac and P. Zoller, *Long-distance quantum communication with atomic ensembles and linear optics*, Nature **414**, p. 413 (2001).
- [Duo17] M. Duocastella, G. Vicidomini, K. Korobchevskaya, K. Pydzińska, M. Ziólek, A. Diaspro and G. de Miguel, *Improving the Spatial Resolution in Direct Laser Writing Lithography by Using a Reversible Cationic Photoinitiator*, The Journal of Physical Chemistry C **121**(31), p. 16970 (2017).
- [Eat94] W. P. Eaton, S. H. Risbud and R. L. Smith, *Silicon wafer-to-wafer bonding at $T < 200$ °C with polymethylmethacrylate*, Applied Physics Letters **65**(4), p. 439 (1994).
- [Eke91] A. K. Ekert, *Quantum cryptography based on Bell's theorem*, Physical Review Letters **67**(6), p. 661 (1991).
- [Eki81] A. Ekimov and A. A. Onushzhenko, *Quantum size effect in three-dimensional microscopic semiconductor crystals*, JETP Lett **34**, p. 345 (1981).
- [Far08] T. Farrow, P. See, A. J. Bennett, M. B. Ward, P. Atkinson, K. Cooper, D. J. P. Ellis, D. C. Unitt, D. A. Ritchie and A. J. Shields, *Single-photon emitting diode based on a quantum dot in a micro-pillar*, Nanotechnology **19**(34), p. 345401 (2008).
- [Fis10] J. Fischer, G. von Freymann and M. Wegener, *The Materials Challenge in Diffraction-Unlimited Direct-Laser-Writing Optical Lithography*, Advanced Materials **22**(32), p. 3578 (2010).
- [Fis13] J. Fischer and M. Wegener, *Three-dimensional optical laser lithography beyond the diffraction limit*, Laser & Photonics Reviews **7**(1), p. 22 (2013).
- [Fis17] S. Fischbach, A. Schlehahn, A. Thoma, N. Srocka, T. Gissibl, S. Ristok, S. Thiele, A. Kaganskiy, A. Strittmatter, T. Heindel, S. Rodt, A. Herkommer, H. Giessen and S. Reitzenstein, *Single Quantum Dot with Microlens and 3D-Printed Micro-objective as Integrated Bright Single-Photon Source*, ACS Photonics **4**(6), p. 1327 (2017).

- [Fis18] S. Fischbach, M. v. Helversen, M. Schmidt, A. Kaganskiy, R. Schmidt, A. Schliwa, T. Heindel, S. Rodt and S. Reitzenstein, *A deterministically fabricated spectrally-tunable quantum dot based single-photon source*, arXiv e-prints **1805.10623v1** [[cond-mat.mes-hall](#)] (2018).
- [För03] J. Förstner, C. Weber, J. Danckwerts and A. Knorr, *Phonon-Assisted Damping of Rabi Oscillations in Semiconductor Quantum Dots*, Physical Review Letters **91**, p. 127401 (2003).
- [Fra49] F. C. Frank and J. H. van der Merwe, *One-Dimensional Dislocations. I. Static Theory*, Proceedings of the Royal Society A: Mathematical, Physical and Engineering Sciences **198**, p. 205 (1949).
- [Fri09] I. Friedler, C. Sauvan, J. P. Hugonin, P. Lalanne, J. Claudon and J. M. Gérard, *Solid-state single photon sources: the nanowire antenna*, Optics Express **17**(4), p. 2095 (2009).
- [Gaa10] S. Gaan, G. He, R. M. Feenstra, J. Walker and E. Towe, *Size, shape, composition, and electronic properties of InAs/GaAs quantum dots by scanning tunneling microscopy and spectroscopy*, Journal of Applied Physics **108**(11), p. 114315 (2010).
- [Gam96] D. Gammon, E. S. Snow, B. V. Shanabrook, D. S. Katzer and D. Park, *Fine Structure Splitting in the Optical Spectra of Single GaAs Quantum Dots*, Physical Review Letters **76**, p. 3005 (1996).
- [Gan13] Z. Gan, Y. Cao, R. A. Evans and M. Gu, *Three-dimensional deep sub-diffraction optical beam lithography with 9 nm feature size*, Nature Communications **4**, p. 2061 (2013).
- [Gaz13] O. Gazzano, S. Michaelis de Vasconcellos, C. Arnold, A. K. Nowak, E. Galopin, I. Sagnes, L. Lanco, A. Lemaître and P. Senellart, *Bright solid-state sources of indistinguishable single photons.*, Nature communications **4**, p. 1425 (2013).
- [Gis16a] T. Gissibl, M. Schmid and H. Giessen, *Spatial beam intensity shaping using phase masks on single-mode optical fibers fabricated by femtosecond direct laser writing*, Optica **3**(4), p. 448 (2016).
- [Gis16b] T. Gissibl, S. Thiele, A. Herkommer and H. Giessen, *Two-photon direct laser writing of ultracompact multi-lens objectives*, Nature Photonics **10**, p. 554 (2016).

- [Gla63] R. J. Glauber, *The Quantum Theory of Optical Coherence*, Physical Review **130**, p. 2529 (1963).
- [GM31] M. Göppert-Mayer, *Über Elementarakte mit zwei Quantensprüngen*, Annalen der Physik **401**, p. 273 (1931).
- [Gru95] M. Grundmann, O. Stier and D. Bimberg, *InAs/GaAs pyramidal quantum dots: Strain distribution, optical phonons, and electronic structure*, Physical Review B **52**(16), p. 11969 (1995).
- [Gru10] M. Grundmann, *The Physics of Semiconductors*, Graduate Texts in Physics, Springer-Verlag Berlin Heidelberg (2010).
- [Gsc13] M. Gschrey, F. Gericke, A. Schüßler, R. Schmidt, J.-H. Schulze, T. Heindel, S. Rodt, A. Strittmatter and S. Reitzenstein, *In situ electron-beam lithography of deterministic single-quantum-dot mesa-structures using low-temperature cathodoluminescence spectroscopy*, Applied Physics Letters **102**(25), 251113 (2013).
- [Gsc15a] M. Gschrey, R. Schmidt, J.-H. Schulze, A. Strittmatter, S. Rodt and S. Reitzenstein, *Resolution and alignment accuracy of low-temperature in situ electron beam lithography for nanophotonic device fabrication*, Journal of Vacuum Science & Technology B **33**(2), p. 021603 (2015).
- [Gsc15b] M. Gschrey, A. Thoma, P. Schnauber, M. Seifried, R. Schmidt, B. Wohlfeil, L. Krüger, J.-H. Schulze, T. Heindel, S. Burger, F. Schmidt, A. Strittmatter, S. Rodt and S. Reitzenstein, *Highly indistinguishable photons from deterministic quantum-dot microlenses utilizing three-dimensional in situ electron-beam lithography*, Nature Communications **6**, p. 7662 (2015).
- [Guh15] S. Guha, H. Krovi, C. A. Fuchs, Z. Dutton, J. A. Slater, C. Simon and W. Tittel, *Rate-loss analysis of an efficient quantum repeater architecture*, Physical Review A **92**, p. 022357 (2015).
- [Hab13] F. Habashi, *Gold, physical and chemical properties*, in R. H. Kretsinger, V. N. Uversky and E. A. Permyakov (Editor), *Encyclopedia of Metalloproteins*, p. 932–933, Springer New York (2013), URL https://doi.org/10.1007/978-1-4614-1533-6_540.
- [Han18] L. Hanschke, K. A. Fischer, S. Appel, D. Lukin, J. Wierzbowski, S. Sun, R. Trivedi, J. Vučković, J. J. Finley and K. Müller, *Quantum dot single-photon*

- sources with ultra-low multi-photon probability*, npj Quantum Information **4**(43) (2018).
- [HB56] R. Hanbury-Brown and R. Q. Twiss, *Correlation between photons in two coherent beams of light*, Nature **177**(4497), p. 27 (1956).
- [Hei15] Y.-M. He, G. Clark, J. R. Schaibley, Y. He, M.-C. Chen, Y.-J. Wei, X. Ding, Q. Zhang, W. Yao, X. Xu, C.-Y. Lu and J.-W. Pan, *Single quantum emitters in monolayer semiconductors*, Nature Nanotechnology **10**(6), p. 497 (2015).
- [Hei97] F. Heinrichsdorff, M.-H. Mao, N. Kirstaedter, A. Krost, D. Bimberg, A. O. Kosogov and P. Werner, *Room-temperature continuous-wave lasing from stacked InAs/GaAs quantum dots grown by metalorganic chemical vapor deposition*, Applied Physics Letters **71**(1), p. 22 (1997).
- [Hei98] F. Heinrichsdorff, M. Grundmann, O. Stier, A. Krost and D. Bimberg, *Influence of In/Ga intermixing on the optical properties of InGaAs/GaAs quantum dots*, Journal of Crystal Growth **195**(1), p. 540 (1998).
- [Hei10] T. Heindel, C. Schneider, M. Lermer, S. H. Kwon, T. Braun, S. Reitzenstein, S. Höfling, M. Kamp and A. Forchel, *Electrically driven quantum dot-micropillar single photon source with 34% overall efficiency*, Applied Physics Letters **96**(1), p. 011107 (2010).
- [Hei17] T. Heindel, S. Rodt and R. S., *Single-Photon Sources Based on Deterministic Quantum-Dot Microlenses*, in *Quantum Dots for Quantum Information Technologies*, Nanooptics and Nanophotonics, Springer (2017).
- [Hel98] W. Heller, U. Bockelmann and G. Abstreiter, *Electric-field effects on excitons in quantum dots*, Physical Review B **57**, p. 6270 (1998).
- [Hen15] B. J. Hensen, H. Bernien, A. E. Dréau, A. Reiserer, N. Kalb, M. S. Blok, M. Ruitenberg, R. F. L. Vermeulen, R. N. Schouten, C. Abellan, W. Amaya, V. Pruneri, M. W. Mitchell, M. Markham, D. J. Twitchen, D. Elkouss, S. D. C. Wehner, T. H. Taminiiau and R. Hanson, *Loophole-free Bell inequality violation using electron spins separated by 1.3 kilometres*, Nature **526**(7575), p. 682 (2015).
- [Her10a] A. Herklotz, J. D. Plumhof, A. Rastelli, O. G. Schmidt, L. Schultz and K. Dörr, *Electrical characterization of PMN-28%PT(001) crystals used as thin-film substrates*, Journal of Applied Physics **108**(9), p. 094101 (2010).

- [Her10b] C. Hermannstädter, G. J. Beirne, M. Witzany, M. Heldmaier, J. Peng, G. Bester, L. Wang, A. Rastelli, O. G. Schmidt and P. Michler, *Influence of the charge carrier tunneling processes on the recombination dynamics in single lateral quantum dot molecules*, Physical Review B **82**, p. 085309 (2010).
- [Höf17] B. Höfer, J. Zhang, J. Wildmann, E. Zallo, R. Trotta, F. Ding, A. Rastelli and O. G. Schmidt, *Independent tuning of excitonic emission energy and decay time in single semiconductor quantum dots*, Applied Physics Letters **110**(15), p. 151102 (2017).
- [Hol14] M. J. Holmes, K. Choi, S. Kako, M. Arita and Y. Arakawa, *Room-Temperature Triggered Single Photon Emission from a III-Nitride Site-Controlled Nanowire Quantum Dot*, Nano Letters **14**(2), p. 982 (2014).
- [Hol16] M. J. Holmes, S. Kako, K. Choi, M. Arita and Y. Arakawa, *Single Photons from a Hot Solid-State Emitter at 350 K*, ACS Photonics **3**(4), p. 543 (2016).
- [Hub17] D. Huber, M. Reindl, Y. Huo, H. Huang, J. S. Wildmann, O. G. Schmidt, A. Rastelli and R. Trotta, *Highly indistinguishable and strongly entangled photons from symmetric GaAs quantum dots*, Nature Communications **8**, p. 15506 (2017).
- [Hub18a] D. Huber, M. Reindl, J. Aberl, Rastelli and R. A. Trotta, *Semiconductor quantum dots as an ideal source of polarization-entangled photon pairs on-demand: a review*, Journal of Optics **20**, p. 073002 (2018).
- [Hub18b] D. Huber, M. Reindl, S. F. Covre da Silva, C. Schimpf, J. Martín-Sánchez, H. Huang, G. Piredda, J. Edlinger, A. Rastelli and R. Trotta, *Strain-Tunable GaAs Quantum Dot: A Nearly Dephasing-Free Source of Entangled Photon Pairs on Demand*, Physical Review Letters **121**, p. 033902 (2018).
- [Ils93] P. Ils, M. Michel, A. Forchel, I. Gyuro, M. Klenk and E. Zielinski, *Fabrication and optical properties of InGaAs/InP quantum wires and dots with strong lateral quantization effects*, Journal of Vacuum Science & Technology B: Microelectronics and Nanometer Structures Processing, Measurement, and Phenomena **11**(6), p. 2584 (1993).
- [Jog15] C. S. Jog, *Continuum Mechanics: Foundations and Applications of Mechanics*, volume 1, Cambridge University Press (2015).

- [Joh76] D. R. Johnson and E. L. Chavez, *Characterization of the Thermosonic Wire Bonding Technique*, Proc. ISHM (1976).
- [Joh10] J. Johansen, B. Julsgaard, S. Stobbe, J. M. Hvam and P. Lodahl, *Probing long-lived dark excitons in self-assembled quantum dots*, Physical Review B **81**, p. 081304 (2010).
- [Joh17] S. Johnson, P. R. Dolan and J. M. Smith, *Diamond photonics for distributed quantum networks*, Progress in Quantum Electronics **55**, p. 129 (2017).
- [J.T07] J. Tian, P. Han, X. Huang, H. Pan, J. F. C. III and D. A. Payne, *Improved stability for piezoelectric crystals grown in the lead indium niobate–lead magnesium niobate–lead titanate system*, Applied Physics Letters **91**(22), p. 222903 (2007).
- [Jun00] H. Jung and D.-G. Gweon, *Creep characteristics of piezoelectric actuators*, Review of Scientific Instruments **71**(4), p. 1896 (2000).
- [Kag16] A. Kaganskiy, T. Heuser, R. Schmidt, S. Rodt and S. Reitzenstein, *CSAR 62 as negative-tone resist for high-contrast e-beam lithography at temperatures between 4 K and room temperature*, Journal of Vacuum Science & Technology B, Nanotechnology and Microelectronics: Materials, Processing, Measurement, and Phenomena **34**(6), p. 061603 (2016).
- [Kag18] A. Kaganskiy, S. Fischbach, A. Strittmatter, S. Rodt, T. Heindel and S. Reitzenstein, *Enhancing the photon-extraction efficiency of site-controlled quantum dots by deterministically fabricated microlenses*, Optics Communications **413**, p. 162 (2018).
- [Kai61] W. Kaiser and C. G. B. Garrett, *Two-Photon Excitation in CaF₂: Eu²⁺*, Physical Review Letters **7**, p. 229 (1961).
- [Kän57] W. Känzig, *Ferroelectrics and antiferroelectrics*, in F. Seitz and D. Turnbull (Editor), *Solid State Physics*, volume 4, Academic Press In. (1957).
- [Kan72] K. Kanaya and S. Okayama, *Penetration and energy-loss theory of electrons in solid targets*, Journal of Physics D: Applied Physics **5**(1), p. 43 (1972).
- [Kan95] S. Y. Kang, P. M. Williams, T. S. McLaren and Y. C. Lee, *Studies of thermosonic bonding for flip-chip assembly*, Materials Chemistry and Physics **42**(1), p. 31 (1995).

- [Kim77] H. J. Kimble, M. Dagenais and L. Mandel, *Photon Antibunching in Resonance Fluorescence*, Physical Review Letters **39**, p. 691 (1977).
- [Kim00] H. J. Kimble, *The quantum internet*, Nature **453**, p. 1023 (2000).
- [Kis08] C. Kistner, T. Heindel, C. Schneider, A. Rahimi-Iman, S. Reitzenstein, S. Höfling and A. Forchel, *Demonstration of strong coupling via electro-optical tuning in high-quality QD-micropillar systems*, Optics Express **16**(19), p. 15006 (2008).
- [Kni01] E. Knill, R. Laflamme and G. J. Milburn, *A scheme for efficient quantum computation with linear optics*, Nature **409**(6816), p. 46 (2001).
- [Kog93] N. Koguchi, K. Ishige and S. Takashi, *New selective molecular-beam epitaxy growth method for direct formation of GaAs quantum dots*, Journal of Vacuum Science & Technology B **11**(3), p. 787 (1993).
- [Koj13] T. Kojima, K. Kojima, T. Asano and S. Noda, *Accurate alignment of a photonic crystal nanocavity with an embedded quantum dot based on optical microscopic photoluminescence imaging*, Applied Physics Letters **102**(1), 011110 (2013).
- [Kok07] P. Kok, W. J. Munro, K. Nemoto, T. C. Ralph, J. P. Dowling and G. J. Milburn, *Linear optical quantum computing with photonic qubits*, Reviews of Modern Physics **79**, p. 135 (2007).
- [Kop15] M. Koperski, K. Nogajewski, A. Arora, V. Cherkez, P. Mallet, J.-Y. Veullen, P. Marcus, J. D. and Kossacki and M. Potemski, *Single photon emitters in exfoliated WSe₂ structures*, Nature Nanotechnology **10**, p. 503 (2015).
- [Kow05] K. Kowalik, O. Krebs, A. Lemaître, S. Laurent, P. Senellart, P. Voisin and J. A. Gaj, *Influence of an in-plane electric field on exciton fine structure in InAs-GaAs self-assembled quantum dots*, Applied Physics Letters **86**(4), p. 041907 (2005).
- [Krz90] J. E. Krzanowski, *A transmission electron microscopy study of ultrasonic wire bonding*, IEEE Transactions on Components, Hybrids, and Manufacturing Technology **13**(1), p. 176 (1990).
- [Kuh02] A. Kuhn, M. Hennrich and G. Rempe, *Deterministic Single-Photon Source for Distributed Quantum Networking*, Physical Review Letters **89**, p. 067901 (2002).

- [Kum16] H. Kumano, T. Harada, I. Suemune, H. Nakajima, T. Kuroda, T. Mano, K. Sakoda, S. Odashima and H. Sasakura, *Stable and efficient collection of single photons emitted from a semiconductor quantum dot into a single-mode optical fiber*, Applied Physics Express **9**, p. 032801 (2016).
- [Kur00] C. Kurtsiefer, S. Mayer, P. Zarda and H. Weinfurter, *Stable Solid-State Source of Single Photons*, Physical Review Letters **85**, p. 290 (2000).
- [Kur01] C. Kurtsiefer, P. Zarda, A. Mayer and H. Weinfurter, *The breakdown flash of silicon avalanche photodiodes-back door for eavesdropper attacks?*, Journal of Modern Optics **48**(13), p. 2039 (2001).
- [Kur13] T. Kuroda, T. Mano, N. Ha, H. Nakajima, H. Kumano, B. Urbaszek, M. Jo, M. Abbarchi, Y. Sakuma, K. Sakoda, I. Suemune, X. Marie and T. Amand, *Symmetric quantum dots as efficient sources of highly entangled photons: Violation of Bell's inequality without spectral and temporal filtering*, Physical Review B **88**, p. 041306 (2013).
- [Kwi95] P. G. Kwiat, K. Mattle, H. Weinfurter, A. Zeilinger, A. V. Sergienko and Y. Shih, *New High-Intensity Source of Polarization-Entangled Photon Pairs*, Physical Review Letters **75**, p. 4337 (1995).
- [Lai16] K. Laiho, B. Pressl, A. Schlager, H. Suchomel, M. Kamp, S. Höfling, C. Schneider and G. Weihs, *Uncovering dispersion properties in semiconductor waveguides to study photon-pair generation*, Nanotechnology **27**(43), p. 434003 (2016).
- [Las86] J. B. Lasky, *Wafer bonding for silicon-on-insulator technologies*, Applied Physics Letters **48**(1), p. 78 (1986).
- [Led94] N. N. Ledentsov, V. M. Ustinov, A. Y. Egorov, A. E. Zhukov, M. V. Maksimov, I. G. Tabatadze and P. S. Kop'ev, *Optical properties of heterostructures with InGaAs-GaAs quantum clusters*, Semiconductors **28**, p. 832 (1994).
- [Lee15] C.-M. Lee, H.-J. Lim, C. Schneider, S. Maier, S. Höfling, M. Kamp and Y.-H. Lee, *Efficient single photon source based on μ -fibre-coupled tunable microcavity*, Scientific Reports **5**, p. 14309 (2015).
- [Li10] F. Li, S. Zhang, Z. Xu, X. Wei, J. Luo and T. R. Shroud, *Piezoelectric activity of relaxor-PbTiO₃ based single crystals and polycrystalline ceramics at cryogenic temperatures: Intrinsic and extrinsic contributions*, Applied Physics Letters **96**(19), p. 192903 (2010).

- [Lia18] S.-K. Liao, W.-Q. Cai, J. Handsteiner, B. Liu, J. Yin, L. Zhang, D. Rauch, M. Fink, J.-G. Ren, W.-Y. Liu, Y. Li, Q. Shen, Y. Cao, F.-Z. Li, J.-F. Wang, Y.-M. Huang, L. Deng, T. Xi, L. Ma, T. Hu, L. Li, N.-L. Liu, F. Koidl, P. Wang, Y.-A. Chen, X.-B. Wang, M. Steindorfer, G. Kirchner, C.-Y. Lu, R. Shu, R. Ursin, T. Scheidl, C.-Z. Peng, J.-Y. Wang, A. Zeilinger and J.-W. Pan, *Satellite-Relayed Intercontinental Quantum Network*, Physical Review Letters **120**, p. 030501 (2018).
- [Liu18] F. Liu, A. Brash, J. O'Hara, L. Martins, C. Phillips, R. Coles, B. Royall, E. Clarke, C. Bentham, N. Prtljaga, I. Itskevich, L. Wilson, M. Skolnick and A. Fox, *High Purcell factor generation of coherent on-chip single photons*, Nature Nanotechnology **13**, p. 835 (2018).
- [Lod15] P. Lodahl, S. Mahmoodian and S. Stobbe, *Interfacing single photons and single quantum dots with photonic nanostructures*, Reviews of Modern Physics **87**, p. 347 (2015).
- [Log73] R. A. Logan and F. K. Reinhart, *Optical waveguides in GaAs-AlGaAs epitaxial layers*, Journal of Applied Physics **44**(9), p. 4172 (1973).
- [Loh15] A. Lohrmann, N. Iwamoto, Z. Bodrog, S. Castelletto, T. Ohshima, T. Karle, A. Gali, S. Praver, J. McCallum and B. Johnson, *Single-photon emitting diode in silicon carbide*, Nature Communications **6**(1) (2015).
- [Lud85] M. J. Ludowise, *Metalorganic chemical vapor deposition of III-V semiconductors*, Journal of Applied Physics **58**(8), p. R31 (1985).
- [Ma15] Y. Ma, G. Ballesteros, J. M. Zajac, J. Sun and B. D. Gerardot, *Highly directional emission from a quantum emitter embedded in a hemispherical cavity*, Optics Letters **40**(10), p. 2373 (2015).
- [Mad82] O. Madelung, M. Schulz and H. Weiss (Editor), *Semiconductors, Physics of Group IV Elements and III-V Compounds*, volume 3 of *Landolt-Börnstein. Numerical data and functional relationships in science and technology. New Series*, Springer-Verlag Berlin Heidelberg (1982), URL <https://onlinelibrary.wiley.com/doi/abs/10.1002/crat.2170181018>, <https://onlinelibrary.wiley.com/doi/pdf/10.1002/crat.2170181018>.
- [Mad14] K. H. Madsen, S. Ates, J. Liu, A. Javadi, S. M. Albrecht, I. Yeo, S. Stobbe and P. Lodahl, *Efficient out-coupling of high-purity single photons from a coher-*

- ent quantum dot in a photonic-crystal cavity*, Physical Review B **90**, p. 155303 (2014).
- [Mal65] I. H. Malitson, *Interspecimen Comparison of the Refractive Index of Fused Silica*, Journal of the Optical Society of America **55**(10), p. 1205 (1965).
- [Mal97] S. Malik, C. Roberts, R. Murray and M. Pate, *Tuning self-assembled InAs quantum dots by rapid thermal annealing*, Applied Physics Letters **71**(14), p. 1987 (1997).
- [Man68] H. M. Manasevit, *SINGLE-CRYSTAL GALLIUM ARSENIDE ON INSULATING SUBSTRATES*, Applied Physics Letters **12**, p. 156 (1968).
- [Man10] T. Mano, M. Abbarchi, T. Kuroda, B. McSkimming, A. Ohtake, K. Mitsuishi and K. Sakoda, *Self-Assembly of Symmetric GaAs Quantum Dots on (111)A Substrates: Suppression of Fine-Structure Splitting*, Applied Physics Express **3**(6), p. 065203 (2010).
- [Man15] M. T. Man and H. S. Lee, *Discrete states and carrier-phonon scattering in quantum dot population dynamics*, Scientific Reports **5**, p. 8367 (2015).
- [Mar97] S. Maruo, O. Nakamura and S. Kawata, *Three-dimensional microfabrication with two-photon-absorbed photopolymerization*, Optics Letters **22**(2), p. 132 (1997).
- [Mar15] E. A. S. Marques, L. F. M. da Silva, M. D. Banea and R. J. C. Carbas, *Adhesive Joints for Low- and High-Temperature Use: An Overview*, The Journal of Adhesion **91**(7), p. 556 (2015).
- [McP15] K. M. McPeak, S. V. Jayanti, S. J. P. Kress, S. Meyer, S. Iotti, A. Rossinelli and D. J. Norris, *Plasmonic Films Can Easily Be Better: Rules and Recipes*, ACS Photonics **2**(3), p. 326 (2015).
- [Meh07] M. Mehta, D. Reuter, A. Melnikov, A. D. Wieck and A. Remhof, *Focused ion beam implantation induced site-selective growth of InAs quantum dots*, Applied Physics Letters **91**(12), p. 123108 (2007).
- [Mel03] A. Melliti, M. Maaref, F. Hassen, M. Hjiri, H. Maaref, J. Tignon and B. Sermage, *Radiative recombination lifetime of excitons in self-organized InAs/GaAs quantum dots*, Solid State Communications **128**(6), p. 213 (2003).

- [Mic00a] P. Michler, A. Imamoglu, M. D. Mason, P. J. Carson, G. F. Strouse and S. K. Buratto, *Quantum correlation among photons from a single quantum dot at room temperature*, Nature **406**(6799), p. 968 (2000).
- [Mic00b] P. Michler, A. Kiraz, C. Becher, W. V. Schoenfeld, P. M. Petroff, L. Zhang, E. Hu and A. Imamoglu, *A Quantum Dot Single-Photon Turnstile Device*, Science **290**(5500), p. 2282 (2000).
- [Mon17] N. Montaut, L. Sansoni, E. Meyer-Scott, R. Ricken, V. Quiring, H. Herrmann and C. Silberhorn, *High-Efficiency Plug-and-Play Source of Heralded Single Photons*, Physical Review Applied **8**, p. 024021 (2017).
- [Mun17] P. Munnely, B. Lingnau, M. M. Karow, T. Heindel, M. Kamp, S. Höfling, K. Lüdge, C. Schneider and S. Reitzenstein, *On-chip optoelectronic feedback in a micropillar laser-detector assembly*, Optica **4**(3), p. 303 (2017).
- [Neu17] F. Neukart, G. Compostella, C. Seidel, D. von Dollen, S. Yarkoni and B. Parney, *Traffic Flow Optimization Using a Quantum Annealer*, Frontiers in ICT **4**, p. 29 (2017).
- [Nik01] F. Niklaus, P. Enoksson, E. Kälvesten and G. Stemme, *Low-temperature full wafer adhesive bonding*, Journal of Micromechanics and Microengineering **11**, p. 110 (2001).
- [Nov06] L. Novotny and B. Hecht, *Principles of Nano-Optics*, Cambridge University Press (2006), URL <https://books.google.de/books?id=Qrf036kThTQC>.
- [Oya12] T. G. Oyama, K. Enomoto, Y. Hosaka, A. Oshima, M. Washio and S. Tagawa, *Electron-Beam-Induced Decomposition Mechanisms of High-Sensitivity Chlorinated Resist ZEP520A*, Applied Physics Express **5**(3), p. 036501 (2012).
- [Pal91] E. Palik, *Handbook of Optical Constants of Solids*, Academic Press, Academic Press (1991), URL https://books.google.de/books?id=d4_kRYYS0H8C.
- [Pao65] Y.-H. Pao and P. M. Rentzepis, *LASER-INDUCED PRODUCTION OF FREE RADICALS IN ORGANIC COMPOUNDS*, Applied Physics Letters **6**(5), p. 93 (1965).
- [Pet07] E. Peter, S. Laurent, J. Bloch, J. Hours, S. Varoutsis, I. Robert-Philip, A. Beveratos, A. Lemaître, A. Cavanna, G. Patriarche, P. Senellart and D. Martrou, *Fast radiative quantum dots: From single to multiple photon emission*, Applied Physics Letters **90**(22), p. 223118 (2007).

- [Pik80] A. N. Pikhtin and A. D. Yas'kov, *Dispersion of the Refractive Index of Semiconducting Solid Solutions with the Sphalerite Structure*, Soviet Physics: Semiconductors **14**, p. 389 (1980).
- [Poh08] U. Pohl and A. Strittmatter, *Control of Self-Organized In(Ga)As/GaAs Quantum Dot Growth*, in *Semiconductor Nanostructures*, Editor: Bimberg, D., Springer Science and Business Media (2008).
- [Poh13] U. W. Pohl, *Epitaxy of Semiconductors*, Springer-Verlag Berlin Heidelberg (2013).
- [Pom07] J. Pomplun, S. Burger, L. Zschiedrich and F. Schmidt, *Adaptive finite element method for simulation of optical nano structures*, physica status solidi (b) **244**(10), p. 3419 (2007).
- [Pre13] J. H. Prechtel, A. V. Kuhlmann, J. Houel, L. Greuter, A. Ludwig, D. Reuter, A. D. Wieck and R. J. Warburton, *Frequency-Stabilized Source of Single Photons from a Solid-State Qubit*, Physical Review X **3**, p. 041006 (2013).
- [Pry98] C. Pryor, *Eight-band calculations of strained InAs/GaAs quantum dots compared with one-, four-, and six-band approximations*, Physical Review B **57**, p. 7190 (1998).
- [Pur46] E. M. Purcell, *Spontaneous emission probabilities at radio frequencies*, Proceedings of the American Physical Society **69**, p. 681 (1946).
- [Qu17] J. Qu, M. Kadic, A. Naber and M. Wegener, *Micro-Structured Two-Component 3D Metamaterials with Negative Thermal-Expansion Coefficient from Positive Constituents*, Scientific Reports **7**, p. 40643 (2017).
- [Rau14] M. Rau, T. Heindel, S. Unsleber, T. Braun, J. Fischer, S. Frick, S. Nauerth, C. Schneider, G. Vest, S. Reitzenstein, M. Kamp, A. Forchel, S. Höfling and H. Weinfurter, *Free space quantum key distribution over 500 meters using electrically driven quantum dot single-photon sources - a proof of principle experiment*, New Journal of Physics **16**(4), p. 043003 (2014).
- [Ree88] M. A. Reed, J. N. Randall, R. J. Aggarwal, R. J. Matyi, T. M. Moore and A. E. Wetsel, *Observation of discrete electronic states in a zero-dimensional semiconductor nanostructure*, Physical Review Letters **60**, p. 535 (1988).
- [Rei04] J. Reithmaier, G. Şek, A. Löffler, C. Hofmann, S. Kuhn, S. Reitzenstein, L. Keldysh, V. Kulakovskii, T. Reinecke and A. Forchel, *Strong coupling in*

- a single quantum-dot semiconductor microcavity system*, Nature **432**, p. 197 (2004).
- [Rei06] S. Reitzenstein, A. Bazhenov, A. Gorbunov, C. Hofmann, S. Münch, A. Löffler, M. Kamp, J. P. Reithmaier, V. D. Kulakovskii and A. Forchel, *Lasing in high-Q quantum-dot micropillar cavities*, Applied Physics Letters **89**(5), 051107 (2006).
- [Rei10] S. Reitzenstein and A. Forchel, *Quantum dot micropillars*, Journal of Physics D: Applied Physics **43**(3), p. 033001 (2010).
- [Rei17] M. Reindl, K. D. Jöns, D. Huber, C. Schimpf, Y. Huo, V. Zwiller and R. Rastelli, A. and Trotta, *Phonon-Assisted Two-Photon Interference from Remote Quantum Emitters*, Nano Letters **17**(7), p. 4090 (2017).
- [Res05] K. J. Resch, M. Lindenthal, B. Blauensteiner, H. R. Böhm, A. Fedrizzi, C. Kurtsiefer, A. Poppe, T. Schmitt-Manderbach, M. Taraba, R. Ursin, P. Walther, H. Weier, H. Weinfurter and A. Zeilinger, *Distributing entanglement and single photons through an intra-city, free-space quantum channel*, Optics Express **13**(1), p. 202 (2005).
- [Ril08] M. S. Rill, C. Plet, M. Thiel, I. Staude, G. von Freymann, S. Linden and M. Wegener, *Photonic metamaterials by direct laser writing and silver chemical vapour deposition*, Nature Materials **7**, p. 543 (2008).
- [Rod05] S. Rodt, A. Schliwa, K. Pötschke, F. Guffarth and D. Bimberg, *Correlation of structural and few-particle properties of self-organized InAs/GaAs quantum dots*, Physical Review B **71**, p. 155325 (2005).
- [Rod06] S. Rodt, *Exzitonische Komplexe in einzelnen III-V Quantenpunkten*, phdthesis, Technische Universität Berlin (2006).
- [Roe07] G. Roelkens, J. V. Campenhout, J. Brouckaert, D. V. Thourhout, R. Baets, P. R. Romeo, P. Regreny, A. Kazmierczak, C. Seassal, X. Letartre, G. Hollinger, J. Fedeli, L. D. Cioccio and C. Lagache-Blanchard, *III-V/Si photonics by die-to-wafer bonding*, Materials Today **10**(7), p. 36 (2007).
- [Ryu10] K. K. Ryu, J. W. Chung, B. Lu and T. Palacios, *Wafer Bonding Technology in Nitride Semiconductors for Applications in Energy and Communications*, ECS Transactions **33**(4), p. 125 (2010).
- [Sad09] M. H. Sadd, *Elasticity: Theory, Applications, and Numerics*, Academic Press (2009).

- [Sak12] I. Sakellari, E. Kabouraki, D. Gray, V. Purlys, C. Fotakis, A. Pikulin, N. Bityurin, M. Vamvakaki and M. Farsari, *Diffusion-Assisted High-Resolution Direct Femtosecond Laser Writing*, ACS Nano **6**(3), p. 2302 (2012).
- [Sap15] L. Sapienza, M. Davanço, A. Badolato and K. Srinivasan, *Nanoscale optical positioning of single quantum dots for bright and pure single-photon emission*, Nature Communications **6**(8), p. 7833 (2015).
- [Sch07] A. Schliwa, M. Winkelkemper and D. Bimberg, *Impact of size, shape, and composition on piezoelectric effects and electronic properties of In(Ga)As/GaAs quantum dots*, Physical Review B **76**, p. 205324 (2007).
- [Sch08] C. Schneider, M. Strauß, T. Süner, A. Huggenberger, D. Wiener, S. Reitzenstein, M. Kamp, S. Höfling and A. Forchel, *Lithographic alignment to site-controlled quantum dots for device integration*, Applied Physics Letters **92**(18), 183101 (2008).
- [Sch09a] A. Schliwa, M. Winkelkemper and D. Bimberg, *Few-particle energies versus geometry and composition of $In_xGa_{1-x}As/GaAs$ self-organized quantum dots*, Physical Review B **79**(7), 075443 (2009).
- [Sch09b] A. Schliwa, M. Winkelkemper, A. Lochmann, E. Stock and D. Bimberg, *In(Ga)As/GaAs quantum dots grown on a (111) surface as ideal sources of entangled photon pairs*, Physical Review B **80**(16), 161307 (2009).
- [Sch11] T. Schröder, A. W. Schell, G. Kewes, T. Aichele and O. Benson, *Fiber-Integrated Diamond-Based Single Photon Source*, Nano Letters **11**(1), p. 198 (2011).
- [Sch15a] A. Schlehahn, M. Gaafar, M. Vaupel, M. Gschrey, P. Schnauber, J.-H. Schulze, S. Rodt, A. Strittmatter, W. Stolz, A. Rahimi-Iman, T. Heindel, M. Koch and S. Reitzenstein, *Single-photon emission at a rate of 143 MHz from a deterministic quantum-dot microlens triggered by a mode-locked vertical-external-cavity surface-emitting laser*, Applied Physics Letters **107**(4), p. 041105 (2015).
- [Sch15b] A. Schlehahn, L. Krüger, M. Gschrey, J.-H. Schulze, S. Rodt, A. Strittmatter, T. Heindel and S. Reitzenstein, *Operating single quantum emitters with a compact Stirling cryocooler*, Review of Scientific Instruments **86**(1), p. 013113 (2015).
- [Sch16a] A. Schlehahn, R. Schmidt, C. Hopfmann, J.-H. Schulze, A. Strittmatter, T. Heindel, L. Gantz, E. R. Schmidgall, D. Gershoni and S. Reitzenstein, *Gen-*

- erating single photons at gigahertz modulation-speed using electrically controlled quantum dot microlenses*, Applied Physics Letters **108**(2), p. 021104 (2016).
- [Sch16b] P. Schnauber, R. Schmidt, A. Kaganskiy, T. Heuser, M. Gschrey, S. Rodt and S. Reitzenstein, *Using low-contrast negative-tone PMMA at cryogenic temperatures for 3D electron beam lithography*, Nanotechnology **27**(19), p. 195301 (2016).
- [Sch17] A. Schlehahn, *Entwicklung einer autark operierenden Plug-and-Play-Einzelphotonenemittereinheit*, phdthesis, Technische Universität Berlin, Institut für Festkörperphysik (2017).
- [Sch18a] A. Schlehahn, S. Fischbach, R. Schmidt, A. Kaganskiy, A. Strittmatter, S. Rodt, T. Heindel and S. Reitzenstein, *A stand-alone fiber-coupled single-photon source*, Scientific Reports **8**(1340) (2018).
- [Sch18b] P. Schnauber, J. Schall, S. Bounouar, T. Höhne, S.-I. Park, G.-H. Ryu, T. Heindel, S. Burger, J.-D. Song, S. Rodt and S. Reitzenstein, *Deterministic Integration of Quantum Dots into on-Chip Multimode Interference Beamsplitters Using in Situ Electron Beam Lithography*, Nano Letters **18**(4), p. 2336 (2018).
- [Sch18c] P.-I. Schneider, N. Srocka, S. Rodt, L. Zschiedrich, S. Reitzenstein and S. Burger, *Numerical optimization of the extraction efficiency of a quantum-dot based single-photon emitter into a single-mode fiber*, Optics Express **26**(7), p. 8479 (2018).
- [Sch18d] L. Schweickert, K. D. Jöns, K. D. Zeuner, S. F. Covre da Silva, H. Huang, T. Lettner, M. Reindl, J. Zichi, R. Trotta, A. Rastelli and V. Zwiller, *On-demand generation of background-free single photons from a solid-state source*, Applied Physics Letters **112**(9), p. 093106 (2018).
- [Sei06] S. Seidl, M. Kroner, A. Högele, K. Karrai, R. J. Warburton, A. Badolato and P. M. Petroff, *Effect of uniaxial stress on excitons in a self-assembled quantum dot*, Applied Physics Letters **88**(20), p. 203113 (2006).
- [Shi86] M. Shimbo, K. Furukawa, K. Fukuda and K. Tanzawa, *Silicon-to-silicon direct bonding method*, Journal of Applied Physics **60**(8), p. 2987 (1986).
- [Shi88] Y. H. Shih and C. O. Alley, *New Type of Einstein-Podolsky-Rosen-Bohm Experiment Using Pairs of Light Quanta Produced by Optical Parametric Down Conversion*, Physical Review Letters **61**, p. 2921 (1988).

- [Sho97] P. W. Shor, *Polynomial-Time Algorithms for Prime Factorization and Discrete Logarithms on a Quantum Computer*, SIAM Journal on Computing **26**, p. 1484 (1997).
- [Sip14] A. Sipahigil, K. D. Jahnke, L. J. Rogers, T. Teraji, J. Isoya, A. S. Zibrov, F. Jelezko and M. D. Lukin, *Indistinguishable Photons from Separated Silicon-Vacancy Centers in Diamond*, Physical Review Letters **113**, p. 113602 (2014).
- [Sni18] H. Snijders, J. A. Frey, J. Norman, V. P. Post, A. C. Gossard, J. E. Bowers, M. P. van Exter, W. Löffler and D. Bouwmeester, *Fiber-Coupled Cavity-QED Source of Identical Single Photons*, Physical Reviews Applied **9**, p. 031002 (2018).
- [Som82] T. Soma, J. Satoh and H. Matsuo, *Thermal expansion coefficient of GaAs and InP*, Solid State Communications **42**(12), p. 889 (1982).
- [Som16] N. Somaschi, V. Giesz, L. De Santis, J. C. Loredó, M. P. Almeida, G. Hornecker, S. L. Portalupi, T. Grange, C. Antón, J. Demory, C. Gómez, I. Sagnes, N. D. Lanzillotti-Kimura, A. Lemaître, A. Auffeves, A. G. White, L. Lanco and P. Senellart, *Near-optimal single-photon sources in the solid state*, Nature Photonics (2016).
- [Spa16] C. M. Sparrow, *On Spectroscopic Resolving Power*, Astrophysical Journal **44**, p. 76 (1916).
- [Spe11] H. P. Specht, C. Nölleke, A. Reiserer, M. Uphoff, E. Figueroa, S. Ritter and G. Rempe, *A single-atom quantum memory*, Nature **473**, p. 190 (2011).
- [Spr13] J. B. Spring, B. J. Metcalf, P. C. Humphreys, W. S. Kolthammer, X.-M. Jin, M. Barbieri, A. Datta, N. Thomas-Peter, N. K. Langford, D. Kundys, J. C. Gates, B. J. Smith, P. G. R. Smith and I. A. Walmsley, *Boson Sampling on a Photonic Chip*, Science **339**(6121), p. 798 (2013).
- [Ste89] R. Stengl, T. Tan and U. Gösele, *A Model for the Silicon Wafer Bonding Process*, Japanese Journal of Applied Physics **28**(10R), p. 1735 (1989).
- [Sti95] O. Stier, M. Grundmann and D. Bimberg, *InAs/GaAs pyramidal quantum dots: Strain distribution, optical phonons, and electronic structure*, Physical Review B **52**(16), p. 11969 (1995).
- [Sti99] O. Stier, M. Grundmann and D. Bimberg, *Electronic and optical properties of strained quantum dots modeled by 8-band $k\cdot p$* , Physical Review B **59**(8), p. 5688 (1999).

- [Sto09] S. Stobbe, J. Johansen, P. T. Kristensen, J. M. Hvam and P. Lodahl, *Frequency dependence of the radiative decay rate of excitons in self-assembled quantum dots: Experiment and theory*, Physical Review B **80**, p. 155307 (2009).
- [Str12] A. Strittmatter, A. Schliwa, J.-H. Schulze, T. D. Germann, A. Dreismann, O. Hitzemann, E. Stock, I. A. Ostapenko, S. Rodt, W. Unrau, U. W. Pohl, A. Hoffmann, D. Bimberg and V. Haisler, *Lateral positioning of InGaAs quantum dots using a buried stressor*, Applied Physics Letters **100**(9), 093111 (2012).
- [Stu11] D. Stucki, M. Legré, F. Buntschu, B. Clausen, N. Felber, N. Gisin, L. Henzler, P. Junod, G. Litzistorf, P. Monbaron, L. Monat, J.-B. Page, D. Perroud, G. Ribordy, A. Rochas, S. Robyr, J. Tavares, R. Thew, P. Trinkler, S. Ventura, R. Voinol, N. Walenta and H. Zbinden, *Long-term performance of the SwissQuantum quantum key distribution network in a field environment*, New Journal of Physics **13**(12), p. 123001 (2011).
- [Sun99] H.-B. Sun, S. Matsuo and H. Misawa, *Three-dimensional photonic crystal structures achieved with two-photon-absorption photopolymerization of resin*, Applied Physics Letters **74**(6), p. 786 (1999).
- [Sun10] Y. Sun, S. E. Thompson and T. Nishida, *Strain Effect in Semiconductors: Theory and Device Applications*, Springer (2010).
- [Sun13] S. Sun, H. Kim, G. S. Solomon and E. Waks, *Strain tuning of a quantum dot strongly coupled to a photonic crystal cavity*, Applied Physics Letters **103**(15), p. 151102 (2013).
- [Sze06] S. Sze and K. Ng, *Physics of Semiconductor Devices*, Wiley (2006), URL <https://books.google.de/books?id=o4unkmHBhb8C>.
- [Tak05] H. Takesue, E. Diamanti, T. Honjo, C. Langrock, M. M. Fejer, K. Inoue and Y. Yamamoto, *Differential phase shift quantum key distribution experiment over 105 km fibre*, New Journal of Physics **7**(1), p. 232 (2005).
- [Tan02] S. Tanzilli, W. Tittel, H. De Riedmatten, H. Zbinden, P. Baldi, M. DeMicheli, D. Ostrowsky and N. Gisin, *PPLN waveguide for quantum communication*, The European Physical Journal D - Atomic, Molecular, Optical and Plasma Physics **18**(2), p. 155 (2002).

- [Thi17] S. Thiele, K. Arzenbacher, T. Gissibl, H. Giessen and A. M. Herkommer, *3D-printed eagle eye: Compound microlens system for foveated imaging*, Science Advances **3**(2) (2017).
- [Tho16] A. Thoma, P. Schnauber, M. Gschrey, M. Seifried, J. Wolters, J.-H. Schulze, A. Strittmatter, S. Rodt, A. Carmele, A. Knorr, T. Heindel and S. Reitzenstein, *Exploring Dephasing of a Solid-State Quantum Emitter via Time- and Temperature-Dependent Hong-Ou-Mandel Experiments*, Physical Review Letters **116**, p. 033601 (2016).
- [Tho17] A. Thoma, *Deterministische Quantenpunktmikrolinsen als effiziente Quantenlichtquellen*, phdthesis, Technische Universität Berlin (2017).
- [Tir15] A. Tiranov, J. Lavoie, A. Ferrier, P. Goldner, V. B. Verma, S. W. Nam, R. P. Mirin, A. E. Lita, F. Marsili, H. Herrmann, C. Silberhorn, N. Gisin, M. Afzelius and F. Bussi eres, *Storage of hyperentanglement in a solid-state quantum memory*, Optica **2**(4), p. 279 (2015).
- [Ton94] Q.-Y. Tong, E. Schmidt, U. G esele and M. Reiche, *Hydrophobic silicon wafer bonding*, Applied Physics Letters **64**(5), p. 625 (1994).
- [Top14] V. Y. Topolov, P. Bisegna and C. R. Bowen, *The piezoelectric medium and its electromechanical properties*, in *Piezo-Active Composites: Orientation Effects and Anisotropy Factors*, p. 1–23, Springer Berlin Heidelberg (2014), URL https://doi.org/10.1007/978-3-642-38354-0_1.
- [T ur00] V. T urck, S. Rodt, O. Stier, R. Heitz, R. Engelhardt, U. W. Pohl, D. Bimberg and R. Steingr uber, *Effect of random field fluctuations on excitonic transitions of individual CdSe quantum dots*, Physical Review B **61**, p. 9944 (2000).
- [Tro12a] R. Trotta, P. Atkinson, J. D. Plumhof, E. Zallo, R. O. Rezaev, S. Kumar, S. Baunack, J. R. Schr oter, A. Rastelli and O. G. Schmidt, *Nanomembrane Quantum-Light-Emitting Diodes Integrated onto Piezoelectric Actuators*, Advanced Materials **24**(20), p. 2668 (2012).
- [Tro12b] R. Trotta, E. Zallo, C. Ortix, P. Atkinson, J. D. Plumhof, J. van den Brink, A. Rastelli and O. G. Schmidt, *Universal Recovery of the Energy-Level Degeneracy of Bright Excitons in InGaAs Quantum Dots without a Structure Symmetry*, Physical Review Letters **109**, p. 147401 (2012).

- [Tro14] R. Trotta, J. S. Wildmann, E. Zallo, O. G. Schmidt and A. Rastelli, *Highly Entangled Photons from Hybrid Piezoelectric-Semiconductor Quantum Dot Devices*, Nano Letters **14**(6), p. 3439 (2014).
- [Tro15a] R. Trotta, J. Martín-Sánchez, I. Daruka, C. Ortix and A. Rastelli, *Energy-Tunable Sources of Entangled Photons: A Viable Concept for Solid-State-Based Quantum Relays*, Physical Review Letters **114**, p. 150502 (2015).
- [Tro15b] R. Trotta, J. Martín-Sánchez, J. S. Wildmann, G. Piredda, M. Reindl, C. Schimpf, S. Zallo, E. and Stroj, J. Edlinger and A. Rastelli, *Wavelength-tunable source of entangled photons interfaced with atomic vapours*, Nature Communications **7**, p. 10375 (2015).
- [Tsa02] C. H. Tsau, S. M. Spearing and M. A. Schmidt, *Fabrication of wafer-level thermocompression bonds*, Journal of Microelectromechanical Systems **11**(6), p. 641 (2002).
- [Two98] W. W. Tworzydło, W. Cecot, J. T. Oden and C. H. Yew, *Computational micro- and macroscopic models of contact and friction: formulation, approach and applications*, Wear **220**(2), p. 113 (1998).
- [Unr12] W. Unrau, D. Quandt, J.-H. Schulze, T. Heindel, T. D. Germann, O. Hitzemann, A. Strittmatter, S. Reitzenstein, U. W. Pohl and D. Bimberg, *Electrically driven single photon source based on a site-controlled quantum dot with self-aligned current injection*, Applied Physics Letters **101**(21), 211119 (2012).
- [Uns16] S. Unsleber, Y.-M. He, S. Gerhardt, S. Maier, C.-Y. Lu, J.-W. Pan, N. Gregersen, M. Kamp, C. Schneider and S. Höfling, *Highly indistinguishable on-demand resonance fluorescence photons from a deterministic quantum dot micropillar device with 74 % extraction efficiency*, Optics Express **24**(8), p. 8539 (2016).
- [Usk98] A. V. Uskov, J. McInerney, F. Adler, H. Schweizer and M. H. Pilkuhn, *Auger carrier capture kinetics in self-assembled quantum dot structures*, Applied Physics Letters **72**(1), p. 58 (1998).
- [Var67] Y. P. Varshni, *Temperature dependence of the energy gap in semiconductors*, Physica **34**(1), p. 149 (1967).
- [Ved06] V. Vedral, *Introduction to Quantum Information Science*, Oxford University Press (2006).

- [Ver14] M. A. M. Versteegh, M. E. Reimer, K. D. Jöns, D. Dalacu, P. J. Poole, A. Gulnatti, A. Giudice and V. Zwiller, *Observation of strongly entangled photon pairs from a nanowire quantum dot*, Nature Communications **5**, p. 5298 (2014).
- [Vie86] S. Vieira, *The behavior and calibration of some piezoelectric ceramics used in the STM*, IBM Journal of Research and Development **30**(5), p. 553 (1986).
- [Voi10] W. Voigt, *Lehrbuch der Kristallphysik: mit Ausschluss der Kristalloptik*, Teubner (1910).
- [Vol26] M. Volmer and A. Weber, *Keimbildung in übersättigten Gebilden*, Zeitschrift für physikalische Chemie **119**, p. 277 (1926).
- [Wan04] C. F. Wang, A. Badolato, I. Wilson-Rae, P. M. Petroff, E. Hu, J. Urayama and A. Imamoglu, *Optical properties of single InAs quantum dots in close proximity to surfaces*, Applied Physics Letters **85**(16), p. 3423 (2004).
- [Wan15] J. Wang, G.-C. Gong, M. and Guo and L. He, *Towards Scalable Entangled Photon Sources with Self-Assembled InAs/GaAs Quantum Dots*, Physical Review Letters. **115**, p. 067401 (2015).
- [Wei14] Y.-J. Wei, Y.-M. He, M.-C. Chen, Y.-N. Hu, Y. He, D. Wu, C. Schneider, M. Kamp, S. Höfling, C.-Y. Lu and J.-W. Pan, *Deterministic and Robust Generation of Single Photons from a Single Quantum Dot with 99.5 % Indistinguishability Using Adiabatic Rapid Passage*, Nano Letters **14**(11), p. 6515 (2014).
- [Wie06] M. Wiemer, C. Jia, M. Toepfer and K. Hauck, *Wafer bonding with bcb and su-8 for mems packaging*, in *2006 1st Electronic Systemintegration Technology Conference*, volume 2, p. 1401–1405 (2006).
- [Woo82] W. K. Wootters and W. H. Zurek, *A single quantum cannot be cloned*, Nature **299**, p. 802 (1982).
- [Wu92] E.-S. Wu, J. H. Strickler, W. R. Harrell and W. W. Webb, *Two-photon lithography for microelectronic application*, Proc. SPIE: Optical/Laser Microlithography V **1674**, p. 7 (1992).
- [Yac86] B. G. Yacobi and D. B. Holt, *Cathodoluminescence scanning electron microscopy of semiconductors*, Journal of Applied Physics **59**(4), p. R1 (1986).
- [Yin16] H.-L. Yin, T.-Y. Chen, Z.-W. Yu, H. Liu, L.-X. You, Y.-H. Zhou, S.-J. Chen, Y. Mao, M.-Q. Huang, W.-J. Zhang, H. Chen, M. J. Li, D. Nolan, F. Zhou,

- X. Jiang, Z. Wang, Q. Zhang, X.-B. Wang and J.-W. Pan, *Measurement-Device-Independent Quantum Key Distribution Over a 404 km Optical Fiber*, Physical Review Letters **117**, p. 190501 (2016).
- [Yu06] L. Yu, F. E. H. Tay, G. Xu, B. Chen, M. Avram and C. Iliescu, *Adhesive bonding with SU-8 at wafer level for microfluidic devices*, Journal of Physics: Conference Series **34**(1), p. 776 (2006).
- [Zha11] S. Zhang, F. Li, N. P. Sherlock, J. Luo, H. J. Lee, R. Xia, R. J. J. Meyer, W. Hackenberger and T. R. Shrout, *Recent Developments on High Curie Temperature PIN-PMN-PT Ferroelectric Crystals*, Journal of Crystal Growth **318**(1), p. 846 (2011).
- [Zha15] J. Zhang, J. S. Wildmann, F. Ding, R. Trotta, Y. Huo, E. Zallo, D. Huber, A. Rastelli and O. G. Schmidt, *High yield and ultrafast sources of electrically triggered entangled-photon pairs based on strain-tunable quantum dots*, Nature communications **6**, p. 10067 (2015).
- [Zis17] D. Ziss, J. Martín-Sánchez, T. Lettner, A. Halilovic, G. Trevisi, R. Trotta, A. Rastelli and J. Stangl, *Comparison of different bonding techniques for efficient strain transfer using piezoelectric actuators*, Journal of Applied Physics **121**(13), p. 135303 (2017).
- [Zop18] M. Zopf, T. Macha, R. Keil, E. Uruñuela, Y. Chen, W. Alt, L. Ratschbacher, F. Ding, D. Meschede and O. G. Schmidt, *Frequency feedback for two-photon interference from separate quantum dots*, Physical Review B **98**, p. 161302 (2018).

A Comparison of different design approaches for single-photon sources based on quantum dots

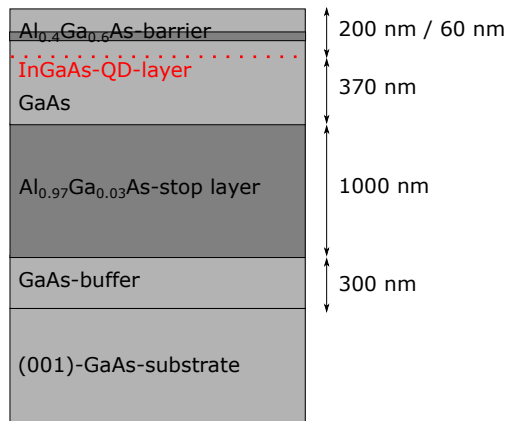
Table A.1: Characteristics of high-performance design approaches for the creation of optically triggered QD-based single-photon sources. Compared are the photon-extraction efficiency η_{Exp} , the second-order autocorrelation $g^{(2)}(\tau = 0)$, the indistinguishability of consecutively emitted photons measured by the visibility, a wavelength tuning achieved by strain transfer, implementations of a direct fiber-coupling and the implementation of a deterministic device processing. The latter refers to a fabrication method that allows one to choose a QD by its emission characteristics before integrating it in-situ into a microstructure.

Type	η_{Exp} [%]	$g^{(2)}(0)^1$	Visibility [%] ¹	Strain-tuning	Direct fiber-coupl.	Determin. fabr.
Planar cavity	$65 \pm 4^{2,3}$ [Che18]	$< 10^{-4}$ [Han18, Sch18d]	99.5 [Wei14]	20 meV [Tro12a]	y [Kum16]	n
Microlenses	$40 \pm 4^{2,3}$ [Fis17]	< 0.01 [Gsc15b]	94 ± 6 [Tho16]	1.7 nm [Fis18]	y [Sch18a]	y [Gsc15b]
Micropillar	79 ± 8^4 [Gaz13]	$< 0.0028 \pm 0.0012$ [Som16]	99.56 ± 0.45 [Som16]	n	y [Sni18]	y [Dou08]
Photonic crystal	44.3 ± 2.1^5 [Mad14]	0.04 ± 0.05 [Mad14]	93.9 [Liu18]	0.45 nm [Sun13]	y [Lee15]	n
Nanowire	72 ± 9^6 [Cla10]	< 0.008 [Cla10]	n	3 meV [Che16]	y [Cad16]	n

¹ Under pulsed excitation ² Using additional on-chip optics ³ NA=0.42 ⁴ NA=0.4 ⁵ NA=0.6 ⁶ NA=0.75

B Layer designs for sample growth by MOCVD

(a) QD sample for flip-chip process



(b) QD sample with DBR mirror

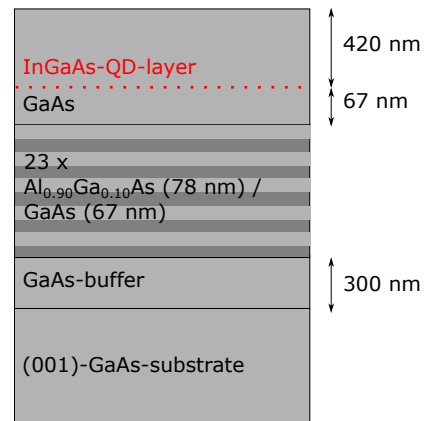


Figure B.1: Layouts for the MOCVD growth of the samples used in this work. (a) Layer structure for flip-chip thermocompression gold bonding with a top layer of either 60 or 200 nm of GaAs, including an AlGaAs diffusion barrier layer. 370 nm of GaAs are grown for the processing of microstructures after a flip-chip bonding process. (b) Layer structure with QDs on top of a DBR mirror with a stopband centered around 920 nm. A GaAs capping layer of 420 nm is applied for the fabrication of microlenses.

Danksagung

Ich möchte mich herzlich bedanken bei allen, die zum Gelingen dieser Arbeit beigetragen haben:

- An erster Stelle möchte ich mich bei Prof. Dr. Stephan Reitzenstein bedanken für die Möglichkeit in seiner Gruppe an der TU Berlin zu forschen und dort meine Promotion anzufertigen. Er nahm sich stets Zeit für meine Fragen und Anliegen und sorgte für eine positive und offene Arbeitsatmosphäre, welche die Arbeit in der Gruppe sehr angenehm gemacht hat.
- Prof. Dr. Armando Rastelli danke ich für die Übernahme des Zweitgutachtens dieser Arbeit.
- Besonderer Dank gilt Dr. Sven Rodt für die Einarbeitung in der Arbeitsgruppe, zahlreiche inhaltliche Diskussionen und Ratschläge, sowie für die angenehme Bürogesellschaft.
- Dr. Tobias Heindel möchte ich für häufige Unterstützung bei der Durchführung von Messungen sowie hilfreiche Diskussionen danken.
- Meinem Reinraum-"Buddy" Ronny Schmidt danke ich für die hervorragende Einarbeitung sowie zahlreiche Hinweise und Diskussionen zu Themen rund um die Halbleiterprozessierung. Desweiteren möchte ich mich bei ihm, Stefan Bock, René Linke und Kathrin Schatke für die zuverlässige Betreuung der Labore und technische Hilfestellungen bedanken.
- Arsenty Kaganskiy danke ich für das exzellente Wachstum der in dieser Arbeit verwendeten Proben.
- Ich danke Peter Schnauber für die gute Einarbeitung im KL-Labor und die angenehme Bürogesellschaft. Zudem danke ich dem gesamten "KL-Team", Dr. Sven Rodt, Peter Schnauber, Nicole Srocka, Tobias Heuser, Arsenty Kaganskiy und den dazugehörigen Studenten für die gute Zusammenarbeit und gegenseitige Unterstützung im Labor.

- Zahlreichen Experten zum Thema μ -PL danke ich für Tipps und Unterstützung im Labor, insbesondere Alexander Schlehahn, Alexander Thoma, Fabian Gericke, Marco Schmidt und Martin von Helversen.
- Allen anderen Mitgliedern der AG Reitzenstein möchte ich für fachliche Diskussionen, gesellige Mittagessen und Kaffeepausen und weitere schöne Erlebnisse und Erinnerungen danken!
- Dr. Andrei Schliwa und Ludwig Greif danke ich für Simulationsergebnisse und Diskussionen zu Verspannungseffekten an Quantenpunkt-Mikrolinsen.
- Ich danke Prof. Dr. Harald Giessen, Simon Ristok, Ksenia Weber und Timo Gisibl von der Universität Stuttgart für die erfolgreiche Zusammenarbeit zum Thema Mikroobjektive, sowie Simon Thiele von der Universität Stuttgart für Simulationsergebnisse und Diskussionen hierzu.
- Bei Dr. Sven Burger und seinem Team am Zuse-Institut Berlin bedanke ich mich für die Einarbeitung und Beratung bei der Simulation mit JCMSuite.
- Meinen Studenten Max Flach (Bachelor) und Jan Hausen (Master) danke ich für die gute Zusammenarbeit im Rahmen ihrer Abschlussarbeiten.
- Zu guter Letzt danke ich meinem Partner und meinen Eltern für vielseitigste Unterstützung während des Studiums und der Promotionszeit.

Erklärung zu Vorveröffentlichungen

Gemäß §2 Abs. 4 sowie §5 Abs. 1 Ziff. 5 der Promotionsordnung der Technischen Universität Berlin:

Es liegen bereits folgende Veröffentlichungen mit Inhalten aus meiner Dissertation vor:

- S. Fischbach, A. Schlehahn, A. Thoma, N. Srocka, T. Gissibl, S. Ristok, S. Thiele, A. Kaganskiy, A. Strittmatter, T. Heindel, S. Rodt, A. Herkommer, H. Giessen und S. Reitzenstein, *Single Quantum Dot with Microlens and 3D-Printed Micro-objective as Integrated Bright Single-Photon Source*, ACS Photonics **4**, 1327-1332 (2017).
Eigenanteil: Designoptimierung mittels Finite-Elemente Methode, Herstellung der Quantenpunkt-Mikrolinsen, Spektroskopie und quantenoptische Analyse mit Datenauswertung
- S. Fischbach, A. Kaganskiy, E. B. Y. Tauscher, F. Gericke, A. Thoma, R. Schmidt, A. Strittmatter, T. Heindel, S. Rodt, und S. Reitzenstein, *Efficient single-photon source based on a deterministically fabricated single quantum dot - microstructure with backside gold mirror*, Applied Physics Letters **111**, 011106 (2017)
Eigenanteil: Designoptimierung mittels Finite-Elemente Methode, Entwicklung eines Verfahrens zum Thermokompressionsbonden, Herstellung der Quantenpunkt-Mikrostrukturen, Spektroskopie und quantenoptische Analyse mit Datenauswertung

Zur Veröffentlichung eingereicht ist der folgende Beitrag:

- S. Fischbach, M. von Helversen, M. Schmidt, A. Kaganskiy, R. Schmidt, A. Schliwa, T. Heindel, S. Rodt, und S. Reitzenstein, *A deterministically fabricated spectrally-tunable quantum dot based single-photon source*, ArXiv e-prints 1805.10623 (2018) [cond-mat.mes-hall]
Eigenanteil: Designoptimierung mittels Finite-Elemente Methode, Entwicklung eines Verfahrens zum Thermokompressionsbonden, Herstellung der Quantenpunkt-Mikrostrukturen, Spektroskopie und quantenoptische Analyse mit Datenauswertung

Nicht Inhalt der vorliegenden Arbeit sind die folgenden Veröffentlichungen:

- T. Jakubczyk, V. Delmonte, S. Fischbach, D. Wigger, D. E. Reiter, Q. Mermillod, P. Schnauber, A. Kaganskiy, J.-H. Schulze, A. Strittmatter, S. Rodt, W. Langbein, T. Kuhn, S. Reitzenstein, und J. Kasprzak, *Impact of Phonons on Dephasing of Individual Excitons in Deterministic Quantum Dot Microlenses*, ACS Photonics **3**, 2461–2466 (2016)
Eigenanteil: Herstellung und Vorcharakterisierung von Quantenpunkt-Mikrolinsen
- I. A. Derebezov, V. A. Gaisler, A. V. Gaisler, D. V. Dmitriev, A. I. Toropov, S. Fischbach, A. Schlehahn, A. Kaganskiy, T. Heindel, S. Bounouar, S. Rodt, und S. Reitzenstein, *Subminiature emitters based on a single (111) In(Ga)As quantum dot and hybrid microcavity*, Semiconductors **51**(11), 1399–1402 (2017)
Eigenanteil: Herstellung und Vorcharakterisierung von Quantenpunkt-Mikrolinsen
- V. A. Gaisler, I. A. Derebezov, A. V. Gaisler, D. V. Dmitriev, A. I. Toropov, S. Fischbach, A. Schlehahn, A. Kaganskiy, T. Heindel, S. Bounouar, S. Rodt, und S. Reitzenstein, *Hybrid microcavity for superminiature single quantum dot based emitters*, Optoelectronics, Instrumentation and Data Processing **53**(2), 178–183 (2017)
Eigenanteil: Herstellung und Vorcharakterisierung von Quantenpunkt-Mikrolinsen
- A. Schlehahn, S. Fischbach, R. Schmidt, A. Kaganskiy, A. Strittmatter, S. Rodt, T. Heindel, and S. Reitzenstein, *A stand-alone fiber-coupled single-photon source*, Scientific Reports **8**, 1340 (2018)
Eigenanteil: Herstellung von Quantenpunkt-Mikrolinsen, Beteiligung an Verklebungen von optischen Fasern, Beteiligung an quantenoptischen Messungen an fasergekoppelten Proben
- A. Kaganskiy, S. Fischbach, A. Strittmatter, S. Rodt, T. Heindel, and S. Reitzenstein *Enhancing the photon-extraction efficiency of site-controlled quantum dots by deterministically fabricated microlenses*, Optics Communications **413**, 162-166 (2018)
Eigenanteil: Simulationen von Mikrostrukturen mittels Finite-Elemente-Methode

Berlin, den

Sarah Fischbach

Versicherung an Eides statt

Hiermit erkläre ich, dass mir die geltende Promotionsordnung der TU Berlin in der Fassung vom 05.02.2014 bekannt ist.

Gemäß §5 Abs. 1 Ziff. 6 und 7 der Promotionsordnung der Technischen Universität Berlin: Hiermit erkläre ich an Eides statt, dass ich die Dissertation selbstständig und ohne Hilfe eines Promotionsberaters angefertigt und keine anderen als die angegebenen Quellen und Hilfsmittel benutzt habe.

Die gemachten Angaben zum Eigenanteil an bestehenden Vorveröffentlichungen in Ko-Autorenschaft sind zutreffend.

Ich habe bei keiner anderen Hochschule oder Fakultät eine Promotionsabsicht eingereicht oder ein Promotionsverfahren beantragt.

Berlin, den

Sarah Fischbach